

3 LATTICE AND ACCELERATOR PHYSICS

3.1 Lattice and Beam Dynamics

The storage ring lattice is designed to provide a stable, closed orbit on which the electron beam can circulate with long lifetime and efficient injection of beam from the booster. This injection will be capable of filling the ring from zero beam current to the operating values (≤ 500 mA) in a short time, as well as to provide top-off injection to maintain a constant level of beam current ($< \pm 0.5\%$ variations) and thus provide a constant radiated beam power on the users' beamline components, with low thermal distortions.

The electron beam will be damped by the synchrotron radiation to a small beam emittance lower than that of any storage ring light source currently operating or under construction. The photon beams radiated from undulators will, therefore, have lower emittance and higher brilliance, surpassing any existing light sources in the 2 to 10 keV range in focused beam flux on small specimens.

3.1.1 Physics and Design Goals for the Storage Ring Lattice

The design of the NSLS-II storage ring is driven by goals required to achieve the baseline performance as well as challenge goals that will provide the potential for future upgrades of beam performance. The challenge goals will keep NSLS-II at the frontier of the field for an extended time. Table 3.1.1 lists the required and challenge goals.

Table 3.1.1 Goals for the NSLS-II Design.

Beam Property	Required Goal	Challenge Goal
Ultra low horizontal emittance [nm-rad]	≤ 1.5 (achromatic)	≤ 0.5
Vertical emittance [nm-rad]	0.010	0.008
Stored currents [mA]	500	750
Straights for insertion devices	≥ 21	27
Low dispersion space for Three Pole Wigglers	≥ 15	≥ 15
Electron beam stability [% of beam size]	10	< 5
Top-off injection current stability ($\Delta t \geq 2$ min) [%]	< 1	< 1

Several lattices have been studied over the past few years. As work progressed, it became clear that the Double Bend Achromatic lattice could meet the emittance goals while providing an increased number of insertion device straight sections. To achieve our low emittance goals, we maintain achromatic arcs and install damping wigglers in the extra ID straight sections to enhance the SR power without significantly increasing the quantum excitation of the electron beam [3.1.1]. This process yields a net reduction of the beam emittance proportionally related to the ratio of dipole-radiated power to the DW-radiated power, reducing the beam emittance up to five-fold without significantly impacting the dynamic aperture performance of the ring.

The minimum emittance for a DBA lattice with 2M dipole magnets and electron energy $E_0 = \gamma mc^2$ is given by

$$\varepsilon_0^{\min} = (7.7 \times 10^{-4} \text{ nm-rad}) \gamma^2 / M^3. \quad (3.1-1)$$

The achievable emittance for a realistic lattice design is about twice this minimum value. The momentum compaction is

$$\alpha = \frac{\pi^2}{6M^2} \frac{2\pi \rho_0}{C}, \quad (3.1-2)$$

where ρ_0 is the dipole magnet bending radius and C is the ring circumference. Note that the momentum compaction increases linearly with bend radius.

The emittance ε_w with damping wigglers is related to that without damping wigglers, ε_0 , by $\varepsilon_w \approx \varepsilon_0 / (1 + U_w / U_0)$, where U_w / U_0 is the ratio of the energy lost per turn in the wigglers to that lost in the dipoles. For NSLS-II, we chose to have a large dipole bending radius. This reduces the energy radiated in the dipoles, which means we need to radiate less energy in the wigglers to reduce the emittance by a given factor.

To be more precise, consider a wiggler of length L_w having bending radius ρ_w and period λ_w centered in the insertion section. The ratio of the fractional energy spread with the wiggler to that without is

$$\frac{\delta_w}{\delta_0} = \sqrt{\left[1 + \frac{L_w}{2\pi \rho_0} \frac{4}{3\pi} \left(\frac{\rho_0}{\rho_w} \right)^3 \right] \left[1 + \frac{L_w}{4\pi \rho_0} \left(\frac{\rho_0}{\rho_w} \right)^2 \right]^{-1}}, \quad (3.1-3)$$

and the ratio of the emittance with the wiggler to that without is

$$\frac{\varepsilon_w}{\varepsilon_0} = \frac{1 + f}{1 + \frac{L_w}{4\pi \rho_0} \left(\frac{\rho_0}{\rho_w} \right)^2}. \quad (3.1-4)$$

The fluctuation factor, f , is given by

$$f = \frac{2C_q \gamma^2}{3\pi^2 \varepsilon_0} \frac{L_w \rho_0}{\rho_w^3} \left[\frac{K_w^2}{5\gamma^2} \langle \beta_x \rangle + \frac{\eta_0^2}{\beta_{x0}} + \beta_{x0} \eta_1^2 \right], \quad (3.1-5)$$

where $C_q = 3.84 \times 10^{-13} \text{ m}$, and strength parameter $K_w = \lambda_w \gamma / 2\pi \rho_w$. The horizontal beta function is given by $\beta_x(s) = \beta_{x0} + s^2 / \beta_{x0}$, where $s = 0$ is the center of the wiggler and insertion, and $\langle \beta_x \rangle$ denotes the average value of β_x in the wiggler. We express the dispersion function in the wiggler in the form $\eta(s) = \eta_w(s) + \eta_0 + \eta_1 s$, where $\eta_w(s)$ is the sinusoidal dispersion generated by the wiggler itself, and $\eta_0 + \eta_1 s$ is the dispersion generated by errors elsewhere in the ring. Eq. (3.1-5) can be used to determine a tolerance on the dispersion in the insertions arising from errors.

As at ESRF, the NSLS-II lattice has alternating high and low horizontal beta function straight sections for insertion devices. A large value of β_x is desired at the injection septum. Small β_x is desired in undulators for beamlines designed to focus the radiation down to a small spot. The vertical beta function should be small in undulators to optimize brightness. In fact, it is essential that β_y not be large in any of the insertion devices. The linear tune shift produced by an undulator or wiggler is

$$\Delta \nu_y = \frac{\langle \beta_y \rangle L_w}{8\pi\rho_w^2}. \quad (3.1-6)$$

Small β_y keeps the tune shift within acceptable limits. We have bounded the straight sections with quadrupole triplets in order to provide a local correction for the modification of the betatron functions and phases due to undulator or wiggler focusing.

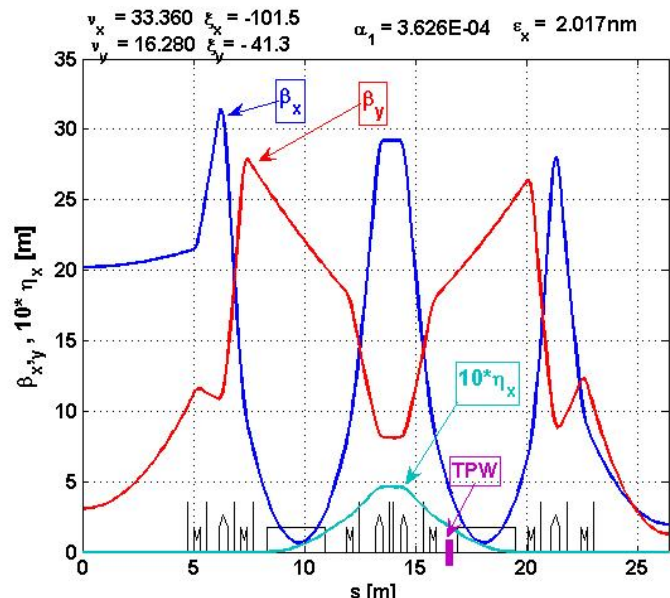
The tune shift with amplitude due to nonlinear undulator or wiggler focusing is

$$\frac{d\nu_y}{dJ} = \frac{\pi \langle \beta_y^2 \rangle L_w}{4\lambda_w^2 \rho_w^2}. \quad (3.1-7)$$

To minimize the effect of the nonlinear focusing on dynamic aperture, it is essential to have small β_y in the insertion devices.

This is the approach taken for NSLS-II [3.1.2]. A DBA with 30 cells was chosen as the lattice structure, with a natural emittance of 2.0 nm. One cell of the lattice, shown in Figure 3.1.1, comprises half a super-period with reflection symmetry about the right or left hand end of the cell. The lattice functions have been optimized to achieve achromatic arcs, low emittance and modest chromatic sextupole strengths, small Closed Orbit Amplification Factors, and desired betatron functions in the long and short straight sections, which are required for small impact on the DA of the IDs, as given by Eq. (3.1-6 and 3.1-7). The working point tune was selected for optimization of the sextupole correction of the nonlinear driving terms that limit the DA, as well as reduced COAF and instability sensitivity. The dipole magnets have been optimized (bend radius $\rho_0 = 25$ m, $B_0 = 0.399$ T at 3 GeV) to enhance the reduction of the beam emittance with the DWs. Although the bare lattice doesn't quite meet the required emittance goal (2.0 nm instead of 1.5 nm), this goal is exceeded with only one 7 m DW installed and operated at a peak field of 1.8 T.

Figure 3.1.1 The lattice functions for one-half of a DBA period. A super-period consists of this cell reflected about either ID center: 9.3 m on the left-hand side or 6.6 m on the right.



The impact of DWs on the emittance and the energy spread, given by Eq. (3.1-3 and 3.1-4), is shown in Figure 3.1.2 for the designed $\rho_0 = 25$ m and a stronger dipole with 1.5 times the field ($2/3$ the bend radius). This calculation also assumes no significant spurious dispersion in the straight section, since the individual quadrupole powering in this lattice should allow the dispersion to be corrected cell-by-cell for any dipole variations. The gain in undulator brightness resulting from the smaller emittance provided by more damping

wigglers is somewhat reduced by the increased energy spread of the beam, especially at x-ray energies corresponding to higher harmonics of the undulator. Increasing the bend radius from 16.68 m to 25 m reduces both the emittance as well as the energy spread. Continuing to increase the bend radius to larger values is increasingly less effective at reducing the emittance as it approaches the IBS limit, and at the same time increasingly expensive, as it increases the circumference of the ring. As discussed in Chapter 5, a bend radius of 25 m is about optimal for NSLS-II. The installed RF power also provides a practical limit to the gain from more damping wigglers, since the beam lifetime will be reduced if the radiated power exceeds the installed power necessary for sufficient RF bucket height.

Figure 3.1.2 The fractional reduction of the ring emittance and the increase in energy spread for dipole magnets of bend radii: $\rho_0 = 25$ m (proposed for NSLS-II) and $\rho_0 = 13.7$ m dipole that could yield a shorter circumference lattice.

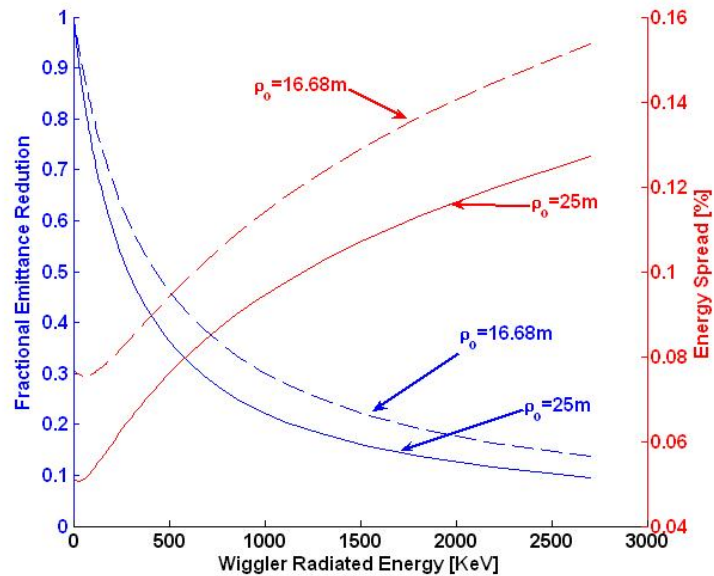


Table 3.1.2 lists the design parameters for this 15 super-period DBA (15×2) lattice. The choice of low dipole field restricts the photon beam energies radiated by the dipoles to 2.4 keV critical energy at 3 GeV. The dipole radiation will provide very bright VUV and soft-x-ray beams. Hard x-rays will be available from the installed DWs (10.8 keV critical energy) with high brilliance and flux.

Table 3.1.2 Storage Ring Parameters.

Energy [GeV]	3
Circumference [m]	791.96
DBA cells	30 (15 x 2)
Bending radius [m]	25.019
RF frequency [MHz]	499.68
Harmonic Number	1320
Momentum compaction	0.000368
Ring Tune: ν_x, ν_y	32.35, 16.28
Natural chromaticity: ζ_x, ζ_y	-103, -44.8
Maximum dispersion [m]	0.46
High-beta 9.3-m straights: β_x, β_y [m]	20.85, 2.94
Low-beta 6.6-m straights: β_x, β_y [m]	2.02, 1.06
Dipole radiated energy loss [keV]	286.5
Dipole critical energy [keV]	2.394

Figure 3.1.3 shows the expected reduction of the emittance as one to eight 7 m DWs are added to the ring.

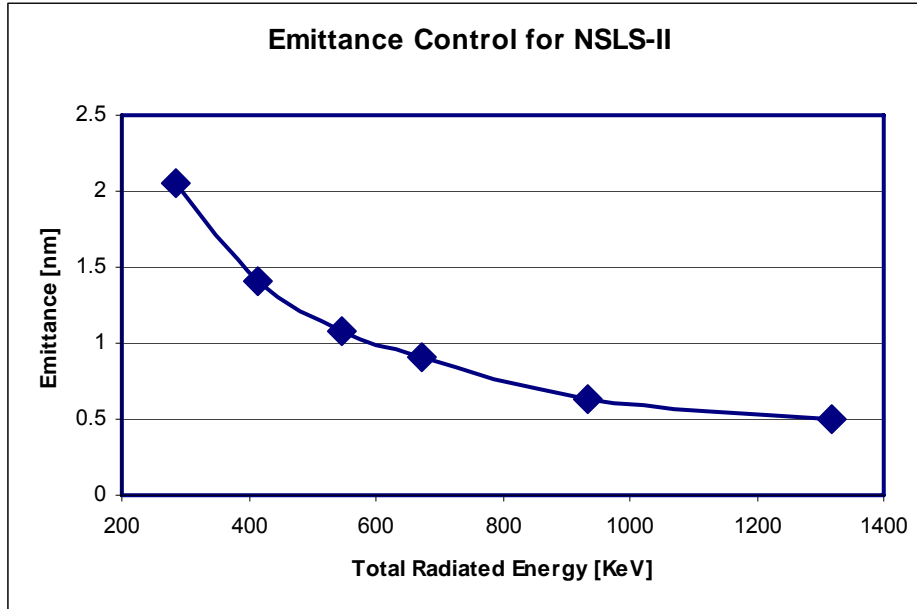


Figure 3.1.3
Emittance reduction for NSLS-II as 0, 1, 2, 3, 5, and 8 DW (7 m each) are installed and operated at 1.8 T peak field.

Table 3.1.3 compares the basic lattice properties with those obtained with 21 or 56 m of DWs installed in the ring. All of these DWs will have a fixed gap and will be available to drive user beamlines.

Table 3.1.3 Effect of Three and Eight 7 m Damping Wigglers on Beam Properties at 3 GeV.

	Zero DWs	Three 7 m DWs (21 m)	Eight 7 m DWs (56 m)
Energy loss [keV]	287	674	1320
RF voltage (3% bucket) [MV]	2.5	3.1	3.9
Synchrotron tune	0.0079	0.00876	0.0096
Natural emittance: ϵ_x, ϵ_y [nm-rad]	2.0, 0.01	0.9, 0.008	0.50, 0.008
Damping time: τ_x, τ_s [ms]	54, 27	23, 11.5	12, 6
Energy spread [%]	0.05	0.089	0.099
Bunch duration [ps]	10	15.4	15.5

The lattice shown in Figure 3.1.1, like that at ESRF, has low and high beta function straight sections. However, we have increased the length of the high- β_x straight section to provide for injection, space for RF cavities, and space for longer DWs and user IDs. The drift space between quadrupole magnets is 9.3 m. The space available for insertion devices is 7 m. The magnet layout for the Long ID straight section, with field free drift space of 9.3 m between sextupoles, is shown in Figure 3.1.4. Half the long ID is shown with reflective symmetry about the centerline (left-hand side). There are a total of six quadrupoles [(QH1, QH2, QH3) \times 2] and eight sextupoles [(SH1,... SH4) \times 2] in this ID straight section. Although they are considered as families of focusing strengths, each will be independently powered to account for magnet-to-magnet differences and for the possibility of shifting the symmetry condition for improved photon beam focusing. The three quadrupole families provide sufficient variables for correcting the local distortions of the linear lattice when IDs are installed or when the gaps are changed by the users [3.1.4, 3.1.5]. The center quadrupole (QH2) is 40cm long, while the other two are 25 cm long, in order to satisfy the maximum gradient of <22 T/m design criteria. The four families of sextupoles in this ID are required in order to correct the nonlinearity of

the lattice arising from the strong chromatic sextupoles located in the dispersive regions. For certain tunes, some sextupoles have small strengths. These might be dropped from a future optimized design.

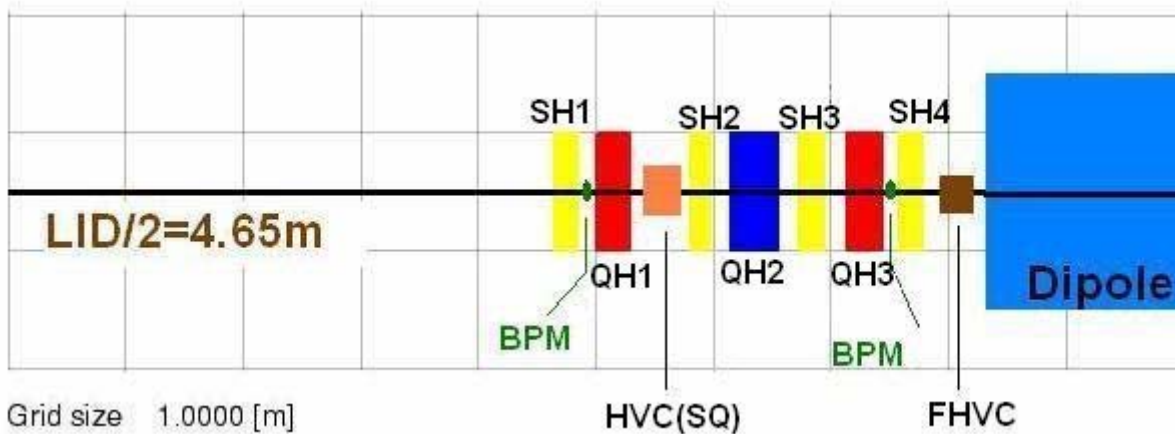


Figure 3.1.4 Layout for half of a long (high beta function-H) ID straight section, with reflection symmetry on left side.

The short ID straight section layout is shown in Figure 3.1.5. The short ID has a 6.6 m drift between the inner sextupoles and is similar to the long ID in layout of the quadrupoles and sextupole families. Differences include additional drift between quadrupoles to reduce the chromaticity, while providing the increased focusing needed for the lower beta functions. The quadrupoles are 25 cm long except for the center quadrupole (QL2) is 40 cm as in the long ID straight section. The QL2 quadrupole has the maximum gradient of the lattice quadrupoles, this magnet has a 10% safety margin of its maximum gradient to allow for tuning range for reducing the horizontal beta function in the short ID, for increase brightness of the ID source.

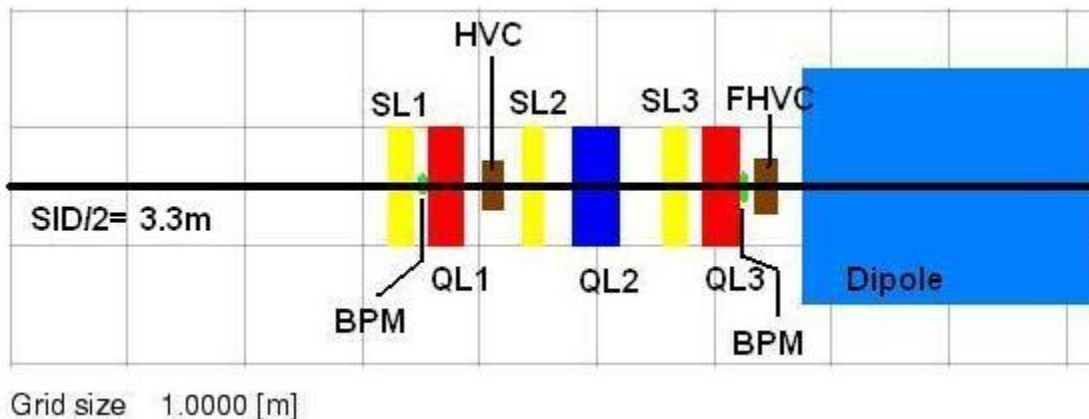


Figure 3.1.5 Layout for half of a short (low high beta function-L) ID straight section, with reflection symmetry on left side.

Two slow horizontal and vertical closed-orbit correction magnets are included in each ID straight section (some also include a skew quadrupole winding). For the purposes of this design, we assume independent corrector magnets, as shown in Figures 3.1.4 and 3.1.5. Also shown are two beam position monitors to be used for closed-orbit correction. When a user ID is installed in the ring, it is assumed that two pairs of fast horizontal and vertical correctors and a pair of user BPMs may also be installed. These will be optimized for the aperture of the ID vacuum chamber to yield increased sensitivity to orbit motion and the increased frequency of correction for fast orbit motion required for the ID beamline. To accomplish this will require

some advanced engineering, but there is adequate drift space provided. The FHVCs and UBPMs will be used as part of a global feedback system to provide submicron photon beam stability up to 100 Hz. Since the four FHVCs will provide a closed bump, the possibility of adding a photon beam position signal to the feedback system will also be available, without that signal impacting the beam for other users. Also shown in Figure 3.1.4 is a skew quadrupole in one of the HVC corrector magnets. This is one of two families of skew quadrupoles (see Figure 3.1.6 for the second family) and is used to correct the vertical coupling of the horizontal and vertical betatron phase space resulting from alignment of the dipoles and quadrupoles in the ring.

Figure 3.1.6 shows the magnet layout for the dispersion region of the lattice with the dipoles included. This region has four quadrupoles in two families and three chromatic sextupoles in two families. These magnets give some flexibility for optimizing the dispersion function for reduced chromatic sextupole strength. The two chromatic sextupoles allow the linear chromaticity to be tuned, while also reducing the 2nd order chromaticity. Space has been provided between the dipole and the vertically focusing quadrupole in order to accommodate a Three Pole Wiggler. Although the drift for the TPW is provided symmetrically around the dispersive section, only the location closest to the dipole could have a TPW installed. These TPW (≤ 15) will provide source points for hard X-ray beams, for support of migrated NSLS user beamlines. As in the ID straight sections, two BPMs are included close to the quadrupoles near the ends of the girder. This is to provide improved alignment of the magnets on the girder using a beam based alignment of the BPM to the quadrupoles magnetic center. A third BPM (electrodes only) is included near the QF1 quadrupole (near the maximum dispersion point). This BPM will be used for accelerator physics measurements of the dispersion and beta functions, when needed, and could improve the orbit correction for large alignment or settlement errors. Also included are two discrete correctors (FHVC) that will be used for static and fast global orbit correction. These correctors are not symmetric about the dispersion section, in order to allow extraction of the damping wiggler beams and space for insertion of a three pole wiggler (TPW). These locations in the lattice for the TPW's will provide up to 15 possible beam sources for hard X-ray beam lines that can be migrated from the existing NSLS-Xray ring. Also show in one of the FHVC correctors is the location of one family of skew quadrupoles for coupling correction and vertical emittance control, see Section 3.1.2.?

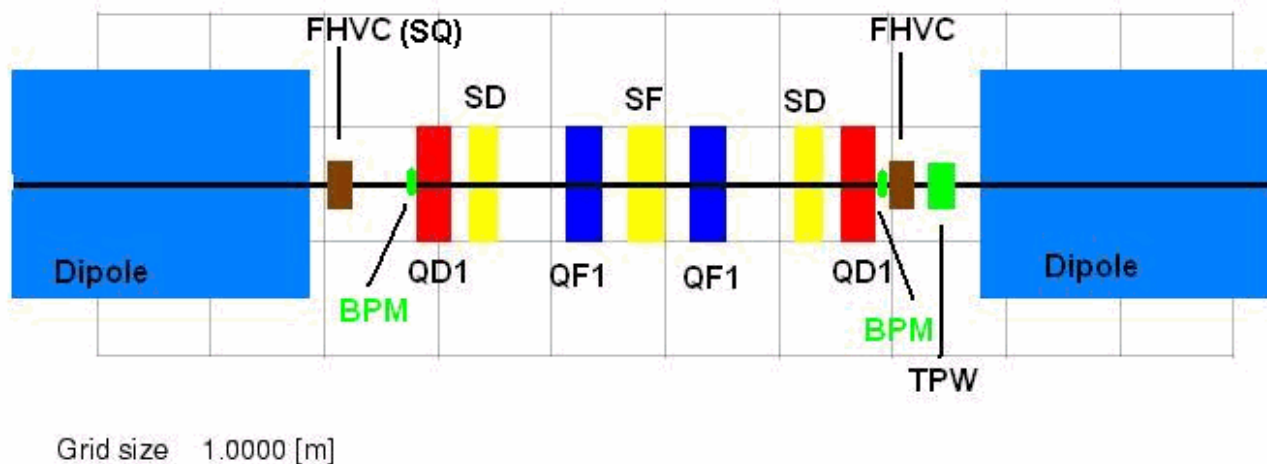


Figure 3.1.6 Layout for the dispersion section, including the two dipole magnets.

Table 3.1.4 lists a summary of the basic storage ring magnets and BPMs in the lattice design and for closed-orbit control. Also included are alignment tolerances for these magnets.

Table 3.1.4 List of Magnets, tolerances and BPMs for the NSLS-II Storage Ring.

Qty.	Magnet Type	Length [m]	B, B', B" [T,T/m,T/m ²]	Alignment Tol.
60	Dipole	2.62	0.4, 0, 0	0.1 mm, 0.5 mrad
270	Quadrupole (S)	0.25	0, 22, 0	0.03 mm, 0.2 mrad
30	Quadrupole (L)	0.40	0, 22, 0	0.03 mm, 0.2 mrad
30	Sextupole (L)	0.25	0, 0, 500	0.03 mm, 0.2 mrad
270	Sextupole (S)	0.20	0, 0, 500	0.03 mm, 0.2 mrad
180(210)	BPM readouts (positions)	0.05		0.1 mm, 0.2 mrad
120	H&V Fast Correctors(SS)	0.30	0.027, 0	0.1 mm, 0.2 mrad
60	H & V Slow Correctors	0.20	0.04, 0	0.1 mm, 0.2 mrad
150	Magnet girders			0.1 mm, 0.5 mrad

The alignment and field tolerance errors are still being studied further. However, initial testing of the lattice with tolerance that has been achieved at other light sources has shown the DA is robust for individual errors. As with most synchrotrons light sources, the closed-orbit amplification factors contribute the most significant tolerance to be handled. COAFs give the RMS closed-orbit distortion around the ring per unit of RMS alignment error (assumed to be a random Normal distribution) for all the quadrupoles in the ring. The COAF for this lattice is shown in Figure 3.1.7 for one cell and has an average value in each plane of greater than 50. This means a 100 μm RMS alignment error in the quadrupoles will yield an average closed-orbit distortion of >5 mm. This closed orbit error in the sextupoles contributes to a nonlinear focusing error in the lattice, which breaks the sextupole strength settings that yield the large DA.

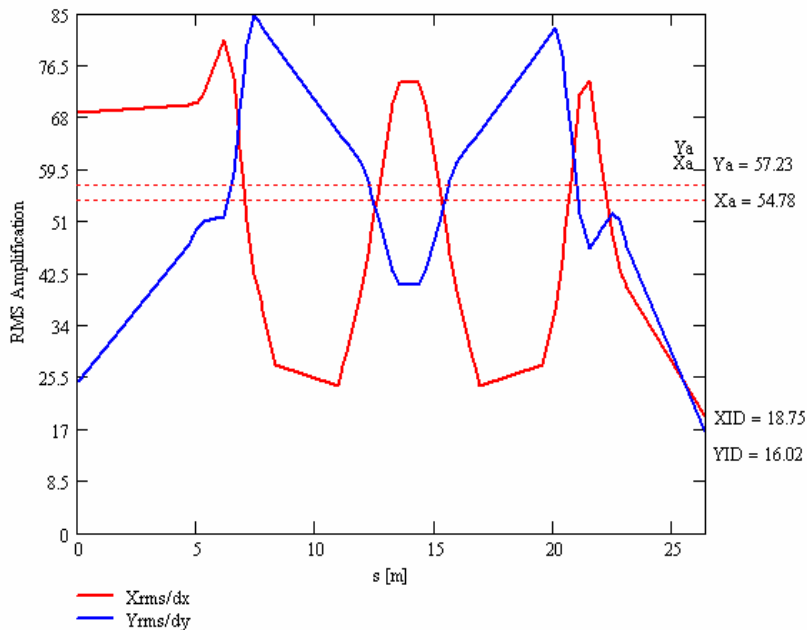


Figure 3.1.7 RMS expected closed-orbit amplification factors for random alignment errors in the quadrupoles of the lattice. Listed are the average amplification factors (X_a, Y_a) and values at the short ID (X_{ID}, Y_{ID}).

Figure 3.1.8 shows the impact of random quadrupole alignment errors of 100 μm that are corrected using the 6 BPMs and the 6 correction magnets per cell. We have corrected the orbit to the BPMs with an assumed no BPM noise or offset from the reference orbit. The corrected orbit DA for 20 different starting seeds (lattice layout errors) is shown with the average and RMS spread of the DA, together with the extreme values. The DA remains adequately large and is more than sufficient for injection and lifetime.

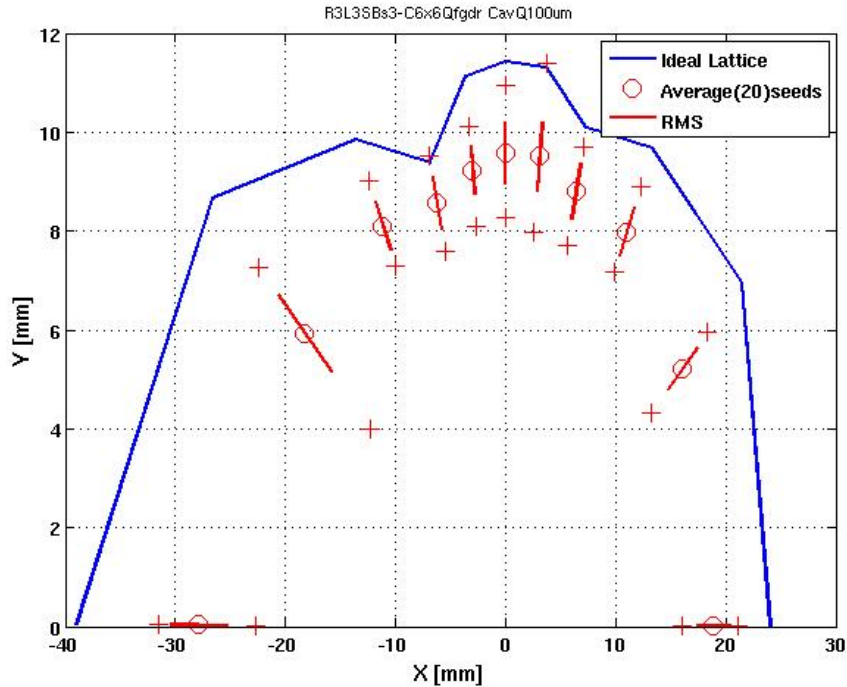


Figure 3.1.8 The DA (average, RMS and extremes values) for the lattice with 100 μm quadrupole alignment errors corrected to ideal BPMs located at the quadrupoles. It includes synchrotron oscillations, and the DA is tracked for 1 K turns around the lattice. The bare DA is also shown.

Adding a 30 μm random alignment tolerance of the BPM-to-quadrupole magnetic center yields little additional reduction of the DA, as shown in Figure 7.1.3, and is more than adequate. This random offset of the BPMs is equivalent to a BBA resolution of the BPM center relative to the quadrupole magnetic center, which could be much better than the 30 μm assumed in Figure 3.1.9, as described below.

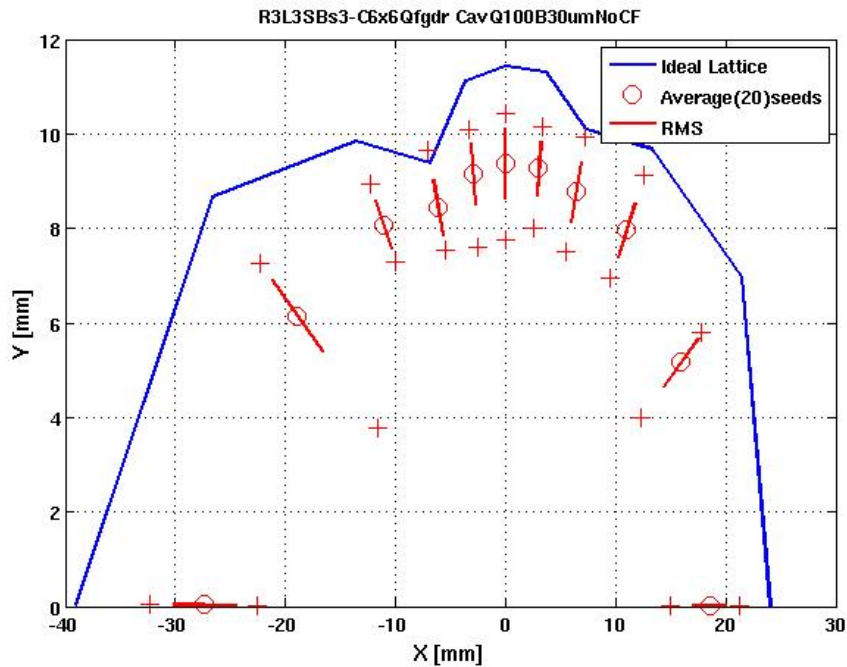


Figure 3.1.9 DA with 100 μm quadrupole alignment tolerances corrected with 30 μm BBA tolerance for BPMs (20 random seeds shown, with synchrotron oscillations).

We have assumed that the BPMs are close to the quadrupoles, since they are the source of the closed-orbit distortions in the sextupole magnets that cause the reduction of the DA. The two BPMs on a girder are aligned to the centers of the neighboring quadrupole magnetic center using the BBA procedure, which has become

common at many synchrotrons. This method uses a beam bump to vary the beam position (x, y) in the quadrupole and its neighboring BPM. If that quadrupole has its strength modulated (ΔK_2), then the magnitude of the closed-orbit distortion measured by the BPMs is (X_m, Y_m). The BPM reading that yields a null in (X_m, Y_m) is then the magnetic center of this quadrupole, as measured by the BPM. With two BPMs on a girder, the beam can be magnetically centered to all elements on the girder using the magnetic alignment instruments: pulsed wire, vibrating wire, and/or rotating coils. Therefore we specify the alignment tolerances for the magnetic elements in terms of: 1) an alignment tolerance of centers one to another, 2) alignment of girder ends one to another and a common roll error of the girder, and 3) a BBA alignment tolerance of the BPMs to their neighboring quadrupole. The sensitivity of the closed-orbit distortion amplitude to the quadrupole modulation ($\Delta K_2 L$) and beam offset relative to the quadrupole center position, (x_c, y_c), is given by:

$$X_m(s) = \frac{\sqrt{\beta_x(s) \beta_x(\text{quad})}}{2 \sin(\pi Q_x)} (\Delta K_2 L) x \geq 5.2 (\Delta K_2 L) x \quad (3.1.1-8)$$

and

$$Y_m(s) = \frac{\sqrt{\beta_y(s) \beta_y(\text{quad})}}{2 \sin(\pi Q_y)} (\Delta K_2 L) y \geq 7.2 (\Delta K_2 L) y \quad (3.1.1-9)$$

where we assume the smallest beta function at a quadrupole and the average beta function at the BPMs. We assume that the closed-orbit amplitude is measurable to the resolution of the BPMs, $\sim 1 \mu\text{m}$, and the modulation is 3% of the quadrupole strength; the magnetic center should be measured in the neighboring BPM with an accuracy of better than

$$\sigma_{x_c} \leq 8 \text{ to } 10 \mu\text{m} \quad \text{and} \quad \sigma_{y_c} \leq 15 \mu\text{m}. \quad (3.1.1-10)$$

Consequently, the random tolerances on the magnet-to-magnet alignment in Table 3.1.1 will be greater than the BBA resolution. However, we have assumed the BBA resolution of $30 \mu\text{m}$ in Figure 3.1.9, which is two to three times greater than achievable.

The impact of the larger values for the girder alignment tolerances were evaluated assuming that either end of the girder is aligned to an RMS level (random Normal distribution $\Delta x, \Delta y$). This misalignment of the girders contributes a correlated misalignment error in all magnets and BPMs on the girder. The sensitivity to this type of error is shown in Figure 3.1.10, where the Girder Amplification Factor is shown. The GAF is defined as the RMS closed-orbit distortion per unit of RMS girder misalignment. This shows a reduction in the averaged COAF (Figure 3.1.7) by a factor of 2X (H) and 3X (V). The GAF values at the center of the short straight section are 9.4 in the horizontal and 4.3 in the vertical plane, compared to 18.8 and 16.0 for the COAF, respectively. However, correcting for the assumed $100 \mu\text{m}$ girder alignment tolerances yields almost complete restoration of the DA (without BPM errors), since the correlations of the quadrupole misalignments are easier to remove by BBA alignment to the quadrupoles on the misaligned girders.

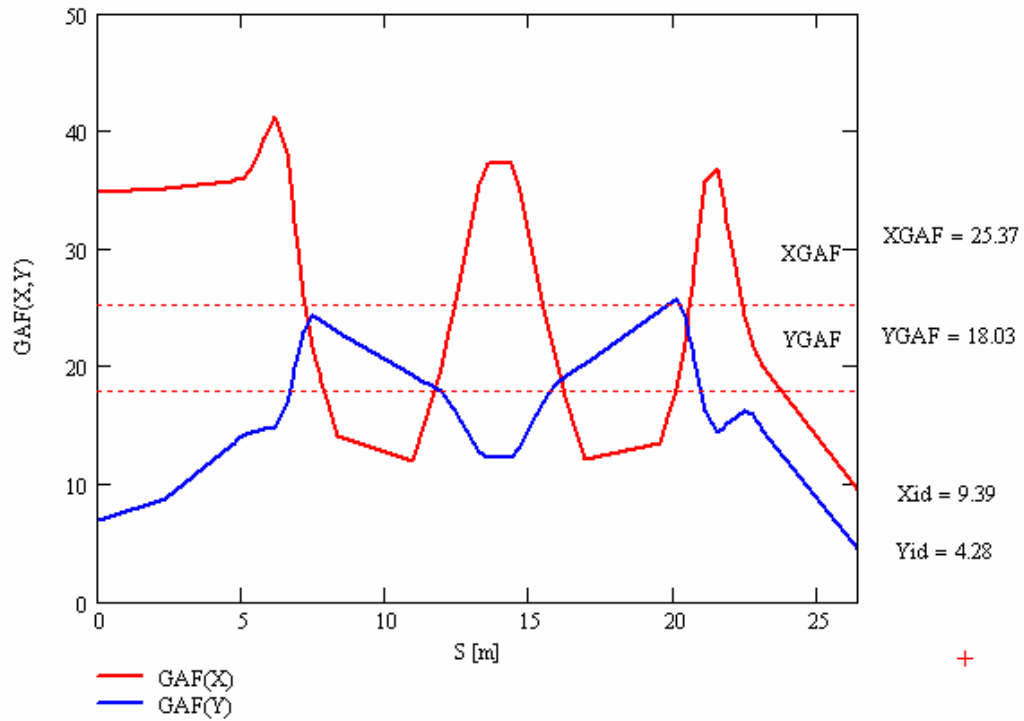


Figure 3.1.10 Girder Amplification Factors for one period of the storage ring. The average GAF values are 25 (H) and 18 (V) with values for the short ID of 9.4(H) and 4.3(V).

The corrected DA is shown in Figure 3.1.11 for 100 μm RMS random girder alignment tolerances, where no other errors are assumed in the BBA resolution for the BPMs, nor any quadrupole misalignment errors on the girder.

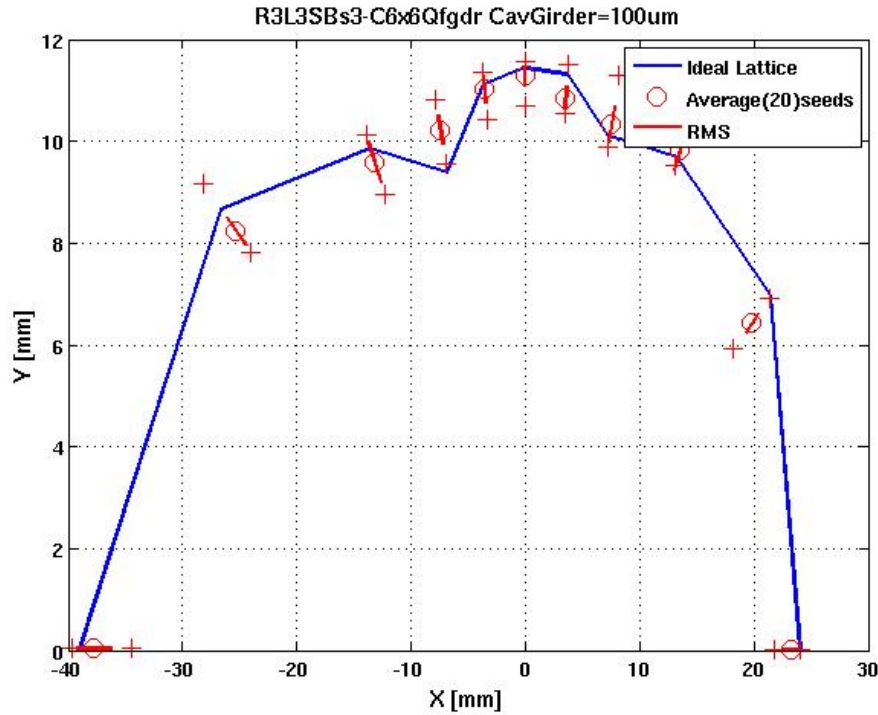


Figure 3.1.11 DA for 20 seeds (lattices) with 100 μm RMS girder alignment tolerances corrected using the BPMs with zero error in the BBA resolution.

The impact on the DA of all the misalignment tolerance, listed in Table 3.1.4 and including a 10 μm BBA resolution, as given by Eq. 3.1.1-10, is shown in Figure 3.1.12. Although there is significant reduction of the DA for this level of tolerance errors, it is well outside the physical aperture of the ring. Relaxing the alignment tolerances is still acceptable but will make the field and multipole tolerances on the magnets even tighter and will have a significant cost impact. The complete analysis of the DA with all alignment and field tolerances is presented in Section 3.1.2. The COAF and GAF presented here will also be used to estimate the orbit stability resulting from magnet vibrations in Section 7.2.2.

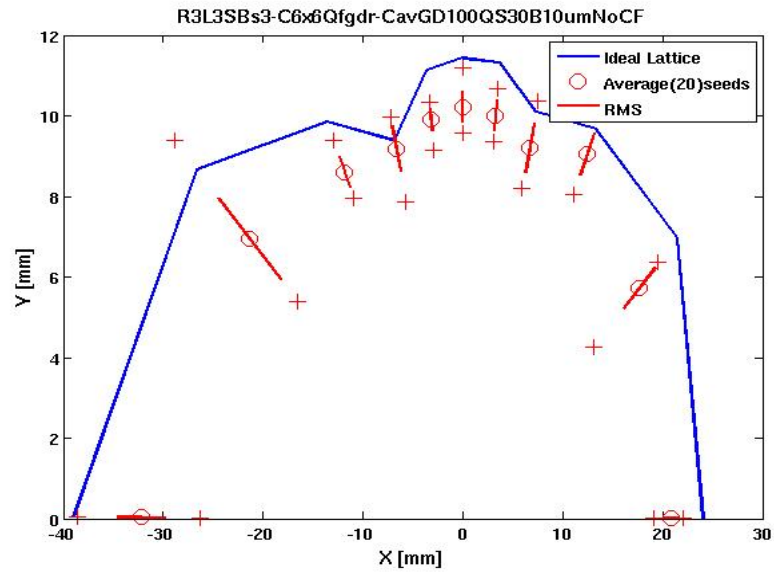


Figure 3.1.12 DA for 20 seeds (lattices) with all alignment tolerances included and using a 30 μm BBA resolution for BPMs. No quadrupole rotations are included.

3.1.2 Nonlinear Dynamics

3.1.2.1 Guidelines

One of the main design challenges for a strongly focusing lattice is to obtain adequate dynamic aperture for injection and Touschek lifetime¹. As the required strength of the chromatic sextupoles increases, the DA can be improved by introducing extra families of geometric and chromatic sextupoles. However, once the sextupoles become too strong, this is no longer feasible. Eventually, cross terms generate higher-order terms, and when more families are introduced, the lattice will become pathological [3.1.5]. To avoid this, the following guideline has been provided for the linear optics design:

- horizontal chromaticity per cell, $\xi_x \leq 3$,
- peak dispersion, $\eta_x \geq 0.3$ m.

Similarly, we have adopted the guidelines for the DA summarized in Table 3.1.5. This is a conservative approach² to satisfy the requirements for the injection aperture for efficient top-off, as well as to ensure sufficient Touschek lifetime.

Table 3.1.5 Dynamic Aperture Guidelines.

	Horizontal and Vertical Dynamic Acceptance [mm-mrad]	Horizontal Dynamic Aperture [mm]	Momentum Acceptance [%]
Bare lattice (2.5 degrees of freedom ³)	~25	±20	±3
"Real" lattice (3 degrees of freedom ⁴)	~20	±15	±3

This also provides some leeway for magnetic alignment and field tolerances, and nonlinearities due to insertion devices, which, when included, the former perturb the symmetry of the linear optics and diminish the cancellation of the nonlinear effects whereas the latter contribute directly, reducing the DA.

3.1.2.2 Sextupole Scheme

The linear lattice has a chromaticity of $\xi_{x,y}^{(1)} \sim (-100, -37)$ and a natural momentum spread of $\sim 0.1\%$ leading to a tune spread of $\Delta\nu_{x,y} \sim (0.1, 0.04)$, which must be corrected⁵. The linear chromaticity is given by

$$\xi_{x,y}^{(1)} = \mp \frac{1}{4\pi} \sum_{k=1}^N [(b_2L)_k - 2(b_3L)_k \eta_{x,k}] \beta_{(x,y),k}, \quad (3.1-8)$$

¹ For medium energy rings: ~ 3 GeV.

² Based on the experience from the Swiss Light Source conceptual design, i.e., a highly nonlinear lattice [3.1.6] with straightforward commissioning [3.1.7], excellent top-off injection efficiency [3.1.8], and stability [3.1.9].

³ With δ (momentum deviation) treated as a parameter, i.e., the adiabatic approximation.

⁴ In particular, with synchrotron oscillations.

⁵ Moreover, a positive linear chromaticity in the range 0–5 is required to stabilize the head-tail instability.

where (b_2L) , (b_3L) are the integrated quadrupole and sextupole strengths, and β and η are the beta function and dispersion, respectively at the quadrupoles and sextupoles, k . The driving terms for linear chromaticity from sextupoles are shown in Figure 3.1.7. Two mirror symmetric chromatic families are introduced inside the dispersion section and 3+4 geometric families in the short and long straight sections, i.e., a total of 9 sextupole families. While one of the families in the latter tends to be weak, it has been left as place holders until a more comprehensive optimization has been completed. Individual power supplies for all the quadrupoles are provided, whereas the sextupole families are powered in groups of five; to allow for local optics correction [3.1.10–3.1.16] and control of residual nonlinear resonances. The latter by analyzing the betatron sidebands from turn-by-turn BPM data and controlling them with the inverted “sextupole response matrix” [3.1.17-3.1.19].

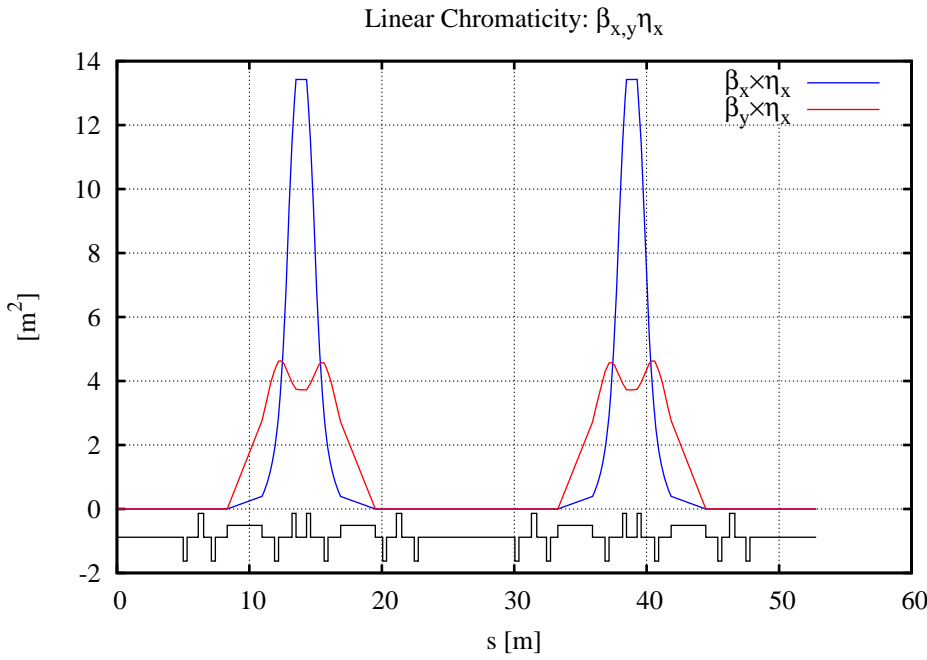


Figure 3.1.7 Driving terms for zeroing linear chromaticity with sextupoles, $\beta_{x,y} \eta_x$.

After linear chromaticity has been zeroed, the residual (nonlinear) chromaticity is one of the limiting factors. The second-order chromaticity is given by [3.1.17]:

$$\xi_{x,y}^{(2)} = -\frac{1}{2}\xi_{x,y}^{(1)} \pm \frac{1}{8\pi} \sum_{k=1}^N \left\{ 2(b_3L)_k \frac{\partial \eta_{x,k}}{\partial \delta} \beta_{(x,y),k} \mp [(b_2L)_k - 2(b_3L)_k \eta_{x,k}] \frac{\partial \beta_{(x,y),k}}{\partial \delta} \right\} \quad (3.1-9)$$

where

$$\frac{\partial \eta_{x,j}}{\partial \delta} = -\eta_{x,j} + \frac{\sqrt{\beta_{x,j}}}{2 \sin(\pi \nu_x)} \sum_{k=1}^N [(b_2L)_k - (b_3L)_k \eta_{x,k}] \eta_{x,k} \sqrt{\beta_{x,k}} \cos(\mu_{j \rightarrow k, x} - \pi \nu_x)$$

and

$$\frac{\partial \beta_{(x,y),k}}{\partial \delta} = \pm \frac{\beta_{(x,y),j}}{2 \sin(2\pi\nu_x)} \sum_{k=1}^N [(b_2 L)_k - 2(b_3 L)_k \eta_{x,k}] \beta_{(x,y),k} \cos(2\mu_{j \rightarrow k, (x,y)} - 2\pi\nu_x)$$

The driving terms are shown in Figures 3.1.8 and 3.1.9. Clearly, small variations of the sextupole locations may lead to large changes of the nonlinear chromaticity⁶. In particular, the quite large momentum dependence of the optics functions $\eta_x(\delta)$ and $\beta_{x,y}(\delta)$ leads to considerable residual second and cubic terms in the horizontal chromaticity [3.1.19]. Therefore, all the sextupole families are chromatic, i.e., part of the reduction of the nonlinear chromaticity originates from the reduction of the latter with the “geometric” sextupoles, see Figures 3.1.10 and 3.1.11. The former is not reduced, because there are only two chromatic families.

⁶ As noted from numerical simulations for the DIAMOND conceptual design [3.1.18].

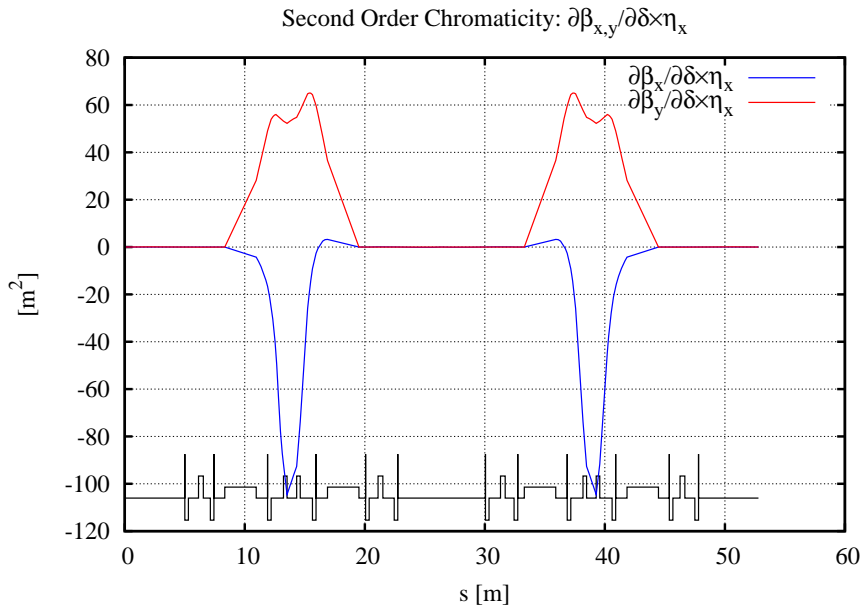


Figure 3.1.8 Driving terms for second-order chromaticity, $\partial\beta_{x,y}/\partial\delta \times \eta_x$ (no sextupoles).

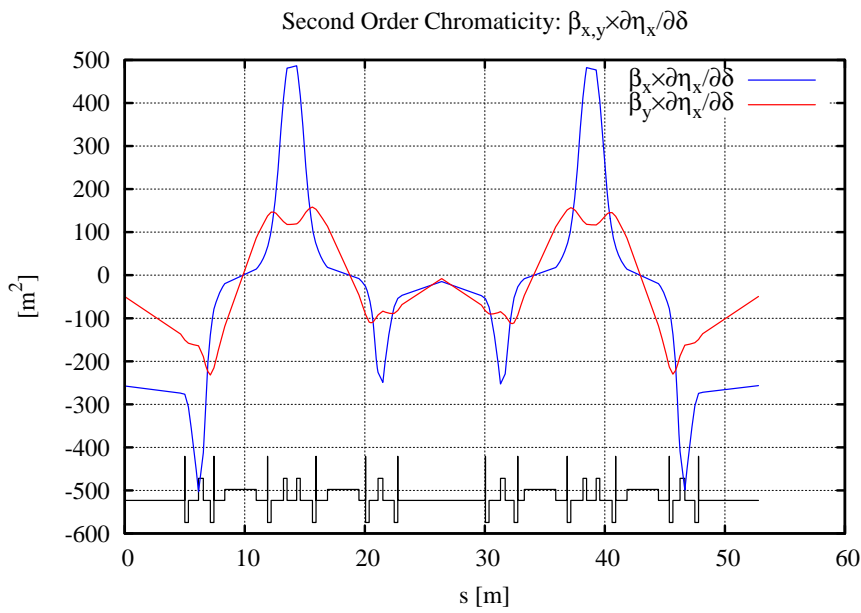


Figure 3.1.9 Driving terms for second-order chromaticity, $\beta_{x,y} \partial\eta_x/\partial\delta$ (no sextupoles).

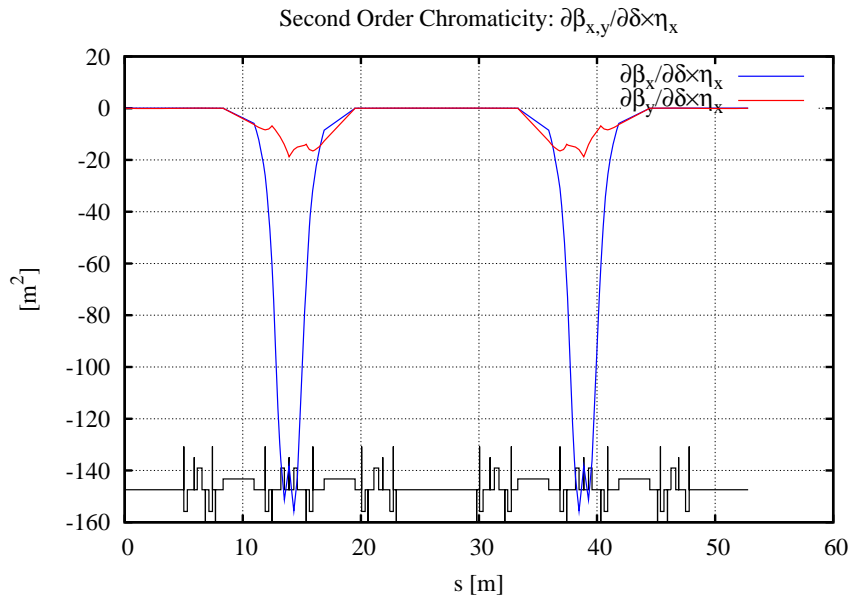


Figure 3.1.10 Driving terms for second-order chromaticity, $\partial\beta_{x,y}/\partial\delta \times \eta_x$ (with sextupoles).

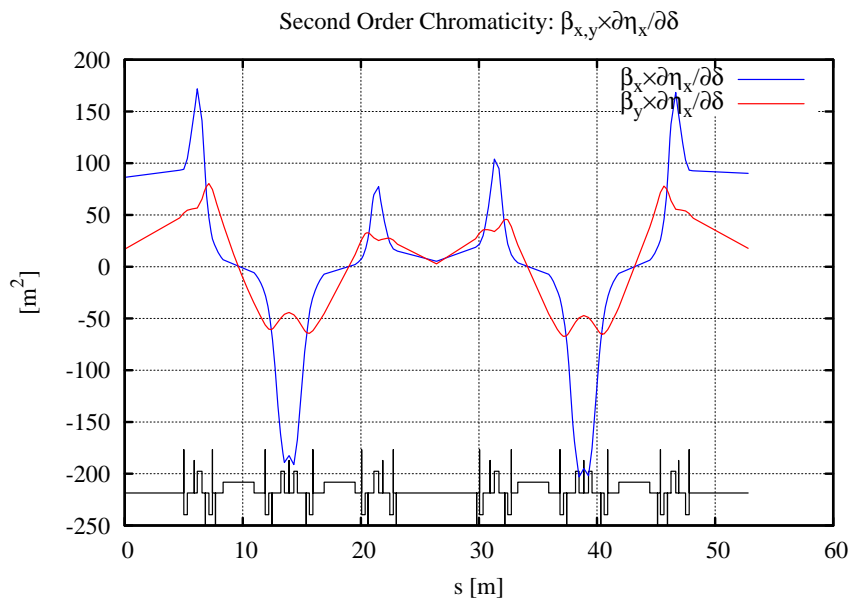


Figure 3.1.11 Driving terms for second-order chromaticity, $\beta_{x,y} \partial\eta_x/\partial\delta$ (with sextupoles).

3.1.2.3 Dynamic Aperture Optimization

The Poincaré map has the formal Lie series representation [3.1.17]:

$$\mathcal{M} = e^{:h:} \mathcal{M}_{\text{linear}} \quad (3.1-10)$$

where $\mathcal{M}_{\text{linear}}$ is the linear one-turn map, and the Lie generator h represents the nonlinear kicks parallel transported to the lattice entrance. It can be written in the normal form⁷ [3.1.22]

$$\mathcal{M} = \mathcal{A}^{-1} \dots e^{g(\bar{J}, \bar{\phi})} e^{k(\bar{J})} e^{-g(\bar{J}, \bar{\phi})} \mathcal{A},$$

where $[\bar{J}, \bar{\phi}]$ are the action-angle variables, \mathcal{A} is a linear transformation to Floquet space⁸, $g(\bar{J}, \bar{\phi})$ a canonical transformation, and $k(\bar{J})$ a nonlinear rotation. A nonlinear pseudo-invariant is obtained from

$$\mathcal{K}(\bar{J}, \bar{\phi}) = e^{g(\bar{J}, \bar{\phi})} k(\bar{J}) = \text{cst.} \mathcal{A}.$$

In particular, the terms are of the form:

$$\mathcal{K}_i \propto \frac{J_x^{a_x} J_y^{a_y}}{\sin(\pi(n_x \nu_x + n_y \nu_y))} \quad (3.1-11)$$

where $[n_x, n_y]$ are integers, $[a_x, a_y]$, and $[\nu_x, \nu_y]$ the cell tune; note the resonance denominator. For a validation of the goodness of the pseudo-invariant as a description of the nonlinear dynamics see [3.1.23].

In contrast to the linear case, the long-term stability now depends on: $\mathcal{K}(\bar{J}, \bar{\phi})$, the cell tune, and the initial conditions. In other words, for a systematic approach, the pseudo-invariant and the working point have to be optimized simultaneously. We have implemented a generalized (partial) third-order achromat by introducing 9 sextupole families to the super-period, and minimized the coefficients of $\mathcal{K}(\bar{J}, \bar{\phi})$ over two super-periods, i.e., four DBA cells, for a range of cell tunes. At each working point with optimized sextupole strengths, we evaluated the DA by tracking. To the second order in the sextupole strengths, there are:

- 2+3+2 chromatic terms
- 5+8 geometric terms (modes)
- 3+3 tune shift with amplitude and momentum

This is a total of 26 terms⁹ (see Table 3.1.6 for an inventory). These are minimized by varying the sextupole strengths using the following automated method¹⁰ [3.1.5]:

1. For a given cell tune, the pseudo-invariant $\mathcal{K}(\bar{J}, \bar{\phi})$ and its parametric dependence on the sextupole strengths (i.e., the Jacobian) are calculated for $J_{x,y}$ and δ at the anticipated DA.
2. The norm of $\|\mathcal{K}(\bar{J}, \bar{\phi})\|$ is minimized¹¹ and the DA is evaluated by tracking.
3. The cell tune is changed by using a grid of working points¹² from the optics optimizations, and steps 1–3 are repeated.

⁷ Recursively, i.e., to arbitrary order, by Lie series and Truncated Power Series Algebra (TPSA).

⁸ Normalized phase space.

⁹ The corresponding overconstrained system of nonlinear equations for the sextupole strengths can be minimized because of symmetry and the fact that the higher order terms are due to cross terms of the lower order.

¹⁰ Feasible only because of the use of symmetry and the fact that the higher order terms appear due to cross terms of the lower order.

¹¹ In particular, a least-square of the individual terms.

¹² Each working point meets all the optics requirements.

The off-momentum aperture is included by using a weighted average for the DA at $\delta = 0, \pm 3\%$. A robust solution is obtained by establishing a broad local maximum for the DA see Figure 3.1.12¹³. The tune scan is then redone with engineering tolerances included in the tracking, see Figure 3.1.13¹⁴, which has a broad maximum centered near $\nu_{x,y} \approx [32.87, 15.67]$. The resulting DA is shown in Figure 3.1.14, for $\delta = 0, \pm 3\%$. The linear chromaticity is set to $\xi_{x,y}^{(1)} \approx [2.0, 2.0]$, and the residual nonlinear chromaticity is shown in Figure 3.1.15.

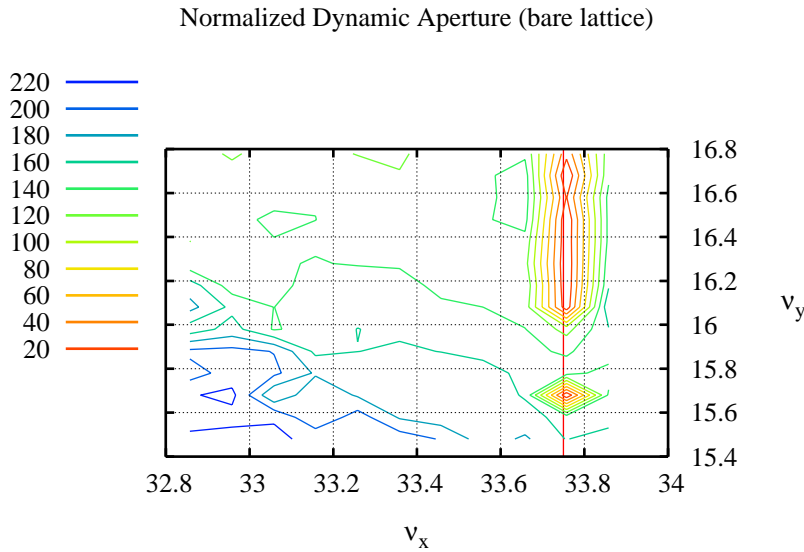


Figure 3.1.12 Normalized DA ($\text{Area}/\sqrt{\beta_x\beta_y}$) versus tune per super-period (bare lattice).

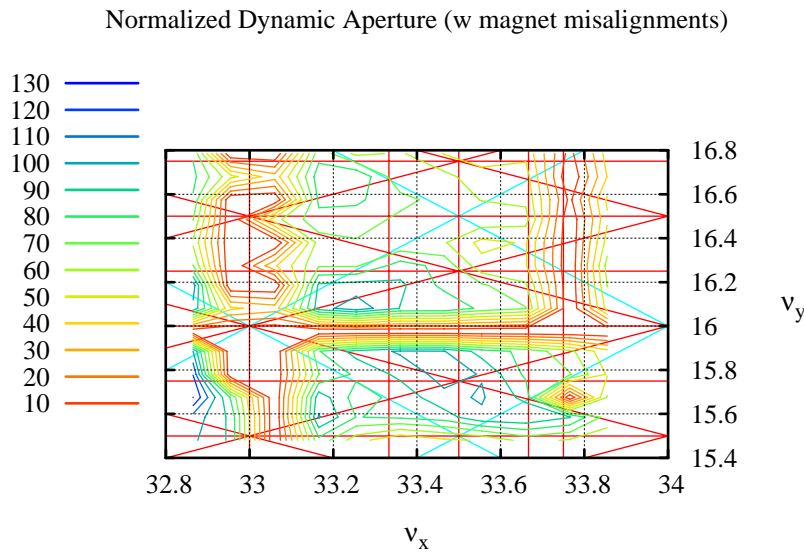


Figure 3.1.13 Normalized DA ($\text{Area}/\sqrt{\beta_x\beta_y}$) versus tune per super-period (with errors).

¹³ The red line shows the (systematic) $4\nu_y = 135$ resonance.

¹⁴ The red lines shows the resonances up to first order in the sextupole strength.

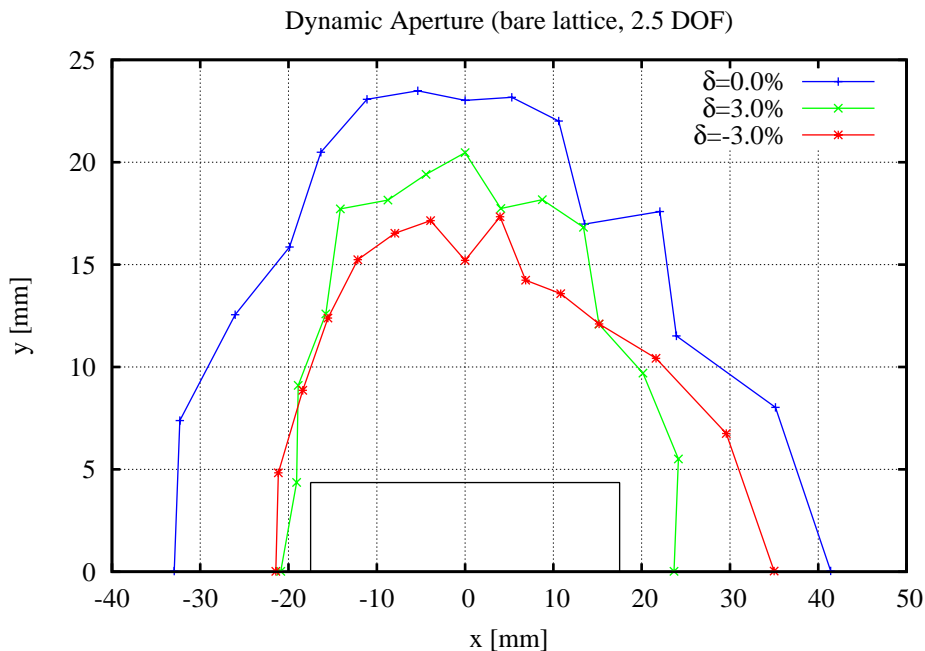


Figure 3.1.14 DA for $\delta = 0, \pm 3\%$ for the optimized tune and sextupoles at the center of the long straight section (i.e., at injection), $\beta_{x,y} = [20.8, 3.4]$ m for $\nu_{x,y} \approx [32.833, 15.616]$.

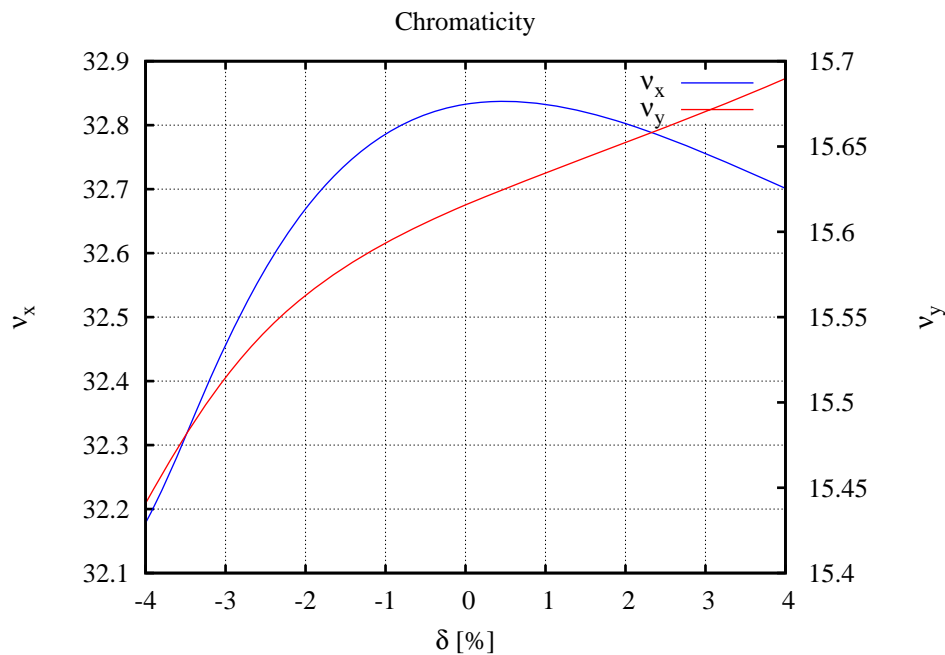


Figure 3.1.15 Residual nonlinear chromaticity for the optimized tune and sextupoles for $\xi_{x,y}^{(1)} \approx [2.0, 2.0]$.

As mentioned earlier, the horizontal chromaticity has a substantial quadratic and cubic term originating from $h_{10002}, h_{20001}, h_{00201}$, which generate momentum dependence of the optics function. The amplitude-dependent tune shifts are shown in Figures 3.1.16 and 3.1.17, and the balancing of the pseudo-invariant terms

is summarized by Table 3.1.3. Moreover, the crossing of the linear coupling resonances during synchrotron oscillations should be avoided (Figure 3.1.18); otherwise, the Touschek lifetime is likely to be affected.

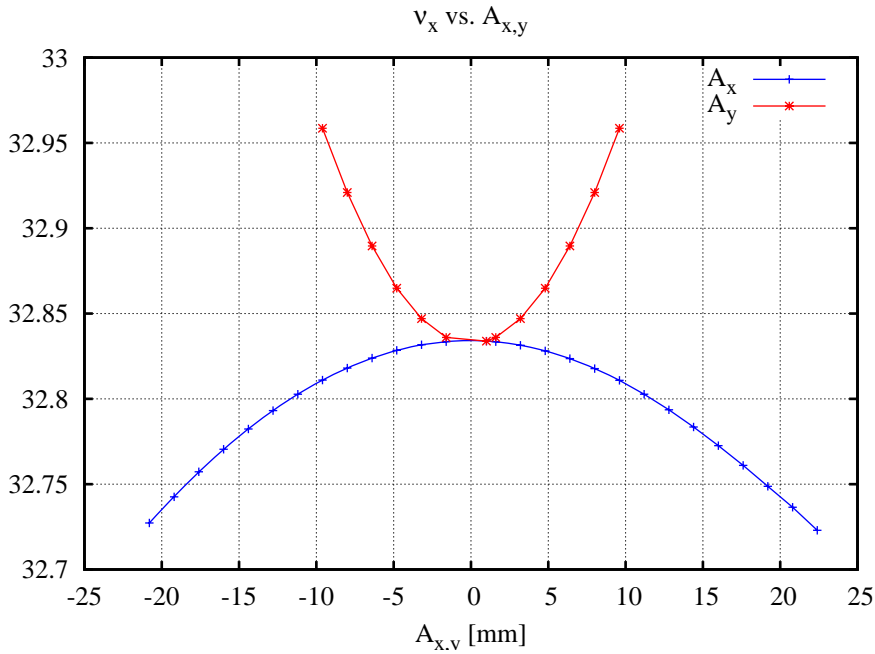


Figure 3.1.6 Horizontal tune, v_x , vs. transverse amplitude (x_0, y_0) at the long straight section for $A_x = (x_0, y_0 \sim 0)$ and $A_y = (x_0 \sim 0, y_0)$.

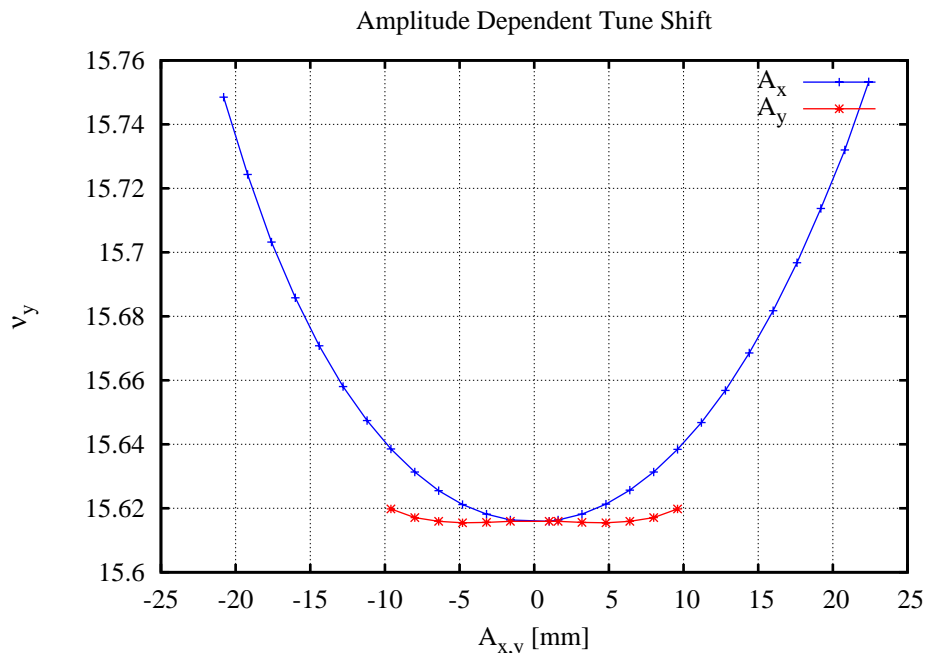


Figure 3.1.17 Vertical tune, v_y , vs. transverse amplitude (x_0, y_0) at the long straight section for: $A_x = (x_0, y_0 \sim 0)$ and $A_y = (x_0 \sim 0, y_0)$.

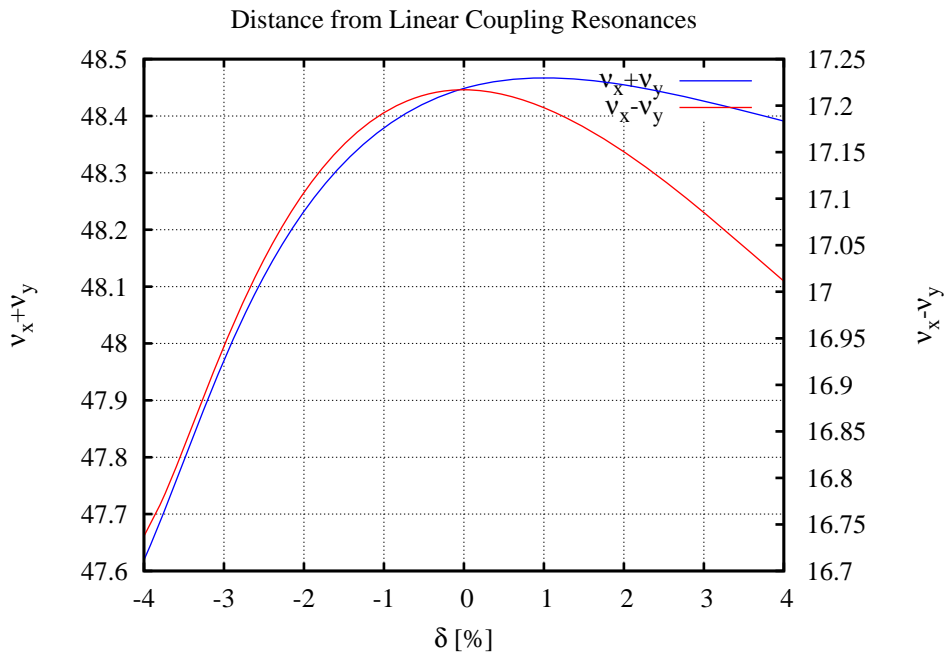


Figure 3.1.18 Distance to the linear coupling resonances.

A frequency map [3.1.15] shows diffusion rate as a function of amplitude or tunes. The diffusion rate, as defined by

$$D(v_x, v_y) = \log_{10} \left(\sqrt{(\Delta v_x)^2 + (\Delta v_y)^2} \right), \quad (3.1-12)$$

is an indicator of chaotic behavior, where Δv is the tune change between the first and second half of the particle tracking with initial amplitude $J_{x,y}$. The frequency map for the optimized working point and sextupole settings for the selected linear chromaticity is shown in Figure 3.1.19, with the diffusion parameter plotted as a color-weighted value. Similarly, a frequency map for x vs. δ is shown in Figure 3.1.20; since crossing of leading order resonances for the Touschek/synchrotron oscillation/radiation damping process must be avoided.

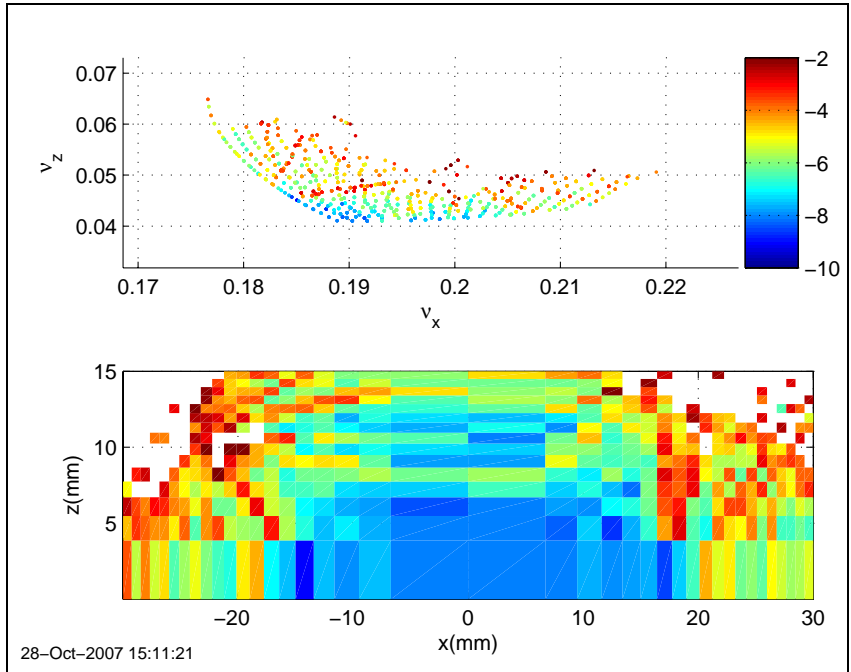


Figure 31.19 Frequency map vs. transverse amplitudes at the Long Straight Section, $\beta_{x,y} = (20.8, 3.4)$ m.

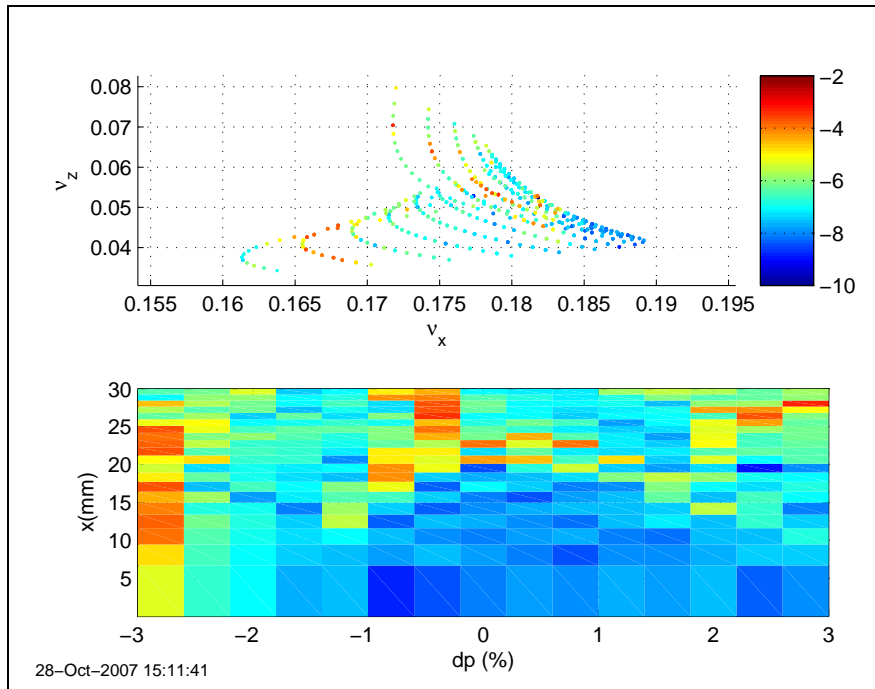


Figure 3.1.20 Frequency map vs. momentum and horizontal amplitude at the Long Straight Section, $\beta_{x,y} = (20.8, 3.4)$ m.

Table 3.1.6 Residual Normalized Lie Generators.

Lie Generator	Effect	Normalized Value
$ h_{11001} $	$\partial v_x / \partial \delta$	5.4×10^{-7}
$ h_{00111} $	$\partial v_y / \partial \delta$	1.5×10^{-6}
$ h_{10002} $	$\partial \eta_x / \partial \delta$	2.0×10^{-6}
$ h_{20001} $	$\partial \beta_x / \partial \delta$	2.4×10^{-6}
$ h_{00201} $	$\partial \beta_y / \partial \delta$	1.7×10^{-6}
$ h_{21000} $	v_x	8.6×10^{-7}
$ h_{10110} $	v_x	9.2×10^{-7}
$ h_{30000} $	$3v_x$	7.0×10^{-7}
$ h_{10020} $	$v_x - 2v_y$	3.7×10^{-6}
$ h_{10200} $	$v_x + 2v_y$	9.8×10^{-7}
$ h_{20110} $	$2v_x$	3.1×10^{-7}
$ h_{31000} $	$2v_x$	5.0×10^{-8}
$ h_{40000} $	$4v_x$	7.3×10^{-7}
$ h_{20020} $	$2v_x - 2v_y$	1.5×10^{-6}
$ h_{20200} $	$2v_x + 2v_y$	5.1×10^{-8}
$ h_{11200} $	$2v_y$	6.0×10^{-7}
$ h_{00310} $	$2v_y$	3.9×10^{-7}
$ h_{00400} $	$4v_y$	1.7×10^{-7}
$ h_{22000} $	$\partial v_x / \partial J_x$	9.0×10^{-7}
$ h_{11110} $	$\partial v_{x,y} / \partial J_{y,x}$	3.8×10^{-6}
$ h_{00220} $	$\partial v_y / \partial J_y$	7.3×10^{-7}
$ h_{22001} $	$\partial^2 v_x / \partial J_x \partial \delta$	3.2×10^{-7}
$ h_{11111} $	$\partial^2 v_{x,y} / \partial J_{y,x} \partial \delta$	8.1×10^{-7}
$ h_{00221} $	$\partial^2 v_y / \partial J_y \partial \delta$	4.5×10^{-7}
$ h_{11002} $	$\partial^2 v_x / \partial \delta^2$	9.7×10^{-7}
$ h_{00112} $	$\partial^2 v_y / \partial \delta^2$	1.9×10^{-7}
$ h_{11003} $	$\partial^3 v_x / \partial \delta^3$	1.8×10^{-7}
$ h_{00113} $	$\partial^3 v_y / \partial \delta^3$	1.4×10^{-7}

3.1.2.4 Impact of Alignment and Field Tolerances on Dynamic Aperture

Systematic and random magnetic field errors further reduce the DA, and their impact has been evaluated by simulations. Figure 3.1.21 shows the impact on the DA as the random quadrupole gradient errors are increased for all the quadrupoles of the lattice. At a relative RMS error of $\Delta b_2/b_2 \approx 5 \times 10^{-4}$, they reduce the DA by $\sim 20\%$, which is taken as the tolerance level for the quadrupole powering errors.

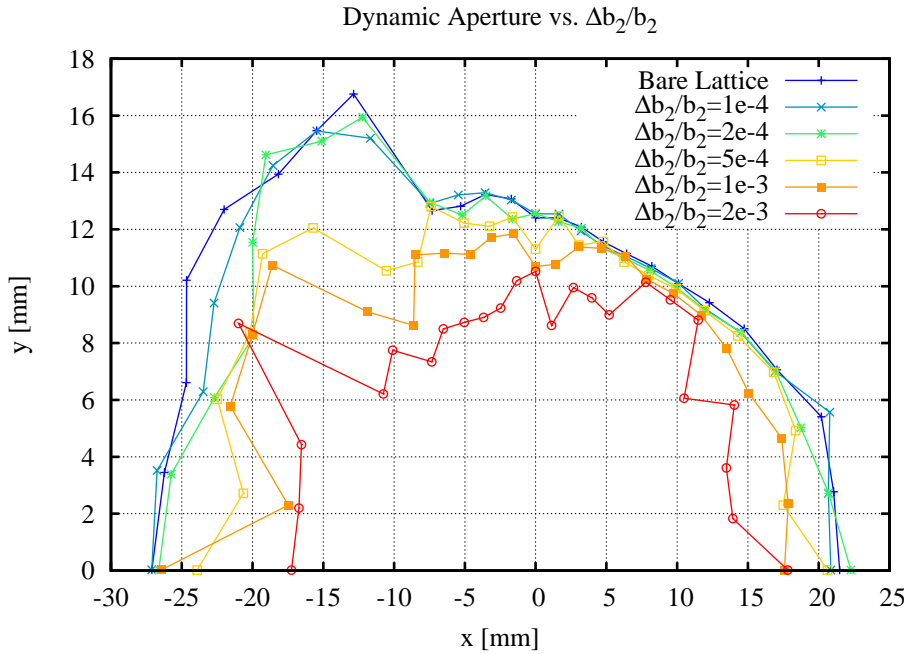


Figure 3.1.21 DA sensitivity versus the fractional gradient errors in the quadrupoles.

This reduction in DA originates from distortions of the linear optics at the sextupole magnets that perturb the influence of the carefully balanced sextupole strengths that were chosen to minimize the nonlinear driving terms. The resulting RMS beta and phase advance beats at the sextupoles can therefore be used as a tolerance level, regardless of their source [3.1.24]. These latter tolerance levels, as well as the gradient tolerance level, are listed in Table 3.1.7.

Table 3.1.7 Optics Tolerances for Robust DA of the NSLS-II Lattice.

Location	At the Quadrupoles	At the Sextupoles	
Parameter	$\left(\frac{\Delta b_2 L}{b_2 L}\right)_{\text{rms}}$	$\left(\frac{\Delta \beta_{x,y}}{\beta_{x,y}}\right)_{\text{rms}}$	$(\Delta v_{x,y})_{\text{rms}}$ $(\Delta x_{\text{cod}}, \Delta y_{\text{cod}})_{\text{rms}}$
Tolerance	$\sim 5 \times 10^{-4}$	$\sim (0.02, 0.03)$	$\sim (0.003, 0.01)$ $\sim (50, 50) \mu\text{m}$

Similarly, a tolerance level can be specified for the residual Closed-Orbit Distortions at the sextupoles, which introduce beta and phase advance beats proportional to the sextupole gradients times the COD offset. This impact on the DA was simulated by introducing random transverse alignment errors to all the sextupoles and is shown in Figure 3.1.22 vs. the RMS error. At a level of $\sigma_x = \sigma_y \sim 50 \mu\text{m}$, the DA area is reduced by about 20%. These RMS values can be taken as the tolerance level for the misalignments and residual COD at the sextupoles that must be maintained by the global orbit correction system (see Table 3.1.7).

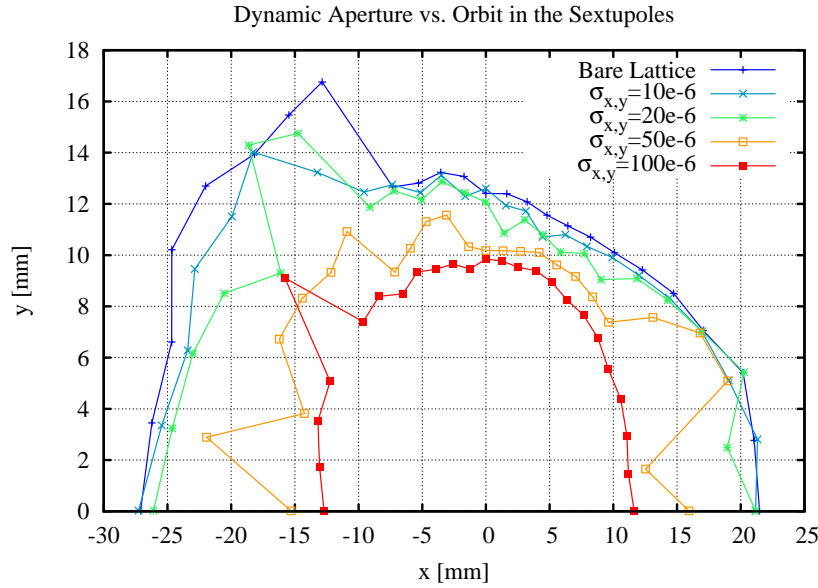


Figure 3.1.22 DA sensitivity to transverse alignment errors of the sextupoles.

Correspondingly, the required transverse magnet alignment tolerances are summarized in Table 3.1.8, assuming the COD errors are corrected using the seven BPMs and seven correctors of the lattice. Details on the global orbit correction scheme are given in Section 3.1.2.5.

Table 3.1.8 Transverse Magnet Alignment Tolerances.

	Δx RMS [μm]	Δy RMS [μm]	Roll RMS [m-rad]
Dipole	~100	~100	-0.5
Girder	~100	~100	-0.5
Quadrupoles	~30	~30	-0.2
Sextupoles	~30	~30	-0.2

The magnetic field error tolerances are specified in terms of the normal and skew multipole coefficients (b_n, a_n), defined by the normalized transverse magnetic field expansion:

$$\frac{1}{(B\rho)} [B_x(x, y) + i B_y(x, y)] \equiv \sum_n (b_n + i a_n) (x + i y)^{n-1} = \sum_n (b_n + i a_n) e^{i(n-1)\phi} \quad (3.1-13)$$

where $n=1,2,3,\dots$ are the dipole, quadrupole, sextupole, ... components, respectively.

In particular, the multipole errors, $\Delta B_n^{(N)}$, relative to the desired field component, b_N , are normalized at a reference radius R and defined by¹⁵

$$\Delta B_n^{(N)}(R) \equiv R^{n-N} \frac{\Delta b_n}{b_N} \quad \text{or} \quad \Delta A_n^{(N)}(R) \equiv R^{n-N} \frac{\Delta a_n}{b_N} \quad (3.1-14)$$

¹⁵ Using the peak B-field for insertion devices.

where $(\Delta b_n, \Delta a_n)$ are the multipole field errors.

The tolerances for the multipole errors are given in Table 3.1.9 using values achieved at the SLS facility [3.1.25, 3.1.26]. The impact is an additional ~20% DA reduction for the lattice with the previously defined alignment tolerances. Future work will include parametric studies for a more precise specification.

Table 3.1.9 Tolerance Levels for RMS Normalized Multipole Errors.

Magnet Type	Normalized Field Error ($R = 28$ mm)						
Quadrupoles	$\Delta B_2^{(2)}$	$\Delta B_3^{(2)}$	$\Delta A_3^{(2)}$	$\Delta B_4^{(2)}$	$\Delta A_4^{(2)}$	$\Delta B_6^{(2)}$	$\Delta B_{10}^{(2)}$
	2.5×10^{-4}	2.8×10^{-4}	2.9×10^{-4}	1.9×10^{-4}	1.4×10^{-4}	1.3×10^{-4}	0.3×10^{-4}
Sextupoles	$\Delta B_3^{(3)}$	$\Delta B_4^{(3)}$	$\Delta A_4^{(3)}$	$\Delta B_5^{(3)}$	$\Delta B_9^{(3)}$	$\Delta B_{15}^{(3)}$	
	5.0×10^{-4}	5.2×10^{-4}	4.9×10^{-4}	3.5×10^{-4}	0.8×10^{-4}	0.5×10^{-4}	

Similarly challenging is the impact of the linear optics distortions from the insertion devices listed in Table 3.1.10. In particular, the proposed superconducting undulators will substantially affect the nonlinear dynamics in the vertical plane due to their short period (see Section 3.1.2.8). The effect of elliptically polarized undulators on the DA remains to be studied. Table 3.1.11 lists the allowed multipole field tolerances for these undulators [3.1.27]. The potential configuration includes the following IDs:

- CPMUs in the 6 m straights
- CPMUs in the 9 m straights
- DWs in the 9 m straights
- EPUs in the 6 m straights¹⁶

Details on the impact of these insertion devices and the control of their nonlinear terms are presented in Section 3.1.2.8.

Table 3.1.10 Insertion Device Parameters and Their Impact on the Vertical Tune.

ID	λ_u [mm]	B [T]	K_u	L_u [m]	Gap [mm]	Δv_y
SCU (2+1)	14	1.7	2.2	2	-5	0.002
CPMU (3)	19	1.24	2.2	3	5	0.002
DW	100	1.8	16.8	7	-11	0.028
EPU	~40	0.88	(3.3, 3.3)	~4	~6.5	TBD

¹⁶ Presumably as 2×1 m canted devices.

Table 3.1.11 RMS Normalized Field Errors for Insertion Devices (CPMU, $R = 20$ mm).

Multipole	$\Delta B_3^{(1)}$	$\Delta A_3^{(1)}$	$\Delta B_4^{(1)}$	$\Delta A_4^{(1)}$
Random	6.6×10^{-7}	6.6×10^{-7}	2.2×10^{-8}	2.2×10^{-8}

Note: Based on tolerances from the Swiss Light Source.

3.1.2.5 Control of Closed-Orbit Distortions (“Golden Orbit” philosophy)

While essentially a linear problem, effective orbit control is crucial for robust DA¹⁷ and orbit stability. From a DA point of view, the main objective for the global orbit correction system is to establish and maintain an orbit at the magnetic centers of the sextupoles (to avoid breaking the symmetry of the linear optics), to within $\sim 50 \mu\text{m}$ (Table 3.1.7). As a rough guideline, the BPMs should be spaced by $\sim 90^\circ$ in phase advance and placed close to the sextupoles. With a horizontal DBA cell tune of ~ 1.1 , about six BPMs per cell should provide good coverage. In order to center the orbit in all the BPMs, one corrector for each BPM is needed. In theory, the DA can be restored if the BPM is at the sextupole magnetic center [3.1.6]. The number of correctors can be reduced in the vertical plane, since the cell tune is only ~ 0.5 . From the horizontal phase advance (Figure 3.1.23), it is clear that at least one BPM is required in each of the dispersive and straight sections.

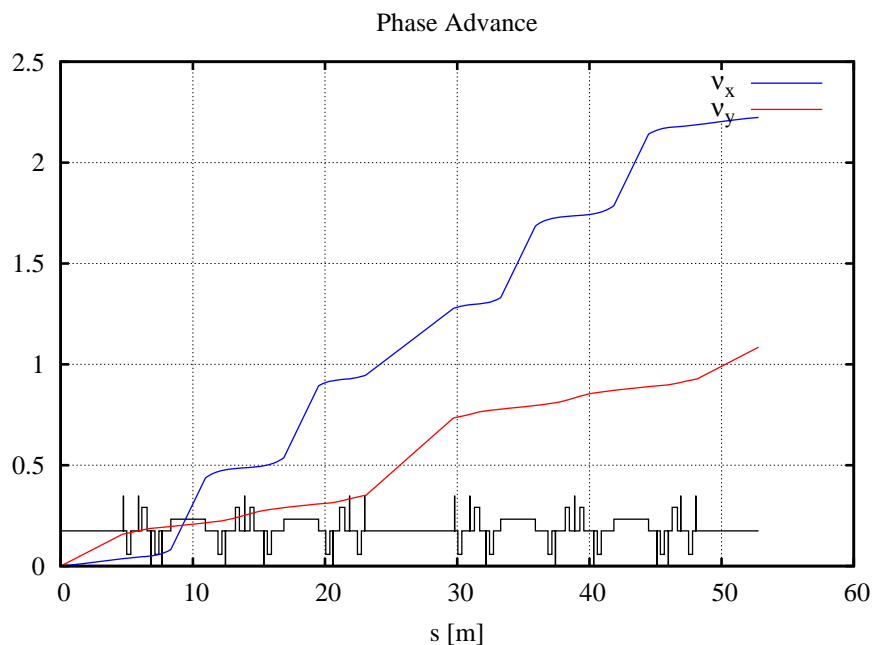


Figure 3.1.23 Normalized Phase Advance for one super-period.

Figures 3.1.24 a and b show the corrected horizontal and vertical RMS closed-orbit distortions (for 1,000 seeds) due to $100 \mu\text{m}$ RMS random horizontal and vertical quadrupole misalignment errors, with the (H-BPM \times H-Corrector, V-BPM \times V-Corrector) = (6 \times 6, 6 \times 6) baseline configuration. Clearly, the resulting orbit is well within the guidelines of Table 3.1.7. BPM buttons are included at the center of each DBA for optics checks during commissioning. Beam-based alignment [3.1.29, 3.1.30] with BPMs at the end of the girders

¹⁷ To avoid the collapse of DA observed in the ALS CDR [3.1.26], eventually addressed by “Global Matching of the Normalized Ring” [7.1.10–7.1.15].

will make it possible to reduce orbit errors below the survey and alignment tolerances for the girders, particularly since the alignment tolerances for the magnetic centers on the girders are tighter than the girder alignment in the tunnel.

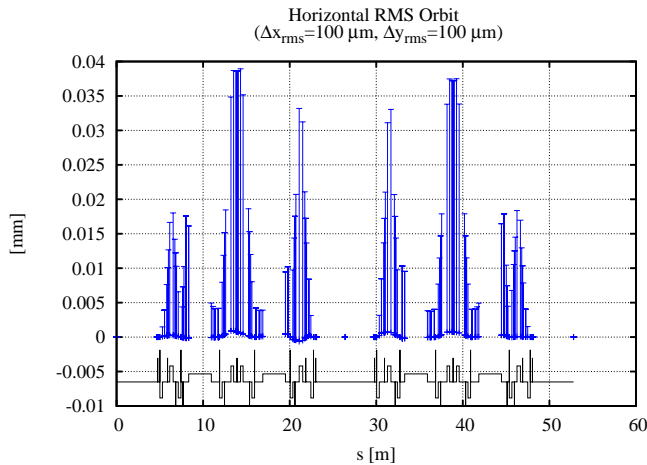


Figure 3.1.24 a Corrected horizontal RMS COD (over 1,000 seeds) for one super-period.

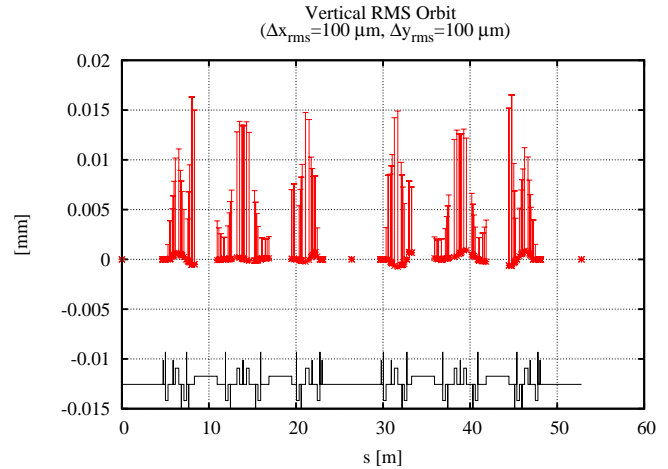


Figure 3.1.24 b Corrected vertical RMS COD (over 1,000 seeds) for one super-period.

Although placing the BPMs close to the sextupoles reduces the residual COD at the sextupoles, the BBA resolution is better for quadrupole centering ($<10 \mu\text{m}$ both H and V) by at least a factor of three [3.1.27, 3.1.28]. This allows for orbit centering beyond the magnet alignment tolerance on the girder. Therefore, we have adopted the $(6 \times 6, 6 \times 6)$ correction scheme, with the BPMs close to the quadrupoles for BBA with a resolution of $10 \mu\text{m}$. The impact on the DA of the corrected COD resulting from the alignment tolerances¹⁸ listed in Table 3.1.8 is shown in Figure 3.1.25 (for 20 random seeds). Clearly the $(6 \times 6, 6 \times 6)$ orbit correction system provides adequate DA, and provides margin for error.

¹⁸ Except for roll errors, to be treated later.

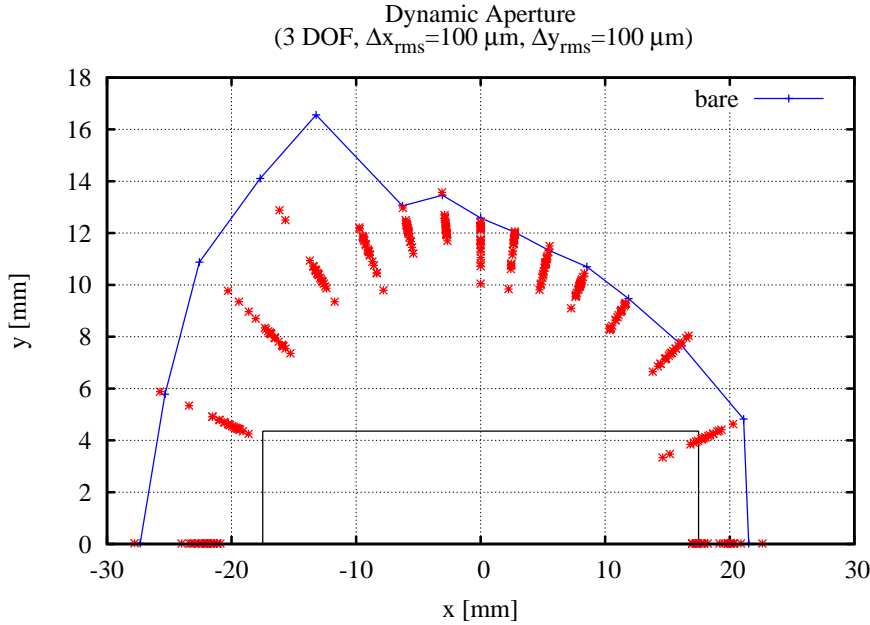


Figure 3.1.25 DA for lattice with transverse misalignment errors (20 seeds), according to Table 3.1.8. These CODs are corrected with the baseline (6×6, 6×6) system.

3.1.2.6 Control of Vertical Beamsize

The vertical beamsize is given by

$$\sigma_y = \sqrt{\beta_y \varepsilon_y + (\eta_y \sigma_\delta)^2} \quad (3.1-15)$$

where β_y and η_y are the vertical beta function and dispersion, ε_y is the vertical emittance, and σ_δ is the momentum spread. The design goal is $\varepsilon_y \sim 0.01$ nm-rad, corresponding to $\sigma_y \sim 5 \mu\text{m}$ in the short straights.

The non-vanishing vertical emittance originates from:

- linear coupling of the horizontal emittance due to roll errors of the quadrupoles and vertical orbit displacement in the sextupoles,
- and vertical dispersion due to roll errors of the dipoles and linear coupling of the horizontal dispersion.

Local control of the vertical beamsize is straightforward. In particular, by controlling the off-diagonal beam response matrix elements given by [3.1.29]:

$$\frac{\partial y_k}{\partial p_{x,i}} = -\frac{(\Delta a_2 L)_j \sqrt{\beta_{x,i} \beta_{x,j} \beta_{x,k}} \cos(\mu_{x,i \rightarrow j} - \pi \nu_x) \cos(\mu_{y,j \rightarrow k} - \pi \nu_y)}{4 \sin(\pi \nu_x) \sin(\pi \nu_y)} + O(\Delta a_2 L)^2, \quad (3.1-16)$$

$$\frac{\partial x_k}{\partial p_{y,i}} = -\frac{(\Delta a_2 L)_j \sqrt{\beta_{y,i} \beta_{y,j} \beta_{y,k}} \cos(\mu_{y,i \rightarrow j} - \pi \nu_y) \cos(\mu_{x,j \rightarrow k} - \pi \nu_x)}{4 \sin(\pi \nu_x) \sin(\pi \nu_y)} + O(\Delta a_2 L)^2$$

for a dipole kick, $p_{(x,y),i}$ at i , due to a skew quadrupole ($a_2 L$) at j produces an orbit change ($\Delta x_k, \Delta y_k$) at a BPM located at k . Similarly, the local control of the vertical dispersion is done by:

$$\Delta\eta_{y,k} = -\frac{(\Delta a_2 L)_j \eta_{x,j} \sqrt{\beta_{y,j} \beta_{x,k}} \cos(\mu_{x,j \rightarrow k} - \pi \nu_x)}{2 \sin(\pi \nu_y)} + O(\Delta a_2 L)^2. \quad (3.1-17)$$

The driving term for the linear coupling is shown in Figure 3.1.26, whereas the driving term for vertical dispersion is similar to the one for vertical linear chromaticity, (Figure 3.1.7). Adequate control is obtained by introducing one skew quadrupole:

- in each long matching section
- in one of the dispersion cells for each super-period

for a total of $15 + 15 = 30$ skew quadrupoles for the full lattice. The corresponding (linear) system of equations

$$\left[\frac{\partial \bar{x}}{\partial \bar{p}_y}, \frac{\partial \bar{y}}{\partial \bar{p}_x}, \Delta \bar{\eta}_y \right]^T = S \cdot (\Delta a_2 L) \quad (3.1-18)$$

was solved in a least-square sense by the Singular Value Decomposition method. The vertical dispersion after correction for the coupling introduced by the roll errors in Table 3.1.8, is shown in Figure 3.1.27. It turns out that the vertical emittance can be corrected significantly below $\varepsilon_y \sim 0.01$ nm-rad. To optimize the Touschek lifetime, a vertical dispersion wave¹⁹ is introduced to obtain the desired vertical beamsizes, e.g., $\eta_y = 5$ mm $\Rightarrow \sigma_y \sim \eta_y \sigma_\delta = 5$ μ m (Figure 3.1.28). Similarly, the vertical beam size and the transverse coupling angle is shown in Figures 3.1.29 and 3.1.30, respectively. Since it is straightforward to measure the beam response matrix and vertical dispersion on the real storage ring, the correction algorithm implemented for this simulation will eventually be used for commissioning as well.

¹⁹ To avoid affecting the dynamics 0.

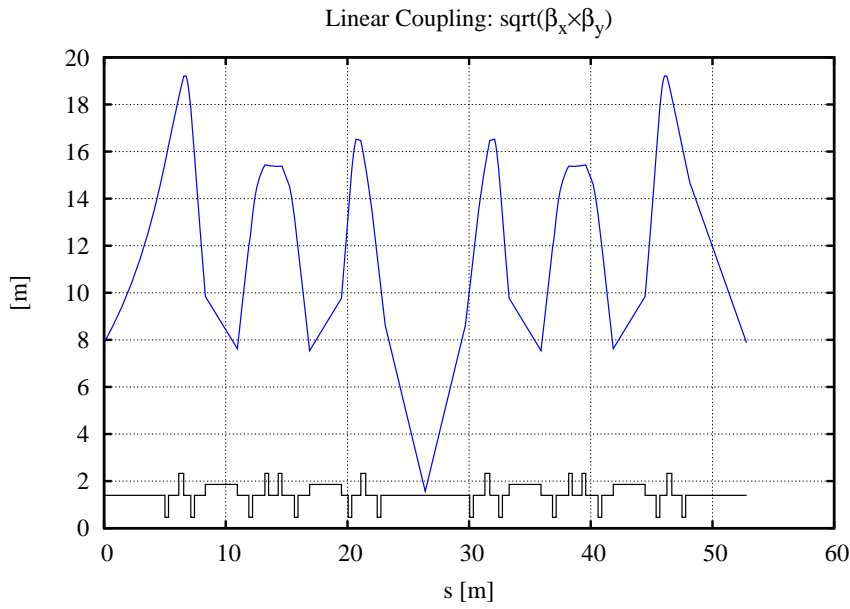


Figure 3.1.26 Driving term for linear coupling, for one super-period.

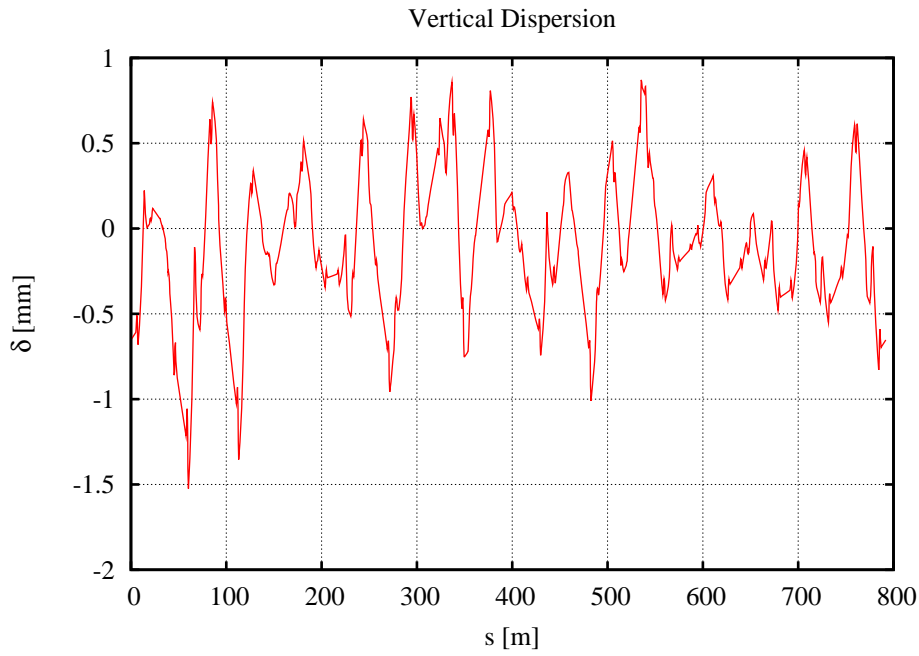


Figure 3.1.27 Corrected vertical dispersion for the quadrupole and dipole roll tolerances.

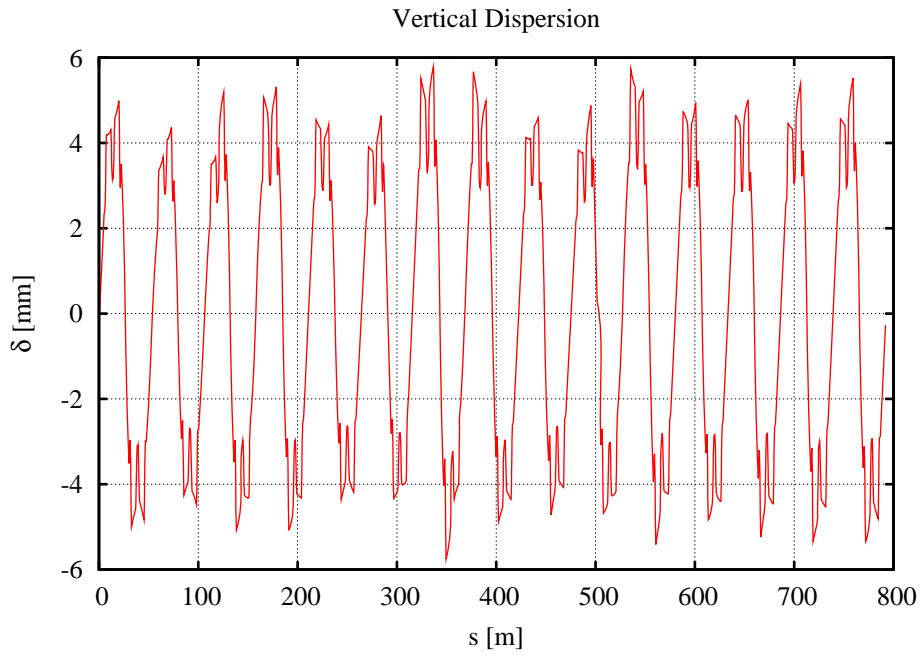


Figure 3.1.28 Corrected vertical dispersion with a residual 5 mm dispersion wave for vertical beamsize control.

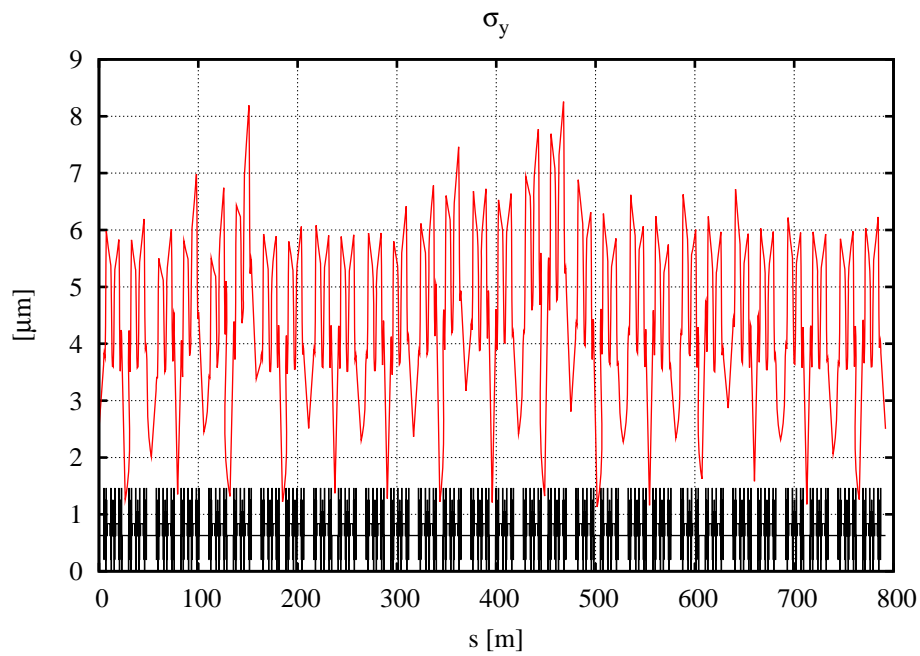


Figure 3.1.29 Vertical beam size with a residual 5 mm dispersion wave.

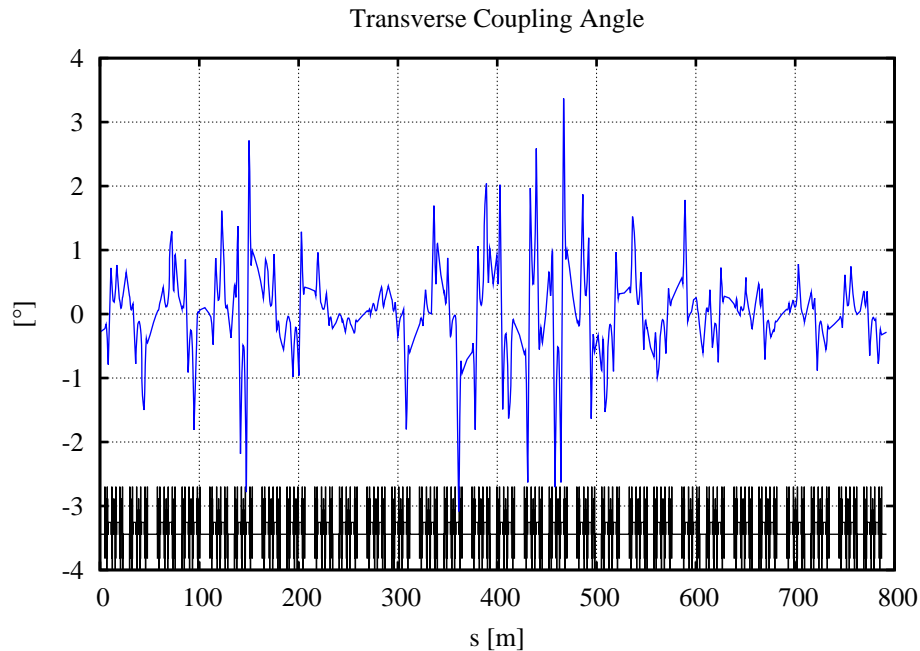


Figure 3.1.30 Transverse coupling angle around the ring with a residual 5 mm dispersion wave.

3.1.2.7 Robustness of DA

The introduction of alignment errors in the lattice leads to orbit distortions, which generate magnetic field errors due to feed-down in the multipoles. These errors are summarized in Table 3.1.12. A robust DA requires that the global orbit correction system maintains the orbit centered in the sextupoles, since feed-down leads to gradient errors. To correctly evaluate this impact, correlations between magnet-magnet alignment errors, e.g., from girder misalignments, need to be included. Also, real magnets are not pure dipoles, quadrupoles, or sextupoles, requiring systematic and random multipole errors to be included. A detailed study of the individual maximum tolerance levels of these multipole errors remains to be done, but the realistic values listed in Table 3.1.9 have been used to evaluate the impact on the DA.

Table 3.1.12 Effect of Mechanical Tolerances on the Magnetic Field Quality.

	Dipole	Quadrupole	Sextupole
Horizontal orbit		horizontal dipole error	gradient error
Vertical orbit		vertical dipole error	skew quadrupole error
Roll error	vertical dipole error	skew quadrupole error	skew sextupole error

Also, due to the nonlinear chromaticity, tracking for at least one synchrotron oscillation period is required to obtain realistic estimates of the DA, since the off-momentum particle will be slowly crossing betatron resonances, which may limit the stability to smaller amplitudes. The design goal for the RF acceptance is $\pm 3\%$. To obtain a conservative estimate of the momentum aperture, an RF voltage sufficient to produce a 4% bucket height was used to evaluate the DA. The impact on the DA and momentum aperture is shown in Figures 3.1.31 – 3.1.33, where the black-outlined rectangle (Figure 3.1.31) represents the physical aperture of the lattice, propagated to the center of the long straight section. The 20 seeds shown represent 20 lattices generated with randomly distributed alignment and multipole errors having RMS values given by the tolerance values and corrected for COD, as described above. The tracked particles undergo synchrotron oscillations, but do not radiate. Since the radiation damping will also lead to the crossing of resonances, it should also be included in refined studies.

Low-emittance lattices tend to have a small linear momentum compaction, α_1 , requiring the second-order term, α_2 , to be included for a proper evaluation of the RF bucket, which becomes distorted and reduces the momentum acceptance [3.1.31]. The source of this distortion is a second stable fixed point, which has an energy offset given by the ratio:

$$\alpha_1/\alpha_2 \approx 3.7 \times 10^{-4} / 4.1 \times 10^{-4} = 92\%. \quad (3.1-19)$$

Since it only becomes important for ratios $<20\%$, it will not pose a problem for this lattice²⁰. This is further demonstrated by the phase space for the longitudinal Hamiltonian (shown in Figure 3.1.34), including terms to α_3 , as well as the radiation loss of 35 m of damping wigglers.

To summarize, the DA guidelines from Table 3.1.5 are easily met for the bare lattice, as well as when the impact of realistic alignment and field tolerances, listed in Tables 3.1.8 and 3.1.9, are included in the lattice model using the correction schemes described above.

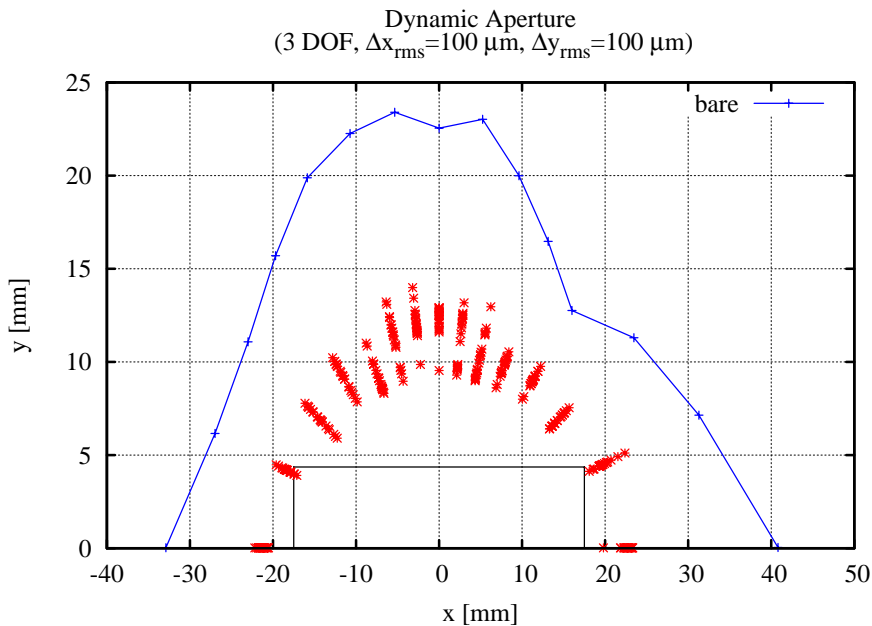


Figure 3.1.31 DA²¹ for a “realistic” lattice (20 seeds) with engineering tolerances and corrections. The black outline indicates the physical aperture.

²⁰ An advantage of the achromatic straights for the DBA lattice.

²¹ The relatively large drop to $x, y \approx [22, 12]$ mm is due to the crossing of $\nu_x = 33, 4\nu_y = 63$ at these amplitudes, see Figures 6.1.6 and 6.1.7.

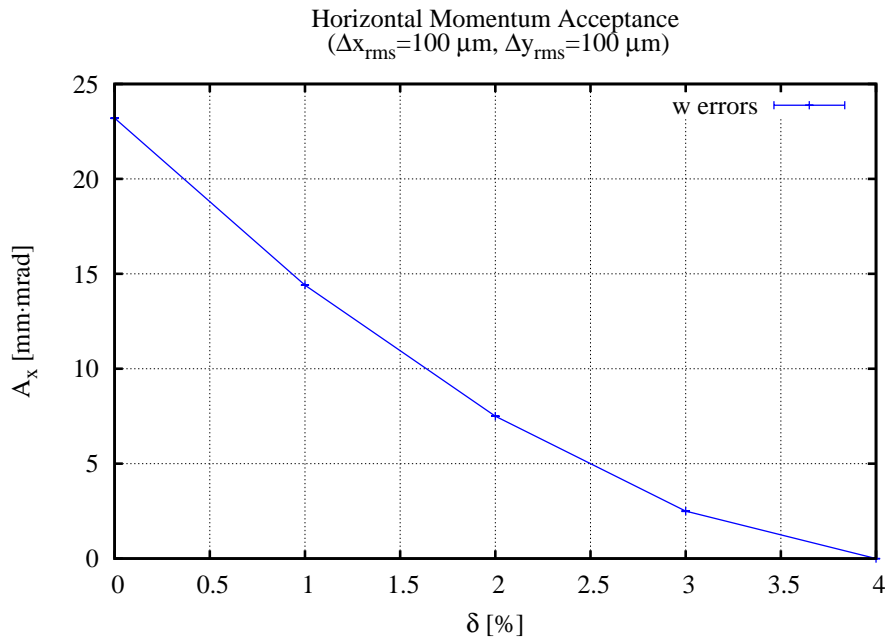


Figure 3.1.32 Average and RMS horizontal momentum acceptance for a “realistic” lattice (20 seeds) with engineering tolerances and corrections.

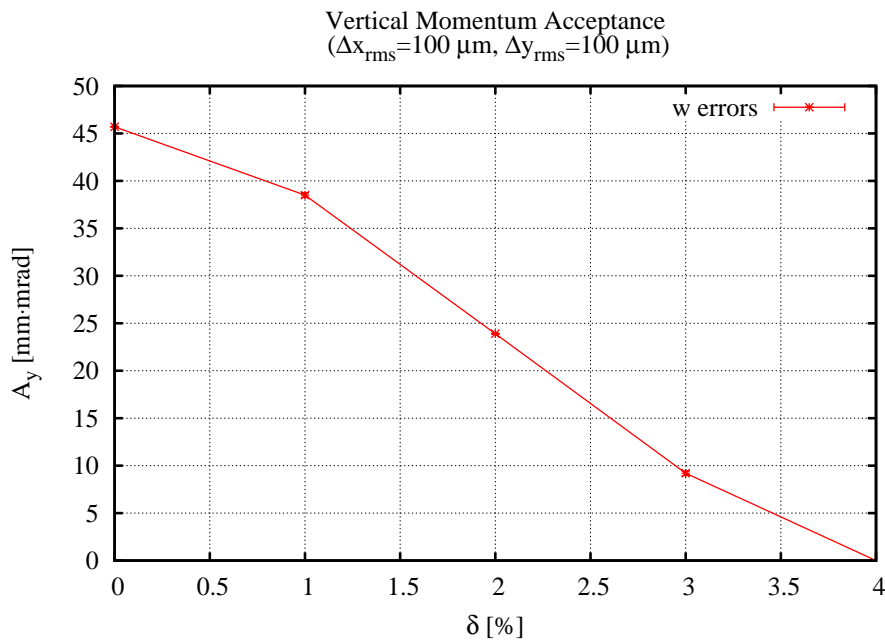


Figure 3.1.33 Average and RMS vertical momentum acceptance for a “realistic” lattice (20 seeds) with engineering tolerances and corrections.

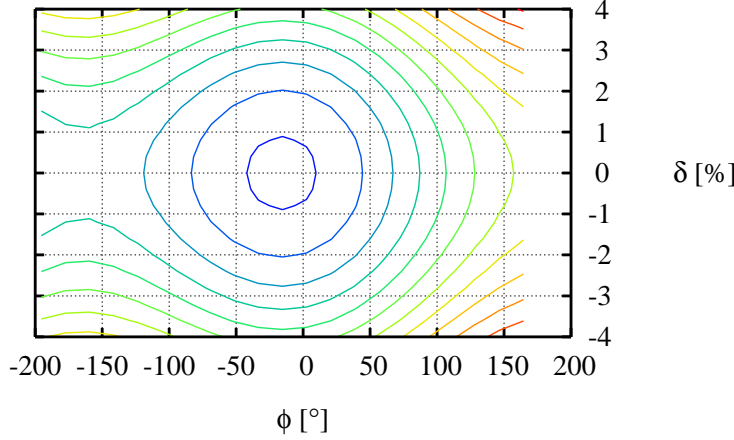
Longitudinal Phase Space to $O(\alpha_4)$ 

Figure 3.1.34 Longitudinal phase-space, including the radiation loss from damping wigglers.

3.1.2.8 Control of Impact from Insertion Devices

The Hamiltonian for an ID averaged over one undulator period, λ_u , is given by [3.1.36, 3.1.37]:

$$\langle H \rangle_{\lambda_u} \approx \frac{p_x^2 + p_y^2}{2(1 + \delta)} - \frac{B_u^2 y^2}{4(B\rho)^2(1 + \delta)} + \frac{\pi^2 B_u^2 y^4}{3(B\rho)^2 \lambda_u^2 (1 + \delta)} - \delta + O(p_{x,y}^4) \quad (3.1-20)$$

with phase-space coordinates $\bar{x} = [x, p_x, y, p_y, \delta, c\Delta t]$, peak field B_u , and magnetic rigidity $(B\rho)^{22}$. Note that both the leading-order linear and nonlinear effect scales with $1/(B\rho)^2$, i.e., the effect is reduced with the energy squared for a given undulator field, B_u . The term quadratic in y introduces a vertically focusing term with the integrated gradient

$$(b_2 L) \approx -\frac{B_u^2 L_u}{2(B\rho)^2} \quad (3.1-21)$$

i.e., quadratic in B_u . The beta-beat at location i due to integrated quadrupole kicks, $(\Delta b_2 L)_j$, is given by:

$$\frac{\Delta \beta_{(x,y),i}}{\beta_{(x,y),i}} = \sum_{j=1}^N \frac{(\Delta b_2 L)_j \beta_{(x,y),j} \cos\left(2\mu_{(x,y),i \rightarrow j} - 2\pi\nu_{(x,y)}\right)}{2 \sin(2\pi\nu_{(x,y)})} + O(\Delta b_2 L)^2 \quad (3.1-22)$$

where β, μ, ν are the beta functions, phase advance, and tune. Similarly, the phase-beat is given by:

²² $(B\rho) \approx 10.007$ T-m at 3 GeV.

$$\Delta\mu_{(x,y),i} = -\sum_{j=1}^N \frac{\text{sgn}(\mu_{(x,y),i \rightarrow j}) (\Delta b_2 L)_j \beta_{(x,y),j} \left(\sin(2\pi\nu_{(x,y)}) + \sin\left(2\mu_{(x,y),i \rightarrow j} - 2\pi\nu_{(x,y)}\right) \right)}{4\sin(2\pi\nu_{(x,y)})} + O(\Delta b_2 L)^2, \quad (3.1-23)$$

and the total tune shift is given by

$$\Delta\nu_{(x,y)} = \pm \frac{1}{4\pi} \sum_{j=1}^N (\Delta b_2 L)_j \beta_{(x,y),j} + O(\Delta b_2 L)^2. \quad (3.1-24)$$

The parameters for the proposed insertion devices are summarized in Table 3.1.10, and the impact of three DWs on the linear optics is shown in Figure 3.1.35, where the beta-beat is rather obvious.

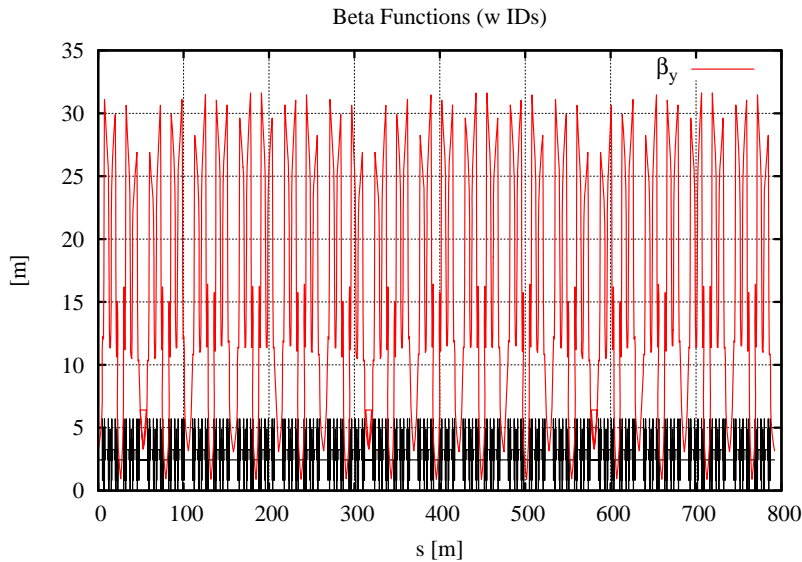


Figure 3.1.35 Perturbed beta functions of the lattice with three DWs installed.

The perturbation of the optics is corrected by adjusting the quadrupole quadruplets in the matching sections. With four quadrupole strengths as parameters, it is expected²³ that the beta- and phase advance beat can be removed in both planes. In particular, the optics deviations at all of the lattice sextupoles, i , are represented in a linearized system of equations that includes the focusing impact of all installed IDs $(\Delta b_2 L)_j$. These equations are given in matrix form by

$$\left[\begin{array}{c} \left(\frac{\Delta\beta_{(x,y)}}{\beta_{(x,y)}} \right)_i \\ \Delta\mu_{(x,y),i} \\ \Delta\nu_{x,y} \end{array} \right]^T = A \cdot [\Delta\bar{b}_2 L] \quad (3.1-22)$$

which was solved using an iterated SVD algorithm[3.1.34, 3.1.35], see Figure 3.1.36. The corrected beta and phase advance beats satisfy the optics tolerances specified in Table 3.1.7.

²³ If the parameters are independent.

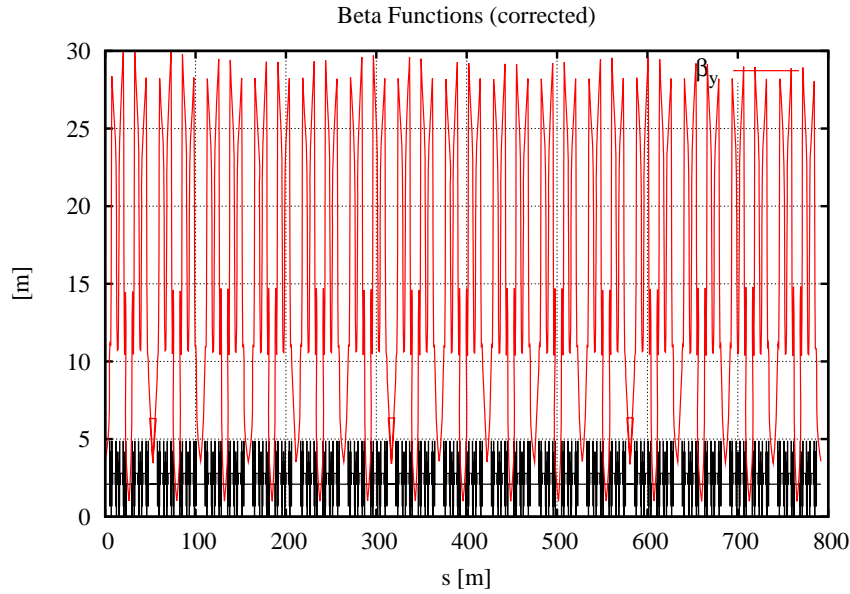


Figure 3.1.36 Corrected beta functions for the lattice with three DWs installed.

The leading order nonlinear part of the ID focusing contains an octupole-like term in the vertical plane which drives amplitude dependent vertical tune shift and $2\nu_y$ and $4\nu_y$ resonances. Table 3.1.13 presents a comparison of the magnitude of the main driving terms from the IDs with those from sextupoles in the lattice. The choice of the length for the CPMUs have been validated by tracking, see Figure 3.1.37.

Table 3.1.13 Lie Generators from the Sextupole Scheme and a Single ID.

Lie Generator	Effect	Sextupole Scheme	DW (Long Straight)	CPMU (Short Straight)	CPMU (Long Straight)	SCU (Short Straight)	SCW (Short Straight)
$ h_{00220} $	$\partial \nu_y / \partial J_y$	363	609	570	1,982	641	492
$ h_{00310} $	$2\nu_y$	22	72	22	976	163	251
$ h_{00400} $	$4\nu_y$	1	18	57	79	43	16

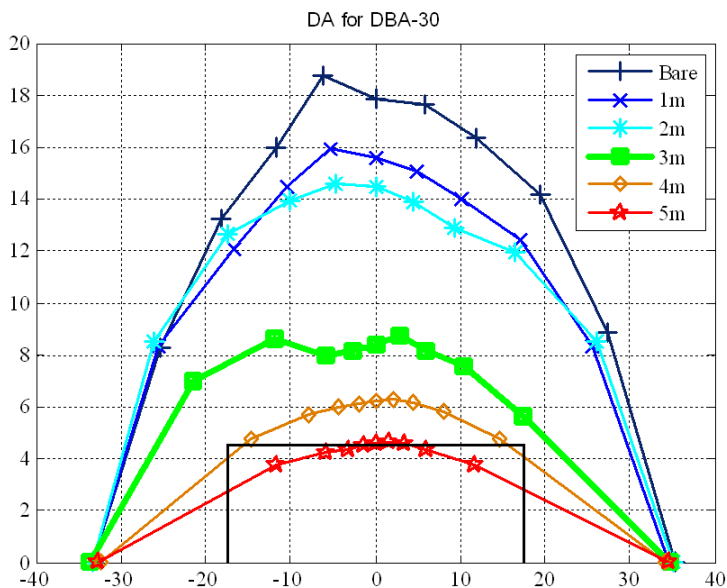


Figure 3.1.37 Impact of the length of one CPMU on the DA.

The effects on the DA and momentum aperture of a lattice with errors and 3 DWs are shown in Figures 3.1.38 and 3.1.39, respectively. The DA is reduced in the vertical to the limited physical aperture. However, there is now considerable diffusion in the interior, which will require further study. Similarly, Figures 3.1.40 and 3.1.41 show the impact of three DWs and 15 CPMUs. Again, the DA is reduced in the vertical due to the reduced vertical aperture. Also, the impact of one APPLE-II EPU is shown in Figures 3.1.42 and 3.1.43. It is well known that the latter are strongly nonlinear devices, and while the dynamic aperture is maintained, control of the impact of these devices may require further work. However, we have now established a realistic (numeric approach) ID model, based on RADIA kick maps [3.1.40], from which it is straightforward to extract the driving terms (analytic approach). Moreover, pioneering work to control the dynamic terms with L-shims has been developed at the ESRF [3.1.41] and BESSY-2 [3.1.42]; guided by fitted generating function techniques.

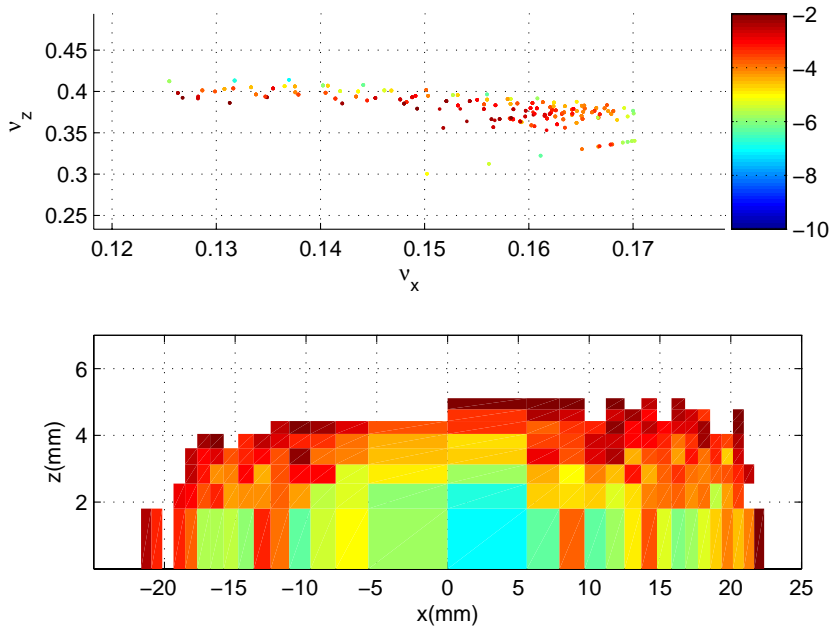


Figure 3.1.38 Frequency map vs. transverse amplitudes for a lattice with three DWs and engineering tolerances.

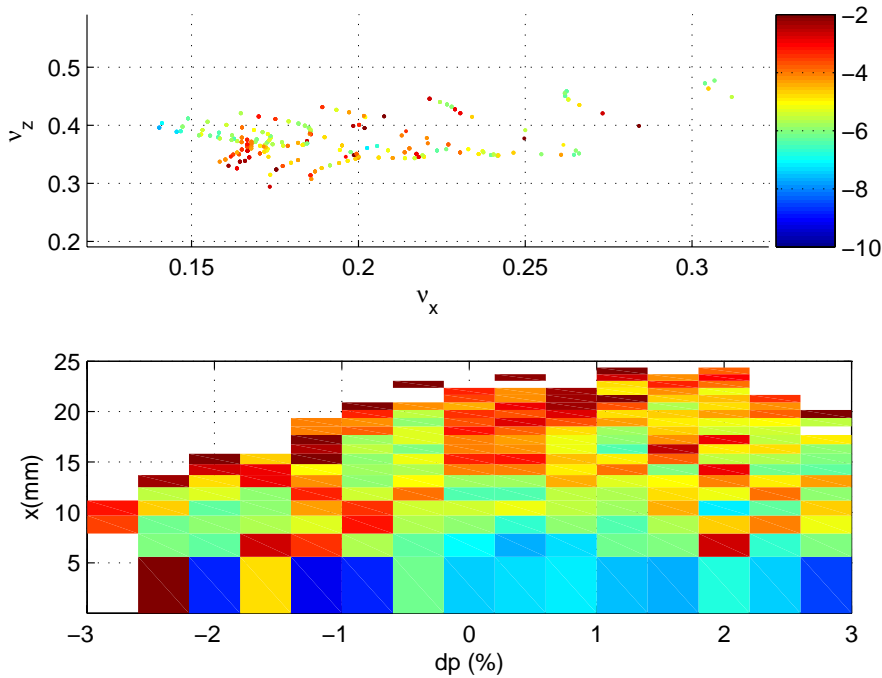


Figure 3.1.39 Frequency map vs. momentum and horizontal amplitude for a lattice with three DWs, 15 CPMUs, and engineering tolerances.

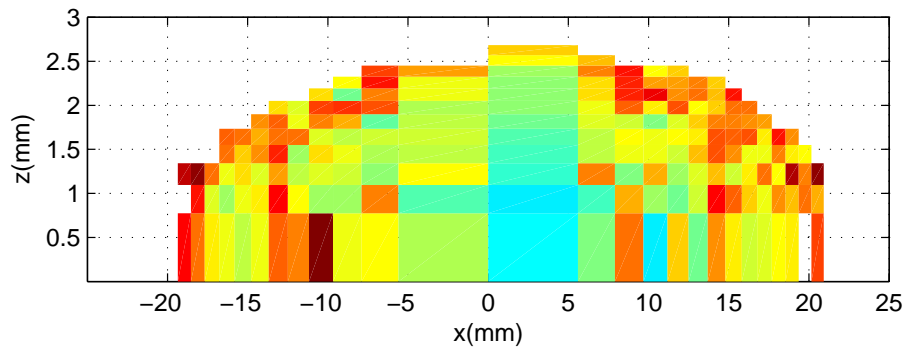
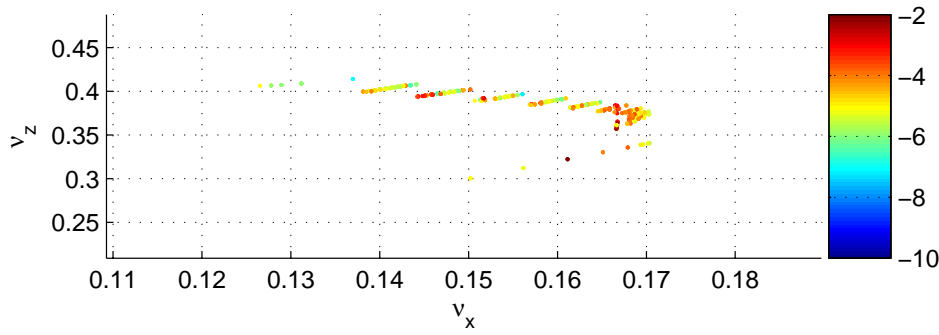


Figure 3.1.40
Frequency map vs. momentum and horizontal amplitude for a lattice with three DWs, 15 CPMUs, and engineering tolerances.

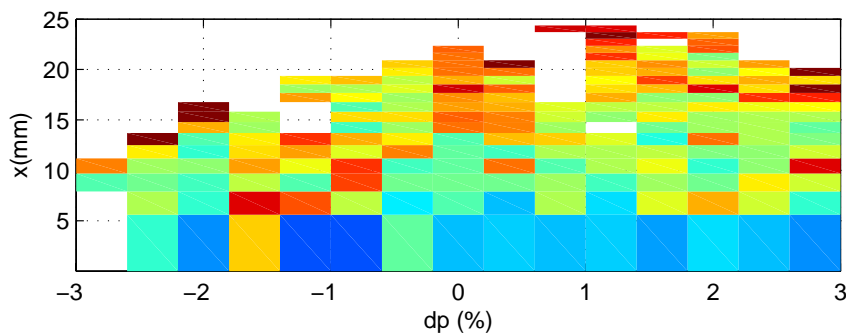
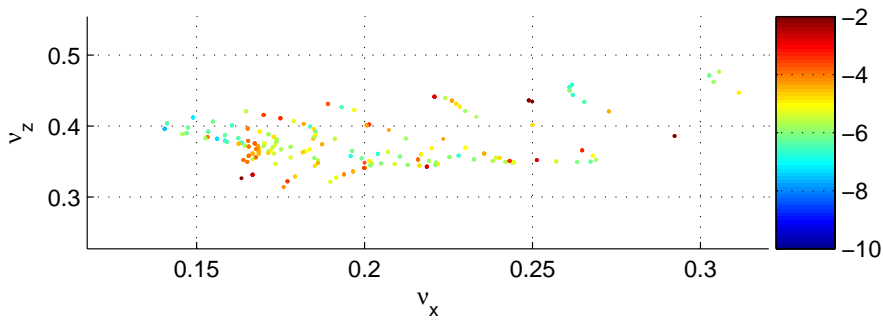


Figure 3.1.41
Frequency map vs. momentum and horizontal amplitude for a lattice with three DWs, 15 CPMUs, and engineering tolerances.

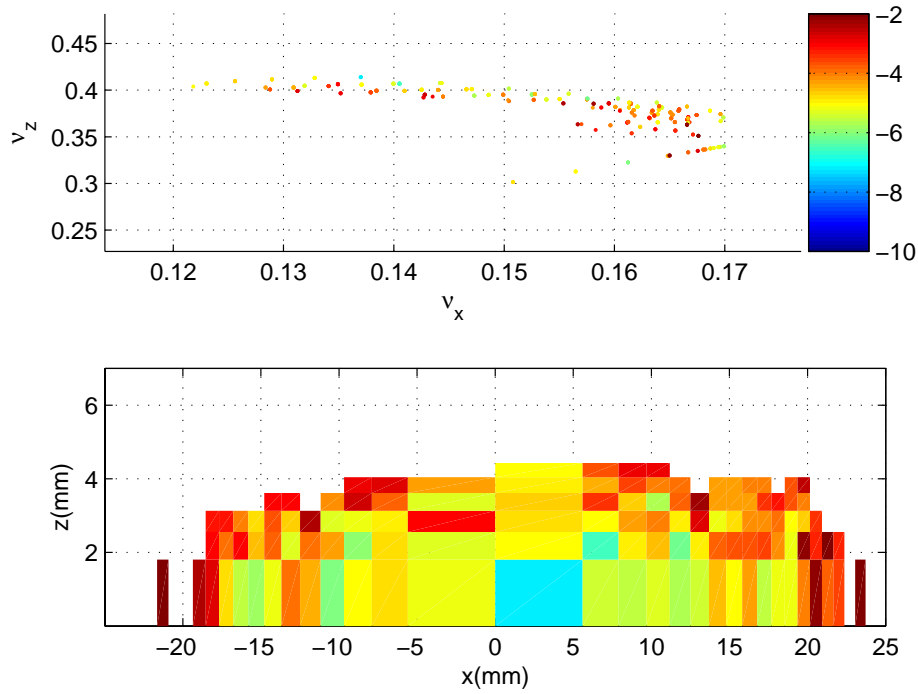


Figure 3.1.42
 Frequency map vs. transverse amplitudes for a lattice w 1 EPU of APPLE-II type and engineering tolerances.

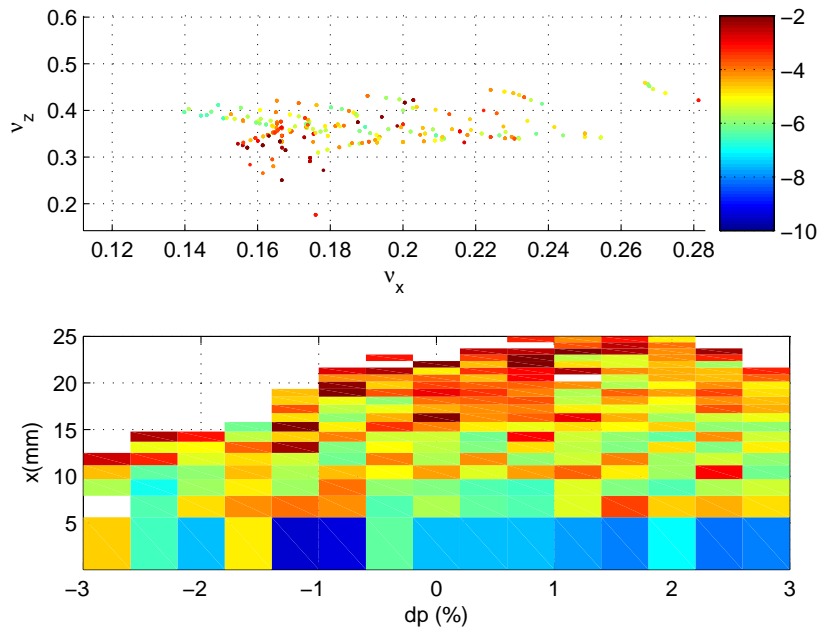


Figure 3.1.43
 Frequency map vs. momentum and horizontal amplitude for a lattice w 1 EPU of APPLE-II type and engineering tolerances.

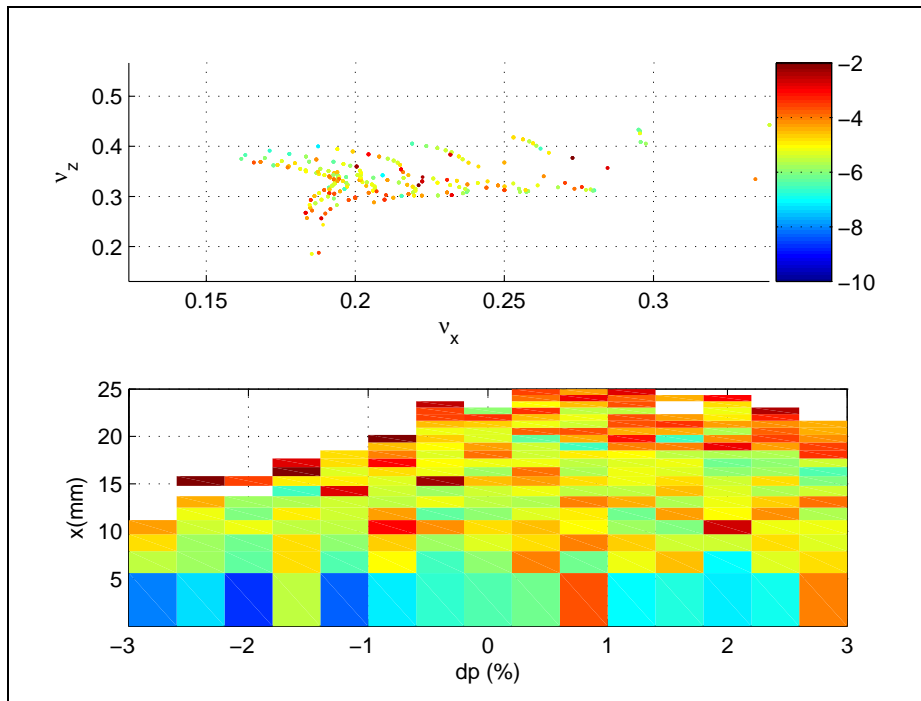


Figure 3.1.43 Frequency map vs. momentum and horizontal amplitude for a lattice w 1 EPU of APPLE-II type and engineering tolerances.

3.1.2.9 Future Work in Lattice and Beam Dynamics Issues

The work presented here shows that the lattice is robust for the errors and realistic magnets. Moreover, that the main impact from the damping wigglers is the perturbation of the optics, which can be restored, and that the dynamic aperture remains outside the physical when 3 DWs and 15 CPMUs are included. However, fine tuning of the working point is required to reduce the considerable amount of tune shift, i.e., resonances, that are observed in the interior of the DA for a realistic lattice. And, to validate the performance with a full set of IDs.

References

- [3.1.1] H. Weidemann, NIM **A266**, p. 24 (1988).
- [3.1.2] S. Krinsky, et al., EPAC06, p.3487 (2006).
- [3.1.3] G. Decker, and O. Singh, *Phys. Rev. STAB* **2**, p. 112801 (1999).
- [3.1.4] S. Krinsky, J. Bengtsson, and S. Kramer, "Consideration of a Double Bend Achromatic Lattice for NSLS-II," pp. 3487–3489, EPAC06.
- [3.1.5] J. Bengtsson, "A Control Theory Approach for Dynamic Aperture," pp. 3478–3480, EPAC06.
- [3.1.6] J. Bengtsson, W. Joho, P. Marchand, G. Mülhaupt, L. Rivkin, and A. Streun, "Increasing the Energy Acceptance of High Brightness Synchrotron Light Storage Rings," *Nucl. Instr. Meth. A* **404**, 237–247 (1998).
- [3.1.7] A. Wrulich, et al., "Commissioning of the Swiss Light Source," pp. 224–226, PAC01.
- [3.1.8] A. Wrulich, et al., "Achievements of the SLS Commissioning," PSI. Scientific Report 2001 Vol. VII, 2002.
- [3.1.9] M. Böge, "Achieving Sub-Micron Stability in Light Sources," pp. 211–213, EPAC04.
- [3.1.10] J. Bengtsson, and E. Forest, "Global Matching of the Normalized Ring" Workshop on Effects of Errors in Accelerators, their Diagnosis and Corrections," Corpus Christi, TX, Oct. 3–8, 1991.
- [3.1.11] J. Bengtsson, and M. Meddahi, "Modeling of Beam Dynamics and Comparison with Measurements for the Advanced Light Source (ALS)," pp. 1022–1024, EPAC94.

- [3.1.12] D. Robin, G. Portmann, H. Nishimura, and J. Safranek, "Model Calibration and Symmetry Restoration of the Advanced Light Source," pp. 971–973, EPAC96.
- [3.1.13] J. Safranek, "Experimental Determination of Storage Ring Optics Using Orbit Response Measurements," *Nucl. Instr. and Meth. A* **388**, 27-36 (1997).
- [3.1.14] D. Robin, C. Steier, J. Safranek, and W. Decking, "Enhanced Performance of the Advanced Light Source through Periodicity Restoration of the Linear Lattice," pp. 136–138, EPAC00.
- [3.1.15] J. Laskar, L. Nadolski, D. Robin, and C. Steier, "Global Dynamics of the Advanced Light Source Revealed through Experimental Frequency Map Analysis," *Phys. Rev. Lett.* **85**, 558–561 (2000).
- [3.1.16] J. Bengtsson, "X-Ray Ring Optics: the Inverse Problem," NSLS Tech Note 540 (2005).
- [3.1.17] J. Bengtsson, "The Sextupole Scheme for the Swiss Light Source (SLS): An Analytic Approach," SLS Note 9/97 (1997).
- [3.1.18] A. Streun, J. Bengtsson, beam studies collaboration at the SLS, May 14-25, 2007.
- [3.1.19] Y. Luo, M. Bai, R. Calaga, J. Bengtsson, W. Fischer, N. Malitsky, F. Pilat, T. Satogata "Measurement and Correction of Third Resonance Driving Term in the RHIC.
- [3.1.20] Diamond Synchrotron Light Source: Report of the Design Specification," CCLRC (2002).
- [3.1.21] S.L. Kramer, S. Krinsky, and J. Bengtsson, "Comparison of Double Bend and Triple Bend Achromatic Lattice Structures for NSLS-II" pp. 384–386, EPAC06.
- [3.1.22] E. Forest "A Hamiltonian-Free Description of Single Particle Dynamics for Hopelessly Complex Systems" *J. Math. Phys.* **31**, pp. 1133-1144 (1990).
- [3.1.23] J. Bengtsson "The Poincaré Map, Lie Generator, Nonlinear Invariant, Parameter Dependence, and Dynamic Aperture for Rings" pp. 4315-4317, PAC07
- [3.1.24] J. Bengtsson, "On the NSLS-II Dynamic Aperture: Robustness," NSLS-II Tech Note 8 (2005).
- [3.1.25] A. Streun, "SLS Dynamic Acceptance Degradation due to Magnet Multipole Errors," SLS-TME-TA-1998-0002 (1998).
- [3.1.26] E.I. Antokhin, et al., "Multipoles of the SLS Storage Ring: Manufacturing and Magnetic Measurements," *IEEE Trans. of Appl. Super.* vol. 12, no. 1, 51–54 (2002).
- [3.1.27] J. Safranek, C. Limborg, A. Terebilo, K.I. Blomqvist, P. Elleaume, and Y. Nosochkov, "Nonlinear Dynamics in a SPEAR Wiggler," *Phys. Rev. ST* **5**, 010701 (2002).
- [3.1.28] C. Steier, G. Portmann, and A. Young, "Commissioning of the First Elliptically Polarizing Undulator at the ALS," pp. 2343–2345, EPAC00.
- [3.1.29] B. Singh, and A. Streun, "Limits for Normal and Skew Sextupole and Octupole Field Errors in the First (I_1) and Second (I_2) Field-Integrals of Insertion Devices planned for SLS," SLS-TME-TA-2001-0170 (2001).
- [3.1.30] "1-2 GeV Synchrotron Radiation Source Conceptual Design Report," LBNL PUB-5172 (1986).
- [3.1.31] G. Portmann, D. Robin, and L. Schachinger, "Automated Beam Based Alignment of the ALS Quadrupoles," pp. 2693–2695, EPAC96.
- [3.1.32] S.L. Kramer, "Beam Based Alignment," NSLS-II Tech Note (2006).
- [3.1.33] J. Bengtsson, and I. Pinayev, "NSLS-II: Control of Vertical Emittance," NSLS-II Tech Note (2006).
- [3.1.34] C. Steier, D. Robin, A. Wolski, G. Portmann, and J. Safranek, "Coupling Correction and Beam Dynamics at Ultralow Vertical Emittance in the ALS," pp. 3213–3215, PAC03.
- [3.1.35] D. Robin, E. Forest, C. Pellegrini, and A. Amiry, "Quasi-Isochronous Storage Rings," *Phys. Rev. E* **48**, 2149–2156 (1993).
- [3.1.36] L. Smith, "Effect of Wigglers and Undulators on Beam Dynamics" LBL-21391 (1986).
- [3.1.37] Y. Wu, V.N. Litvinenko, and J.M.J. Madey, "Lattice and Dynamic Aperture of the Duke FEL Storage Ring," pp. 218–220, PAC93.
- [3.1.38] T. Shaftan and J. Bengtsson, "Impact of Insertion Devices on the NSLS-II lattice," NSLS-II Tech. Note (2006).
- [3.1.39] T. Shaftan, J. Bengtsson, and S. Kramer, "Control of Dynamic Aperture with Insertion Devices" pp. 3490–3492, EPAC06.

- [3.1.40] P. Elleaume “A New Approach to the Electron Beam Dynamics in Undulators and Wigglers” pp. 661-663, EPAC92.
- [3.1.41] J. Chavanne, P. Van Vaerenbergh, P. Elleaume, T. Günzel, “Recent Achievements and Future Prospect of ID Activities at the ESRF” pp. 2346–2348, EPAC00.
- [3.1.42] J. Bahrtdt, W. Frentrup, A. Gaupp, M. Scheer, G. Wüstefeld “Dynamics Multipole Shimming of the APPLE Undulator UE112” pp. 941–943, PAC07.

3.2 Collective Effects

3.2.1 Introduction

In this section, we discuss the effect of multi-particle interactions [3.2.1] on the electron beam in the NSLS-II storage ring. The storage ring has 500 MHz RF and a revolution period of 2.6 μs . The baseline design configuration corresponds to filling 80% (or 90%) of the RF buckets and leaving one or more gaps to allow for ion clearing. In this case we have $M = 1040$ bunches, each containing $N_e = 7.8 \times 10^9$ electrons ($N_e e = 1.25$ nC) corresponding to a total average current $I_{av} = MN_e e / T_0 = 500$ mA and a single-bunch current $I_0 = N_e e / T_0 = 0.5$ mA. For an RMS bunch duration $\sigma_t = 15$ ps, the peak bunch current is $I_p = N_e e / \sqrt{2\pi}\sigma_t = 33$ A.

Limitations on the single bunch current result from the short-range wakefield (broadband impedance). The longitudinal microwave instability depends primarily on the impedance of the vacuum vessel. The transverse mode coupling instability depends on the resistive wall impedance and the geometric impedance due to changes in the vacuum chamber cross-section.

Limitations on the total average current arise from the long-range wakefield (narrowband impedance). The longitudinal coupled-bunch instability is predominantly driven by the longitudinal higher-order modes in the RF cavity. The transverse coupled-bunch instability is primarily due to the resistive wall and the transverse higher-order modes in the RF cavity.

The most accurate approach to estimating the instability thresholds for NSLS-II is to carry out computer simulation tracking studies using the wakefields determined by numerical calculations of the wakefield for each component comprising the storage ring. This is a large effort that is now underway. Here, we shall provide estimates of the instability thresholds using a simplified model of the ring impedance, which has been developed based on impedance calculations performed to-date and on the experience at existing storage rings [3.2.2], especially APS and ESRF. We also present results of impedance calculations obtained thus far using the electromagnetic simulation code GdfidL [3.2.3].

In addition to the wakefield effects mentioned above, we also discuss intrabeam scattering. We report estimates of the Touschek lifetime resulting from single scattering, and of the increase in emittance due to multiple scattering.

We plan to use third-harmonic Landau cavities to increase the bunch length and synchrotron tune spread. Lengthening the bunch will be useful in raising the longitudinal microwave instability threshold, increasing the Touschek lifetime and reducing the effect of intrabeam scattering on the emittance. Increasing the bunch length and synchrotron tune spread improves the effectiveness of positive chromaticity in raising the single and coupled bunch transverse instability thresholds. The beam dynamics issues involved in the operation of the Landau cavities will be addressed.

3.2.2 Wakefields and Impedance

We provide a short overview of wakefields and impedance [3.2.4, 3.2.5] to clarify the approach we plan to adopt. Consider a point charge q (the drive particle) traveling very close to the speed of light in the z -direction through a vacuum enclosure displaced from the design trajectory by \vec{r}_d . A unit test charge travels at a distance s behind the first (Figure 3.2.1) on a trajectory parallel to the z -axis but displaced by $\vec{r}_t = (x, y)$.

The change of momentum $\Delta \vec{p}$ of the second particle, caused by the electromagnetic field of the first, is given by

$$\Delta \vec{p} = \int_{-\infty}^{\infty} dt \left[\vec{E}(\vec{r}_t, z, t) + c \hat{z} \times \vec{B}(\vec{r}_t, z, t) \right]_{z=ct-s}. \quad (3.2-1)$$

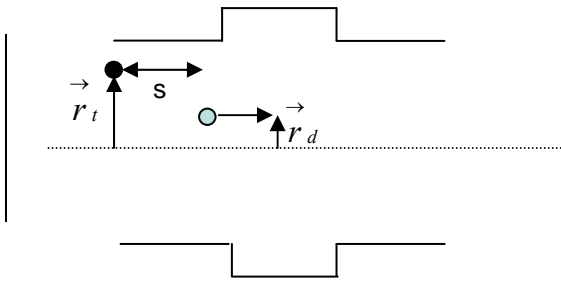


Figure 3.2.1. A drive particle d leading a test particle t through a vacuum structure.

For $\vec{r}_t = \vec{r}_d = 0$, we define the longitudinal wakefield $w_{\parallel}(s)$ [volt/coul] by

$$w_{\parallel}(s) = -\frac{c}{q} \Delta p_z = -\frac{1}{q} \int_{-\infty}^{\infty} dz E_z \left(z, t = \frac{z+s}{c} \right), \quad (3.2-2)$$

and the longitudinal impedance $Z_{\parallel}(k)$ [ohms] is determined by the Fourier transform,

$$Z_{\parallel}(k) = \int_{-\infty}^{\infty} \frac{ds}{c} w_{\parallel}(s) e^{iks}. \quad (3.2-3)$$

For a Gaussian bunch containing N_e electrons, the energy loss is $\Delta E = \kappa_{\parallel} (eN_e)^2$ and the power loss is $P = \kappa_{\parallel} I_0^2 T_0$, where the energy loss factor κ_{\parallel} [V/C] is given by

$$\kappa_{\parallel} = \int_{-\infty}^{\infty} \frac{cdk}{2\pi} \text{Re} Z_{\parallel}(k) e^{-k^2 \sigma_s^2}. \quad (3.2-4)$$

The transverse wakefield [V/C-m] is

$$\vec{w}_{\perp} \left(s, \vec{r}_t, \vec{r}_d \right) = \frac{c}{q} \Delta \vec{p}_{\perp} = \frac{1}{q} \int_{-\infty}^{\infty} dz \left[\vec{E}(\vec{r}, z, t) + c \hat{z} \times \vec{B}(\vec{r}, z, t) \right]_{t=\frac{z+s}{c}}. \quad (3.2-5)$$

The transverse impedance \vec{Z}_{\perp} [Ω/m] is determined by the Fourier transform,

$$\vec{Z}_{\perp}(\vec{r}_t, \vec{r}_d, k) = \frac{-i}{c} \int_0^{\infty} ds w_{\perp}(\vec{r}_t, \vec{r}_d, s) e^{iks}. \quad (3.2-6)$$

When the vacuum enclosure has reflection symmetry about the xz and yz planes, the transverse wakefield vanishes for $\vec{r}_t = \vec{r}_d = 0$ and the first terms in a Taylor expansion yield [3.2.6],

$$w_x(s, x_t, x_d) \cong w_{Dx}(s)x_d + w_{Qx}(s)x_t \quad (3.2-7)$$

$$w_y(s, y_t, y_d) \cong w_{Dy}(s)y_d - w_{Qy}(s)y_t \quad (3.2-8)$$

where w_D is the dipole wakefield and w_Q is the quadrupolar wake. The dipole and quadrupolar impedances are determined by the Fourier transforms

$$Z_x(x_t, x_d, k) \cong Z_{Dx}(k)x_d + Z_{Qx}(k)x_t \quad (3.2-9)$$

$$Z_y(y_t, y_d, k) \cong Z_{Dy}(k)y_d - Z_{Qy}(k)y_t \quad (3.2-10)$$

The coherent betatron tune shift in a Gaussian bunch of N_e electrons produced by the transverse dipole impedance is approximately given by

$$\Delta \nu_{x,y} = \frac{e^2 N_e}{4\pi E} \sum_j \beta_{x,y,j} \kappa_{x,y,j}, \quad (3.2-11)$$

where E is the electron energy and $\beta_{x,y,j}$ is the average value of the betatron function at the j^{th} impedance element and $\kappa_{x,y,j}$ [V/C-m] is the kick factor of the j^{th} element defined by

$$\kappa_{x,y,j} = \frac{c}{\pi} \int_0^{\infty} dk \text{Im} Z_{Dx,y,j}(k) e^{-k^2 \sigma_s^2}. \quad (3.2-12)$$

In a similar manner the quadrupolar impedance contributes to an incoherent tune spread. Some authors employ the effective impedance $(Z_{x,y})_{\text{eff}}$ defined by

$$(Z_{x,y})_{\text{eff}} = \frac{\int_0^{\infty} dk Z_{Dx,y}(k) e^{-k^2 \sigma_s^2}}{\int_{-\infty}^{\infty} dk e^{-k^2 \sigma_s^2}} \quad (3.2-13)$$

The kick factor is related to the effective impedance by

$$\kappa_{x,y} = \frac{c}{2\sqrt{\pi}\sigma_s} \text{Im}(Z_{Dx,y})_{\text{eff}}. \quad (3.2-14)$$

To estimate instability thresholds, we use a model in which the impedance is comprised of a broadband resonator plus the resistive wall. The analytic forms for the wakefield and impedance of these elements are summarized in Table 3.2.1.

Table 3.2.1 Analytic Expressions for Impedance and Wakefield.

Resonator	
$Q' = \sqrt{Q^2 - 1/4} \quad k_r' = k_r Q' / Q$	
$w_{\parallel}(s) = \frac{ck_r R_s}{Q_s} \exp\left(-\frac{k_r s}{2Q_s}\right) \left[\cos k_r' s - \frac{1}{2Q_s'} \sin k_r' s \right]$	$w_{\perp}(s) = \frac{ck_r R_{\perp}}{Q_{\perp}'} \exp\left(-\frac{k_r s}{2Q_{\perp}'}\right) \sin k_r' s$
$Z_{\parallel}(k) = \frac{R_s}{1 - iQ_s(k/k_r - k_r/k)}$	$Z_{\perp}(k) = \frac{k_r}{k} \frac{R_{\perp}}{1 - iQ_{\perp}(k/k_r - k_r/k)}$
$\kappa_{\parallel} = \frac{\omega_r R_s}{2Q_s} \quad (k_r \sigma_s \ll 1)$	$\kappa_{\perp} \cong \frac{1}{\sqrt{\pi}} \frac{c R_{\perp}}{Q_{\perp}} (k_r^2 \sigma_s) \quad (k_r \sigma_s \ll 1)$
$\kappa_{\parallel} = \frac{\omega_r R_s}{4\sqrt{\pi} Q_s^2 (k_r \sigma_s)^3} \quad (k_r \sigma_s \gg 1)$ $(Z/n)_0 = R_s (\omega_0 / \omega_r)$	$\kappa_{\perp} \cong \frac{c}{2\sqrt{\pi} \sigma_s} \frac{R_{\perp}}{Q_{\perp}} \quad (k_r \sigma_s \gg 1)$
Resistive Wall [3.2.7]	
$s_0 = (2b^2 / Z_0 \sigma_{\text{cond}})^{1/3}$	
$w_{\parallel}(s) \cong \frac{-cZ_0 L}{4\pi\sqrt{2\pi} b^2} \left(\frac{s_0}{s}\right)^{3/2} \quad (s \gg s_0)$	$w_{\perp}(s) \cong \frac{cZ_0 s_0 L}{2\pi b^4} \sqrt{\frac{2s_0}{\pi s}} \quad (s \gg s_0)$
$Z_{\parallel}(k) \cong \frac{(1-i)Z_0 s_0 L}{4\pi b^2} \sqrt{k s_0} \quad (0 \leq k \ll 1/s_0)$	$Z_{\perp}(k) \cong \frac{2}{kb^2} Z_{\parallel}(k) \quad (0 \leq k \ll 1/s_0)$
$\kappa_{\parallel} \cong 1.2 \frac{cZ_0}{4\pi} \frac{L}{2\pi b^2} \left(\frac{s_0}{\sigma_s}\right)^{3/2}$	$\kappa_{\perp} \cong 0.58 \frac{cZ_0}{4\pi} \frac{2s_0 L}{b^4} \sqrt{\frac{s_0}{\sigma_s}}$
Extreme Anomalous Skin Effect [3.2.8]	
$s_0 = (Bb)^{3/5} / \sin(\pi/10)$	
$B = 3^{1/6} 2^{-4/3} \pi^{-1/3} Z_0^{-1/3} (l / \sigma_{\text{cond}})^{1/3} \cong 3.9 \times 10^{-7} m^{2/3} \quad (\text{Cu @ 4 K, specular reflection})$	
$w_{\parallel}(s) \cong \frac{-2cB Z_0 L}{3\pi \Gamma(1/3)b} s^{-5/3} \quad (s \gg s_0)$	$w_{\perp}(s) \cong \frac{2cB Z_0 L}{\pi \Gamma(1/3)b^3} s^{-2/3} \quad (s \gg s_0)$
$Z_{\parallel}(k) \cong \frac{(1-\sqrt{3}i)B Z_0 L}{2\pi b} k^{2/3} \quad (0 \leq k \ll 1/s_0)$	$Z_{\perp}(k) \cong \frac{2}{b^2 k} Z_{\parallel}(k) \quad (0 \leq k \ll 1/s_0)$
$\kappa_{\parallel} = 0.16 \frac{cZ_0}{4\pi} \frac{L}{\pi b^2} \left(\frac{s_0}{\sigma_s}\right)^{5/3}$	$\kappa_{\perp} \cong 0.21 \frac{cZ_0}{4\pi} \frac{2s_0 L}{b^4} \left(\frac{s_0}{\sigma_s}\right)^{2/3}$

3.2.3 Estimates of Instability Thresholds

To estimate the instability thresholds, we considered an approximate model of the storage ring impedance, including the long-range wakefield due to the longitudinal and transverse higher-order modes in the CESR-B cavities. The storage ring vacuum chamber is approximated by 720 m of aluminum with a vertical half-aperture of 12.5 mm. We also included 20 in-vacuum undulators, each with 3 m copper chambers of vertical half-aperture 2.5 mm. The geometric impedance due to cross-section changes in the vacuum vessel is approximated by longitudinal and transverse broadband resonators. The parameters for the resonators are based on experience at other storage rings [3.2.2, 3.2.9], especially APS and ESRF, as well as on the impedance calculations we have performed to date. We believe the model is conservative and that it may be possible to build NSLS-II with lower impedance. The details of the impedance model are presented in Table 3.2.2, and some key parameters needed in the estimation of instability thresholds are given in Table 3.2.3.

Table 3.2.2 Impedance Model.

CESR-B cavity higher-order modes (see Tables 3.2.4 and 3.2.5.)	$\beta_x = 20m$
720 m of aluminum with half-gap of 12.5 mm and $\beta_{av} = 7.6$ m:	$\kappa_{\parallel} = 4.0V / pC$ $\kappa_y = 0.68KV / pC / m$
60 m of copper with half-gap of 2.5 mm and $\beta_{av} = 2$ m:	$\kappa_{\parallel} = 1.3V / pC$ $\kappa_y = 5.6KV / pC / m$
Transverse broadband impedance with $f_r = 30$ GHz, $R_y = 1$ M Ω /m, $Q_y=1$, and $\beta_{av} = 7.6$ m $\kappa_y = 19KV / pC / m$	
Longitudinal broadband impedance with $f_r = 30GHz$, $R_s = 30k\Omega$,	$(\text{Im}Z_{\parallel}/n)_0 = 0.4\Omega$ $\kappa_{\parallel} = 35V / pC$

Table 3.2.3 Parameters for Threshold Calculations

Energy, E [GeV]	3
Revolution period, T_0 [μ s]	2.6
Momentum compaction, α	3.7×10^{-4}
Energy loss, U [keV]	1172
RF voltage, V [MV]	3.7
Synchrotron tune, ν_s	0.0094
Damping time: τ_x, τ_s [ms]	13, 6.5
Energy spread, σ_{ϵ_0} [%]	0.09
Bunch duration, σ_{t_0} [ps]	15

3.2.3.1 Transverse Mode Coupling Instability (TMCI)

An approximate relation [3.2.10] determining the threshold of the TMCI at zero chromaticity is given by

$$\frac{\Delta v_y}{\nu_s} = \frac{eI_0^{th}}{2E\nu_s\omega_0} \sum_j \beta_{y_j} \kappa_{y_j} \cong 0.7, \quad (3.2-15)$$

where I_0^{th} is the threshold bunch current, β_{y_j} is the average value of the vertical beta function in the j^{th} element, and κ_{y_j} is its kick factor. $E = \gamma mc^2$ is the electron energy and ν_s is the synchrotron tune. Consider

a current of 0.5 mA bunch. Using the NSLS-II parameters as described in Table 3.2.3, we find that to be below the TMCI threshold requires

$$\sum_j \beta_{y_j} \kappa_{y_j} < 180 \text{ KV} / \text{pC} . \quad (3.2-16)$$

Using the values of the kick factors and beta functions as specified in Table 3.2.2, we find that $\sum_j \beta_{y_j} \kappa_{y_j} = 160 \text{ KV} / \text{pC}$. Therefore, 0.5 mA bunches are below the TMCI threshold for zero chromaticity.

3.2.3.2 Longitudinal Microwave Instability

At very low single-bunch current, the longitudinal density is determined by the equilibrium between radiation damping and quantum fluctuations. As the bunch current increases, the longitudinal charge distribution is modified by the wakefield. Below the threshold of the microwave instability, the energy distribution remains unchanged, and the longitudinal charge distribution $f_0(\tau/\sigma_{\tau_0})$ is determined by the time-independent solution of the Haissinski equation [3.2.11],

$$f_0(q) = A \exp \left[-\frac{1}{2} q^2 + S \int_q^\infty dq' \int_{q'}^\infty dq'' f_0(q'') w(q'' - q') \right], \quad (3.2-17)$$

where the constant A is chosen to satisfy the normalization

$$\int_{-\infty}^{\infty} dq f_0(q) = 1 \quad (3.2-18)$$

In the case of a broadband resonator with shunt impedance R_s , resonant frequency ω_s , and quality factor $Q_s = 1$, the scaled current is defined by

$$S = \frac{e I_0 R_s \omega_r}{E_0 v_s \omega_0 \sigma_\varepsilon} \quad (3.2-19)$$

and

$$w(q) = \exp \left(-\frac{q \omega_r \sigma_{t_0}}{2} \right) \left[\cos(q \omega_r \sigma_{t_0}) - \frac{1}{2\sqrt{0.75}} \sin(q \omega_r \sigma_{t_0}) \right]. \quad (3.2-20)$$

In Figure 3.2.2, we show the Haissinski distribution for bunch currents of 0.1 mA and 0.4 mA.

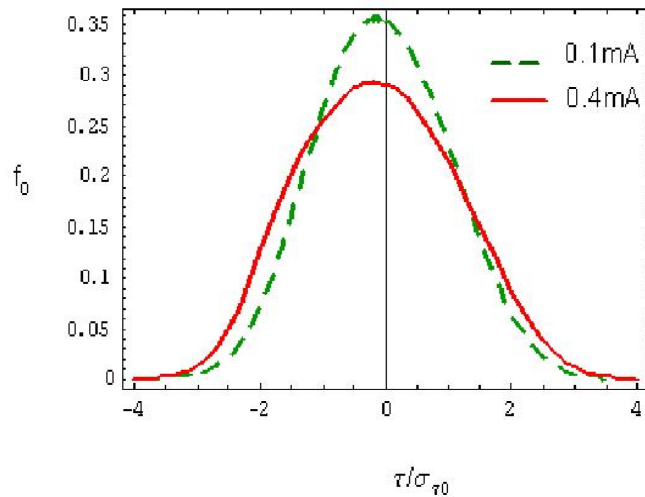


Figure 3.2.2 Longitudinal distribution as determined from the Haissinski equations.

Once the current exceeds the microwave instability threshold, both the energy distribution and the charge distribution are modified and are no longer time-independent. In the case of a broadband resonator with shunt impedance R_s , resonant frequency ω_s , and quality factor $Q_s = 1$, Oide and Yokoya [3.2.12] have shown that the single-bunch current threshold is given by

$$I_0^{th} = \frac{E v_s \sigma_\varepsilon}{e R_s (\omega_r / \omega_0)} S(\omega_r \sigma_{t_0}). \quad (3.2-21)$$

In Figure 3.2.3, we show the function $S(\omega_r \sigma_{t_0})$ as determined by Oide and Yokoya (solid curve), and by tracking using the computer code ELEGANT [3.2.13] (symbols). A useful fit to the scaling function, in the regime $x > 0.2$, is given by

$$S(x) = 11 + 9.4(x - 0.7)^2. \quad (3.2-22)$$

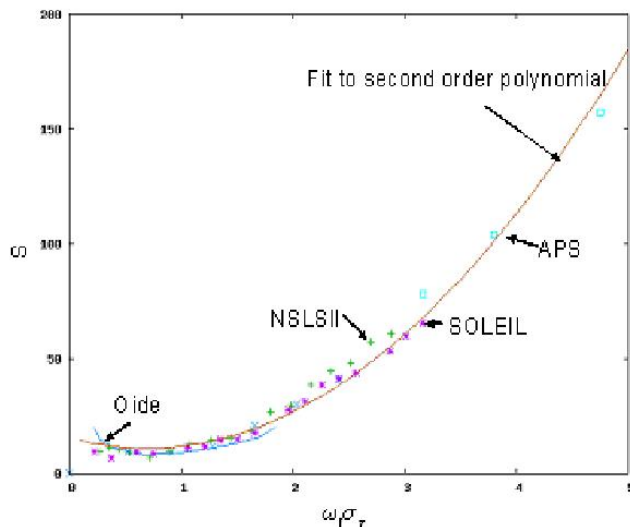


Figure 3.2.3. The scaling function $S(\omega_r \sigma_{t_0})$ as determined by Oide and Yokoya (solid blue curve) and by tracking using ELEGANT (characters). The threshold is defined to be when the energy spread has increased by 5% over the zero current value.

In the limit when $\omega_0 \sigma_{t0} \gg 1$, the threshold condition becomes

$$I_0^{th} = 9.4 \frac{E v_s^2}{e \alpha (\text{Im} Z / n)_0} (\omega_0 \sigma_{t0})^3, \quad (3.2-23)$$

where $(\text{Im} Z / n)_0 = R_s (\omega_0 / \omega_r)$. This has the same form as the Boussard [3.2.14] criterion, except that in the Boussard case, the constant 9.4 is replaced by the smaller value $\sqrt{2\pi}$. The reason that the Boussard criterion gives too pessimistic a threshold is that it does not take into account the bunch lengthening due to potential well distortion.

In Figure 3.2.4, we show the dependence of the bunch length and the energy spread as calculated using the program ELEGANT. This shows that 0.5 mA bunches will suffer negligible increase in energy spread due to the longitudinal microwave instability.

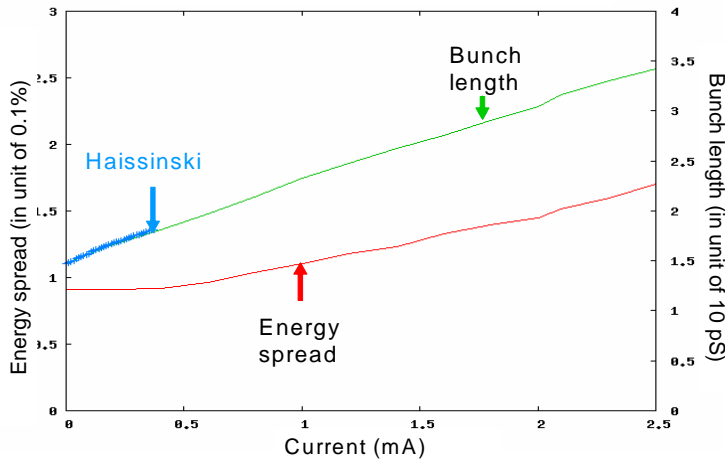


Figure 3.2.4. Bunch length and energy spread for broadband resonator. Resonant frequency $f_y = 30$ GHz, shunt impedance $R_s = 30$ k Ω , and $Q_s = 1$. This corresponds to $(\text{Im} Z / n)_0 = 0.4$ Ω .

3.2.3.3 Transverse Coupled Bunch Instability Driven by Resistive Wall Impedance

As discussed in Section 3.2.3.1, the short-range part of the resistive wall impedance contributes to the single-bunch TMCI. The long-range tail contributes to the transverse coupled bunch instability. A rough approximation to the growth rate of the fastest growing transverse coupled bunch mode driven by the resistive wall impedance (at zero chromaticity) is given by

$$\frac{1}{\tau_{gr}} \cong \frac{e c I_{av} \beta_y}{2 E C} \text{Re} Z_{\perp}^{rw}(\omega_0) \frac{1}{\sqrt{1-q}}, \quad (3.2-24)$$

where $C = 792$ m is the ring circumference, β_y is the average value of the vertical beta function in the resistive wall, and $q = 0.28$ is the fractional part of the vertical tune. Equating the growth time to the radiation damping time provides an estimate of the instability threshold. Using the model parameters given in Tables 3.2.2 and 3.2.3, we find the threshold is at a total average current of 15 mA, far below the design value of 500 mA. Running at positive chromaticity will increase this threshold value.

Particle tracking [3.2.15] has been used to estimate transverse stability thresholds for coupled bunch modes. In these calculations we include both the long-range and short-range resistive wall wakefields as well as the short-range longitudinal and transverse wakefields, as described in Table 3.2.2. To keep the problem

manageable, we assume that all RF buckets contain identical bunches interacting via a single coupled bunch mode. A single bunch is tracked and the effect of other bunches is obtained by appropriate phase shifts under the assumption that the coherent frequency shift is small compared to the characteristic frequency width in the long-range transverse impedance. This should be an excellent approximation for the resistive wall impedance, which dominates the long-range transverse wake. The resistive wall impedance is due to 60 m of Cu with vertical aperture 5 mm and average beta function 2 m, in conjunction with 720 m of Al with aperture 25 mm and average beta function 7.6 m. The broadband transverse resonator has $R_{\perp} = 1$ M-Ohm/m with $Q_{\perp} = 1$ and 30 GHz resonant frequency at beta function 7.6 m. A longitudinal resonator with $R_s = 30$ k-Ohm, resonant frequency 30 GHz, and $Q_s = 1$ dominates the longitudinal impedance.

Three cases were simulated. Case 0 is a “stripped” case with no longitudinal wakes, no quadrupolar wakes (also referred to as detuning wakes), and no third-harmonic RF. Case 1 has the full suite of collective effects but no third harmonic cavity. Case 2 includes a perfect third harmonic cavity. The single-bunch threshold current as a function of vertical chromaticity is shown in Figure 3.2.5. In cases 1 and 2, a chromaticity of 4 allows for an average bunch current of about 0.5 mA and hence for an average stored current of 500 mA. This demonstrates the importance of running at positive chromaticity. Note also that bunch lengthening and enhanced synchrotron frequency spread introduced by the longitudinal wakefield and the third-harmonic cavity increase the effectiveness of positive chromaticity to stabilize the beam.

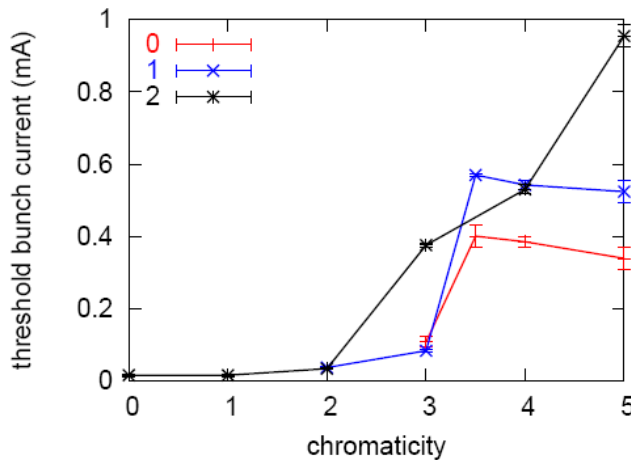


Figure 3.2.5 Threshold single bunch current vs. chromaticity for: (0) no longitudinal wakes, no quadrupolar wakes, and only fundamental RF; (1) all the impedances but only fundamental RF; (2) all impedances as well as fundamental and third-harmonic RF.

3.2.3.4 CESR-B Cavity Longitudinal Impedance and Coupled Bunch Growth Rates

The longitudinal higher-order modes (HOM) in an RF cavity can result in coupling between bunches, leading to unstable synchrotron oscillations. In the case of M equally spaced and populated point bunches, the coherent synchrotron frequency Ω_{μ} of the μ^{th} multi-bunch mode can be approximated by

$$\Omega_{\mu} - \omega_0 \nu_s = \frac{i e \alpha \omega_0 I_{av}}{4 \pi \nu_s E} \sum_{j=-\infty}^{\infty} (M j + \mu) Z_{\parallel} [(M j + \mu + \nu_s) \omega_0] \quad (3.2-25)$$

and

$$(\mu = 0, 1, 2, \dots, M - 1). \quad (3.2-26)$$

A 3D GdfidL [3.2.3] model has been created for the CESR-B cavity [3.2.16]. The model consists of the niobium cavity with the asymmetric beam tubes, warm-to-cold transitions, and ferrite-lined HOM dampers,

and it tapers to the 25×50 mm elliptical ring beampipes. The cavity has a fluted beam tube that allows the lowest dipole mode to be coupled out to the HOM damper. This made it essential to use a 3D model for calculating the HOMs. To benchmark such a complex model, C-Fish [3.2.17] and Superfish [3.2.18] models of the cavity with complex permittivity and permeability were created. The results were compared to GdfidL and to measured data on a ferrite-lined pillbox cavity that was measured on the bench.

The Superfish model approximates the fluted beampipe by a cylindrical tube with the same cutoff frequency. An outline of the cavity geometry with the field lines of the 1586 MHz mode is shown in Figure 3.2.6.

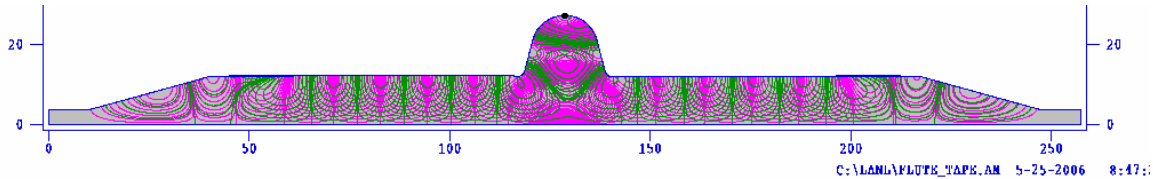


Figure 3.2.6 CESR-B cavity geometry input to C-Fish.

The first eight HOMs calculated are given in Table 3.2.4. Superfish correctly calculates the surface resistivity of niobium as a function of frequency, but only takes the complex permeability and permittivity as a single input. The permittivity of the ferrite load is relatively constant and does not contribute significantly to damping the HOM, but the ferrite permeability properties vary considerably, so specific values (Table 3.2.4) closest to the HOM frequencies were calculated. The ferrite properties were obtained from the Canadian Light Source [3.2.19]. The measurements were made at several discrete frequencies in the band of interest.

Table 3.2.4 CESR-B Higher-Order Longitudinal Modes.

Superfish			GdfidL		
Frequency (MHz)	Shunt Impedance (Ohms)	Q	Frequency (MHz)	Shunt Impedance (Ohms)	Q
952.4	112	222	950.55	8.14	350
973.32	57.07	332	976.62	54.6	420
1014.85	498	112	1014.38	505	150
1184.65	44.1	43	1181.5	13.2	60
1331.15	38.7	40	1361	65.6	20
1487.5	12.5	53	1481.5	46	40
1586.58	27.8	169	1580	7.5	30

We also performed studies of HOMs in CESR-B assembly using GdfidL code, shown in Figure 3.2.7. The studies took off from time-domain simulation of 1 pC charge passing through the structure. For the longitudinal impedance computation, the beam is moving on-axis, in comparison with the transverse impedance computation when the beam trajectory is shifted off-axis with an offset taken as 3×STEPSIZE. To get a result for the impedance, which is Fast Fourier Transforming of the wake function with higher frequency resolution, the wakepotential is computed up to an s-value of 50 meters. Parameters of the ferrite material are taken as $\epsilon_r = 13.4$, $\mu_r = 0.9$, $\tan\delta_\epsilon = 0.02$, $\tan\delta_\mu = 2.33$, $\sigma_\epsilon = 0.05 \Omega^{-1}/\text{m}^{-1}$, and $\sigma_\mu = 46395 \Omega/\text{m}$ at a frequency of 2.8 GHz [3.2.19].

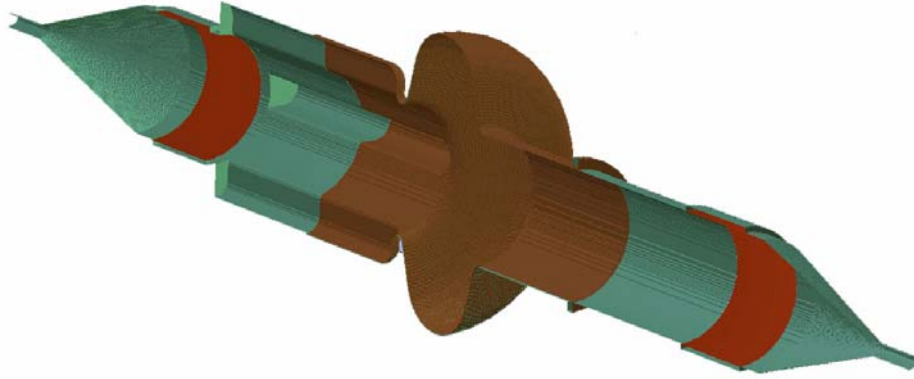


Figure 3.2.7 3D model of CCSR-B cavity assembly in GdfidL.

These parameters were used in ZAP [3.2.20] to calculate the growth rates for nominal ring and beam parameters. The maximum growth time was 120 ms for the sum of three cavity impedances, much longer than the longitudinal damping time of 6.5 ms, and so the beam is longitudinally stable for cavity HOMs.

To summarize the CCSR-B cavity studies, longitudinal CB growth rates were calculated for the first few HOM of the CCSR-B cavity and were found to be below the damping rate, even for three installed cavities without stagger tuning. However, the combination of small-bunch length exciting higher frequency modes and ferrite loss decreasing at higher frequency could lead to unstable modes whose growth rate exceeds the damping rate, so this analysis must be extended to higher frequencies. To enable this, we are pursuing measurements of the ferrite properties to 6 GHz with Ron Hutcheon, who provided the data below 3 GHz that were used in these calculations. This work must also be extended to the third harmonic cavities.

3.2.3.5 CCSR-B Cavity Transverse Impedance and Coupled Bunch Growth Rates

The transverse higher-order modes in an RF cavity can result in coupling between bunches, leading to unstable betatron oscillations. In the case of M equally spaced and populated point bunches, the coherent synchrotron frequency Ω_μ of the μ^{th} multi-bunch mode can be approximated by

$$\Omega_\mu - \omega_0 \nu_x = -i \frac{ecI_{av}}{2E} \frac{\beta_x^{cav}}{C} \sum_{j=-\infty}^{\infty} Z_\perp [(Mj + \mu + \nu_y)\omega_0], \quad (3.2-27)$$

where $\mu = 0, 1, 2, \dots, M-1$). The same GdfidL model used to compute the longitudinal cavity impedances was used to compute the transverse modes. The first 15 modes are listed in Table 3.2.5.

Table 3.2.5 CESR-B Higher-Order Transverse Modes.

Time domain #	Frequency [MHz]	R_{\perp} [k Ω /m]	$Q_{\perp,load}$
f_1	608	2.2	60
f_2	653	3.1	60
f_3	681	15.6	70
f_4	769	1.6	30
f_5	864	1.03	50
f_6	917	0.72	40
f_7	964	0.66	30
f_8	1045	0.8	30
f_9	1146	1.17	30
f_{10}	1243	2.3	70
f_{11}	1299	0.36	160
f_{12}	1344	0.31	40
f_{13}	1405	0.33	70
f_{14}	1433	0.22	100
f_{15}	1464	0.44	70

The horizontal betatron function is 20 m at the RF cavities. These modes were used in ZAP [3.2.20] to calculate the transverse coupled-bunch growth rates. For 500 mA average current distributed uniformly in all the buckets around the ring and zero chromaticity, the coupled bunch growth time is 40 ms, which is longer than the radiation damping time of 13 ms. Therefore, the transverse cavity modes will not lead to unstable coupled-bunch betatron oscillations.

3.2.4 Impedance Budget

Extensive calculations have been performed of the wakefield and impedance produced by the storage ring components. Results of the calculations are summarized in Table 3.2.6, where we present the longitudinal kick factor (Eq. 3.2-4), the transverse kick factors (Eq. 3.2-12) and the imaginary part of the longitudinal impedance at low frequency divided by $n = \omega/\omega_0$, where $\omega_0 = 2\pi \times 384.6 \text{ kHz}$. The values given correspond to a single element. The number of times a given object is located in the ring is stated.

Table 3.2.6 Calculated Impedance for Storage Ring Components.

Object	Number of occurrences	κ_{\parallel} V/pC	$(\text{Im}Z_{\parallel}/n)\omega\Omega$	κ_x V/pC/m	κ_y V/pC/m
Absorber	180	3.4×10^{-3}	9.2×10^{-6}	0.5	0.002
Bellows ¹	180	8.7×10^{-3}	124×10^{-6}	0.8	2
BPM	200	20×10^{-3}	47×10^{-6}	0.9	1.1
Cavity transitions/straight	2	3.5	14×10^{-3}	25.4	57
500 MHz CESR-B cavity	4	0.31	----	0.17	0.17
1500 MHz CESR-B cavity	4	0.52	----	2.6	2.6
Dipole Chamber	60	3.3×10^{-5}	0.7×10^{-7}	4.5×10^{-3}	0
Multipole Chamber	90	0.5×10^{-5}	0.1×10^{-7}	0.7×10^{-3}	0
Flange ¹	300	0.47×10^{-3}	16×10^{-6}	0.141	0.141
Injection Region	1	TBD	TBD	TBD	TBD
SCU chamber geometric	TBD	22.6×10^{-3}	0.6×10^{-3}	61	257
SCU chamber ease (2.5 m)	TBD	5.6×10^{-3}	----	13	26
IR chamber ²	4	0.84	2.1×10^{-3}	11.4	22.6
CPMU geometric	TBD	95×10^{-3}	1.1×10^{-3}	136	425
CPMU resistive wall (3.5 m)	TBD	66×10^{-3}	----	112	225
720 m Al resistive wall	1	4.0	----	272	545
Scraper (Horizontal)	2	0.22	1.4×10^{-3}	22	2
Scraper (Vertical)	2	TBD	TBD	TBD	TBD

The values for the geometric impedances were calculated using GdfidL with $\sigma_s = 3$ mm. The resistive wall and extreme anomalous skin effect estimates were made with $\sigma_s = 4.5$ mm. The bunch-length dependence of the wakefields will be determined in future work. ¹Values for bellows and flanges were calculated by Nagaoka [3.2.21] for SOLEIL with $\sigma_s = 6$ mm. ²The values for a simplified geometry of the far-infrared extraction chamber described in section 3.2.4.3.

The Al vacuum chamber is taken to be of length 720 m with vertical half-height 12.5 mm. The copper-plated RF shield for the in-vacuum permanent magnet undulator is 3 m long with vertical half-height of 2.5 mm. The superconducting undulator chamber is 2 m long with vertical half-height 2.5 mm and is cold copper in the extreme anomalous skin effect regime [3.2.8]. The vertical resistive wall wake of the elliptic chamber is taken to be 0.8 times the value for the circular chamber and the horizontal wake is 0.4 times the circular value [3.2.22]. Results not yet determined are indicated in the table.

3.2.4.1 Insertion Device Chambers

While most of the components listed in Table 3.2.7 are fairly common and have been successfully used in many machines, we feel that significant attention is warranted for studies and optimization of the impedance due to insertion device chambers. This need is based on experience at modern light sources, where installations of small-gap ID chambers have significantly affected beam dynamics [3.2.24], as well as on the requirements for NSLS-II, which is expected to have a large number of ID chambers (~ 20) with gap down to 5 mm beam stay-clear. Both the resistive wall component and the geometric component due to the transitions have been studied. Furthermore, in addition to the dipole impedances, which directly cause beam instabilities, we have estimated the quadrupolar component [3.2.25], which results in incoherent frequency shift and indirectly contributes to the instabilities through the Landau damping.

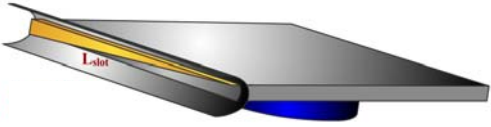
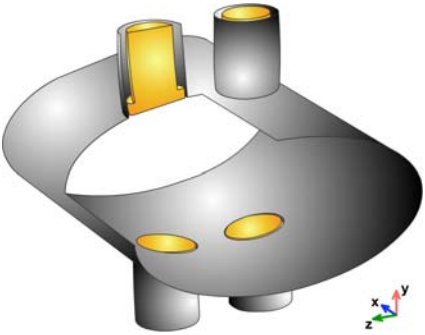


For the purposes of impedance budget we consider two representative ID chamber geometries: 1) a variable-gap, in-vacuum, permanent magnet undulator, and 2) a 5 mm fixed-gap elliptical chamber (4.2 K Cu inner surface) for a superconducting small-gap undulator.

Resistive wall contribution has been estimated analytically. While the inner chamber cross-sections are either complex H-like or elliptical shapes we have conservatively used the formulas in Table 3.2.1 for round

cross-sections. It is known [3.2.22] that as the chamber gets flatter (while height is kept fixed), the longitudinal impedance passes through a minimum equal to about 90% of the round-pipe value, while the transverse impedance monotonically approaches $\sim 80\%$ of its round-pipe value. Copper coating and a minimum full gap of 5 mm were assumed for the estimates.

Geometric impedance contributions due to transitions [3.2.26] were calculated using EM code GdfidL [3.2.3] as well as checked against a recently developed analytical approach [3.2.25].

Table 3.2.7 Description of Components.

	<p>Absorber</p> <p>To protect the vacuum chamber and insertion devices in the ring from damage due to synchrotron radiation, photon absorbers are used. The model consists of a regular elliptical beampipe with a rectangular slot 10 mm high, 180 mm long, and 180 mm deep. A triangular copper burr is located inside the slot for synchrotron radiation absorption. It projects 5 mm inside the regular elliptical beampipe.</p>
	<p>BPM</p> <p>Due to excitation of resonant modes in the buttons, the impedance, kick factor, and loss factor depend very strongly on the BPM button geometry. The BPM button geometry can be optimized to reduce impedance contribution and heating, without losing its resolution. To estimate BPM contribution to the transverse and longitudinal impedance, buttons designed for the SOLEIL BPM were modeled on the regular elliptic beampipe for NSLS-II. Results of the transverse impedance were compared with results for the SOLEIL BPM geometry; in both cases, $50 \Omega/\text{m}$ was computed.</p>
	<p>Dipole Chamber</p> <p>The dipole vacuum chamber for NSLS-II has an elliptical cross-section. Inside the chamber there is a slot 15 mm high. As was shown by Stupakov [3.2.23], the slot length does not affect the impedance. For this numerical computation, the slot length is taken to be 80 mm. The horizontal impedance of this geometry depends on beampipe radius and height of the slot.</p>
	<p>Scraper-H</p> <p>From the impedance estimations of other laboratories, horizontal or vertical beam scrapers can produce impedance comparable with that of a rectangular step or a tapered transition with a small angle of opening. Two scrapers of the presented geometry, one horizontal and the other vertical are under consideration for application in the NSLS-II ring.</p>

3.2.4.1.1 In-Vacuum Undulator

A 3D model of the IVU [3.2.26] is shown in Figure 3.2.8 (a, top). This model is motivated by the geometry of the X13 Mini-Gap Undulator [3.2.27] currently operating at the NSLS x-ray ring and has been tailored to meet the NSLS-II requirements. The device consists of two magnet arrays of width $w_m = 100$ mm and thickness 34 mm, located inside a rectangular vacuum chamber of width $w_{vc} = 180$ mm and height $h_{vc} =$

170 mm. The tapered transition consists of two parts: 1) a fixed portion between the regular beampipe and the undulator vacuum chamber; and 2) a flexible-height portion with one end fixed to the interior of the undulator vacuum chamber and the other end fixed to the moveable magnet array. The flexible portion only consists of flat upper and lower conductive plates with no side walls. For simplicity in the 3D model, we used a continuous smooth taper of length 180 mm. Also, due to mesh limitations, we have shortened the magnet section length to 0.5 m.

Figure 3.2.8 (a, bottom) shows the transverse wakepotential for the considered geometry and 3 mm RMS bunch length. The wakepotential has a Gaussian-like part corresponding to mainly inductive broadband impedance, as well as a characteristic long-range tail.

The short-range wakefield in the IVU is predominantly determined by the tapers; the long-range wake depends on the cross-sectional geometry of the vacuum enclosure and the length of the magnet. The oscillations in the long-range part are due to multiple narrowband impedance resonances that are possible to characterize in terms of waveguide theory [3.2.28]. Due to limitations on the mesh, we have not yet been able to carry out a systematic study of the length dependence.

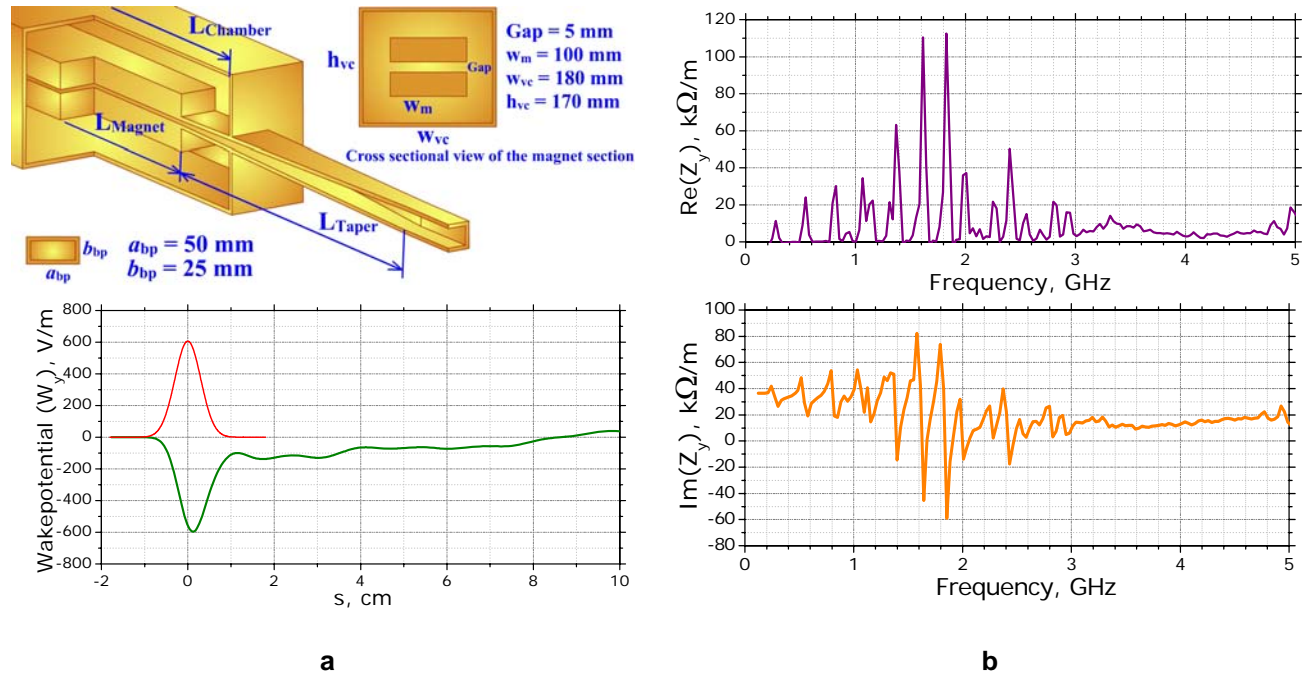


Figure 3.2.8 (a, top) Geometry of CPMU with $L_{\text{taper}} = 180$ mm; (a, bottom) Short-range transverse wakepotential of in-vacuum permanent magnet undulator chamber; (c, top and bottom) Low-frequency behavior of real and imaginary parts of the transverse impedance of CPMU. Impedances determined by FFT of the computed wakepotential up to $s = 7$ m.

3.2.4.1.2 Superconducting Undulator

Similar calculations were performed for the elliptic vacuum chamber of a superconducting undulator. The geometry of the tapered elliptic vacuum chamber is shown in Figure 3.2.9 (a, top). The small-gap magnet region of the elliptic vacuum chamber for the superconducting undulator is fixed and has major axis $2a_s = 15$ mm and minor axis $2b_s = 5$ mm, with a magnet section length of 2000 mm. The tapers must smoothly transition between the magnet section and the regular beampipe, which has a major axis $2a_b = 76$ mm and minor axis $2b_b = 25$ mm.

Transverse impedance in the low-frequency limit and the kick factor for the tapered vacuum chamber are independent of the distance between the tapers. The inner section length was reduced to 100 mm for GdfidL

calculations. The resulting wakepotential for 3 mm RMS long bunch and the taper length of $L_{\text{Taper}} = 180$ mm is shown in Figure 3.2.9 (a, bottom). It corresponds to $\kappa_y = 190$ V/pC/m and $\text{Im}Z_y(\omega \rightarrow 0) = 8.5$ k Ω /m. When we increased the taper length, κ_y and $\text{Im}Z_y(\omega \rightarrow 0)$ decreased inversely proportional to L_{Taper} . The taper length of the elliptic vacuum chamber is chosen to optimize its contribution to the total impedance as well as space in the ring. Note that resonance peaks are observed inside the vacuum chamber in all cases of the transverse impedance calculations. These peaks are not resolved with a wakefield length of 0.3 m. A more detailed investigation of the electrodynamic properties of the tapered elliptic vacuum chamber uncovered the existence of trapped modes. These modes have been identified and classified [3.2.28]. In principle, these modes may affect multi-bunch dynamics and will be systematically studied.

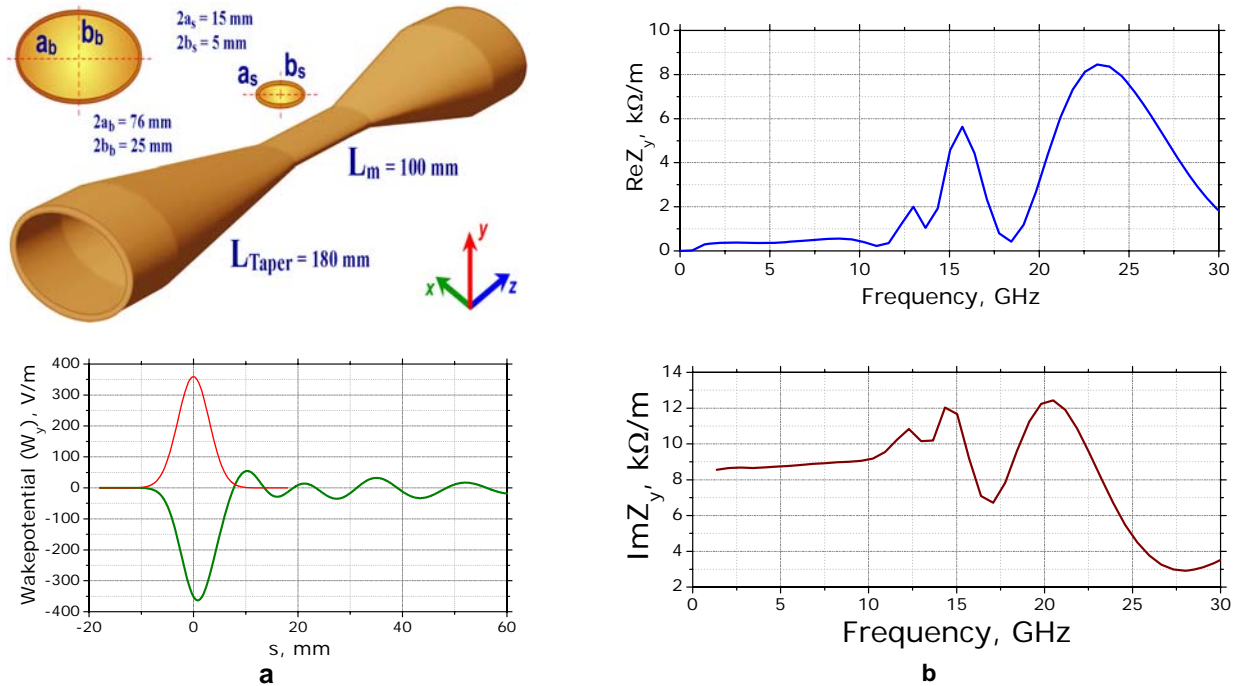


Figure 3.2.9 (a, top) Tapered elliptical vacuum chamber for superconducting small-gap undulator ($L_{\text{Taper}} = 180$ mm). (a, bottom) Transverse wakepotential; (b, top) Real part of the transverse impedance. (b, bottom) Imaginary part of the transverse impedance. Impedances correspond to FFT of the computed wakepotential up to $s = 0.3$ m.

3.2.4.2 CESR-B Short-Range Wake

CESR-B [111] type superconducting cavities are considered for acceleration of the beam in the NSLS-II storage ring. Two main 500 MHz RF cavities and one 2-cell passive 1500 MHz bunch-lengthening harmonic cavity will be fitted in one long straight section. Two long straight sections are reserved in the ring for the RF system. The complicated nature of the RF cavities requires significant computational resources, to establish the longitudinal and transverse impedances for the whole assembly. In order to avoid computational complications, the coupling impedance in the whole assembly can be estimated as a sum the impedance of cavities and transitions [3.2.29, 3.2.30].

Calculated results for the 500 MHz main RF cavity with the attached round beam pipe of radius $a=120$ mm on one side and the fluted beam pipe for Higher Order Modes (HOMs) coupling on the other (Figure 3.2.10a) are presented in Table 3.2.6 (beginning of Section 3.2.4). “Perfect matched layers” (or “port” boundary condition) is used on both sides of the cavity pipe for wakefield analysis. For simplicity, the RF coupler was not included in these computations. The coupling impedance of the rectangular slot in the round

beam pipe, which will be used for matching of the input power to the cavity, can be estimated analytically or can be computed separately and added to the total impedance of the cavity.

The loss factor of the main cavity for a 3 mm bunch length (σ_s) is $\kappa_{loss}=0.31V/pC$ ($\sigma_s \ll a$). Two main cavities per straight contribute the loss factor of 0.62 V/pC. It is about 6 times smaller than the value for the cavity transitions per straight.

To estimate the contribution of the harmonic cavity to the total impedance of the ring we are using a scaled model of the CESR-B main cavity at frequency 1500 MHz. The loss factor of the harmonic cavity is increased by a factor of 1.7 ($\kappa_{loss} \propto \sqrt{g}/a$, where g is the gap of the cavity) due to reduction of the cavity dimensions by a factor of 3. The kick factor of the harmonic cavity is small compared to that due to the cavity transition. Assuming a small impact from the fluted pipes, the kick factor of the harmonic cavity can be scaled from that of the main cavity as $\kappa_{\perp} \propto 1/a^3$ [222] in agreement with computed results in Table 3.2.6.

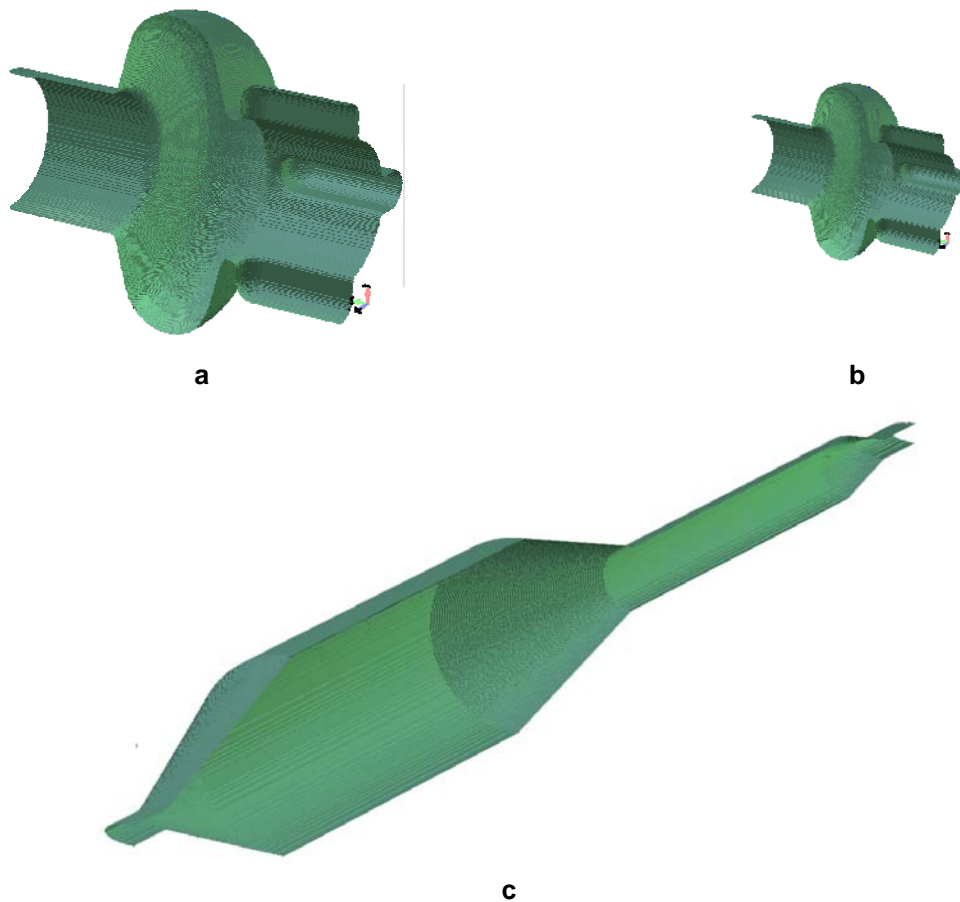


Figure 3.2.10 3D GdfidL models of the RF straight section.

a) 500 MHz main RF cavity. **b)** 1500 MHz harmonic RF cavity. **c)** Cavity transitions per straight.

Cavity transitions per straight consists of three smooth tapered transitions: regular vacuum chamber beam pipe – main cavity beam pipe, main cavity beam pipe – harmonic cavity beam pipe and harmonic cavity beam pipe – regular vacuum chamber beam pipe. Two longest tapers are taken to be 300 mm. The taper length between the beam pipe radius of the harmonic cavity (40 mm) and the regular vacuum chamber is 100 mm. For simplicity, the length of straight pipes between tapers is chosen to be 300 mm. Ferrite rings on both sides

of the RF cavities for HOM damping (narrow-band impedance) are not included in this analysis as they do not affect the short-range wakepotential (broad-band impedance).

Contribution of cavity transitions per straight to the broad-band longitudinal impedance in terms of the loss factor is significant ($\kappa_{loss}=3.5\text{V/pC}$). This value is comparable with the values for 720 m aluminum resistive wall ($\kappa_{loss}=4\text{V/pC}$) and for 200 BPMs ($\Sigma\kappa_{loss}=4\text{V/pC}$) from impedance table. Cavity itself gives a smaller contribution to the longitudinal impedance. To minimize transition impedance, taper lengths between RF cavities will be lengthened to the extent allowed by the available space.

3.2.4.3 Infrared Extraction Chamber

To take out the synchrotron radiation in far-infrared region six dipole magnets will be designed with large gap. To be able to extract the light emission ~ 50 mrad horizontal and ~ 25 mrad vertical (full radiation opening angles of the collected emission in location of the extraction mirror) within a bending magnet of $\rho=25$ m radius, the infrared (IR) chamber requires a full aperture of 67 mm vertical, 134 mm horizontal and a special trapezoidal slot extended vertically. The design of the far-IR chamber is shown in Figure 3.2.11. Since the IR-chamber has larger elliptical shape than the regular vacuum chamber (25 mm full height and 76 mm full width), smooth tapers are used to minimize the contribution to the longitudinal and transverse broad-band impedance. The IR-chamber will be installed inside of the wide-gap dipole magnet of 2.6 m long. Tapered transitions at each end of the structure, 300 mm and 100 mm long, are chosen to estimate the narrow-band impedance. They do not extend beyond the dipole magnet length and the taper length can be increased inside the dipole magnet to further reduce the broad-band impedance.

To direct the collected emission into the output port, the extraction mirror (copper color, 5 mm thick) is first modeled at the end of the trapezoid slot, 30 mm from the beam trajectory as shown in Figure 3.2.11 (zoomed part). Separation of the radiation from the electron beam is made more difficult due to the large bending radius of the NSLS-II dipoles. The mirror must be located close to the electron beam to collect the IR emission. Of particular concern is the narrow-band impedance which may be generated due to the mirror.

The narrow-band impedance computations are shown in Figure 3.2.11. The real part of the longitudinal impedance is presented for the IR-chamber with and without mirror. Set of resonant modes are generated into the chamber after the passing beam if the extraction mirror is inside. The mirror is seen by the beam and generated modes are trapped in a small pocket between the tapered transition and the mirror. These modes can cause couple bunch instability and heating of the chamber wall.

To avoid generation of resonant modes inside the chamber, we studied several variants of mirror position while maintaining the required extraction angles. One of the variants is shown in Figure 3.2.12. To avoid a pocket behind the mirror, we located the mirror at a point right after the widened cross-section had tapered back down to the regular dimensions. In this case, the extraction mirror is hidden behind the tapered transition in the region of the antechamber slot. This design eliminated the problem of resonant modes due to the mirror. It can be seen from the real part of the longitudinal impedance presented in Figure 3.2.12 (b). The narrow-band impedance of the complex IR-chamber was reduced down to the impedance of just a tapered structure.

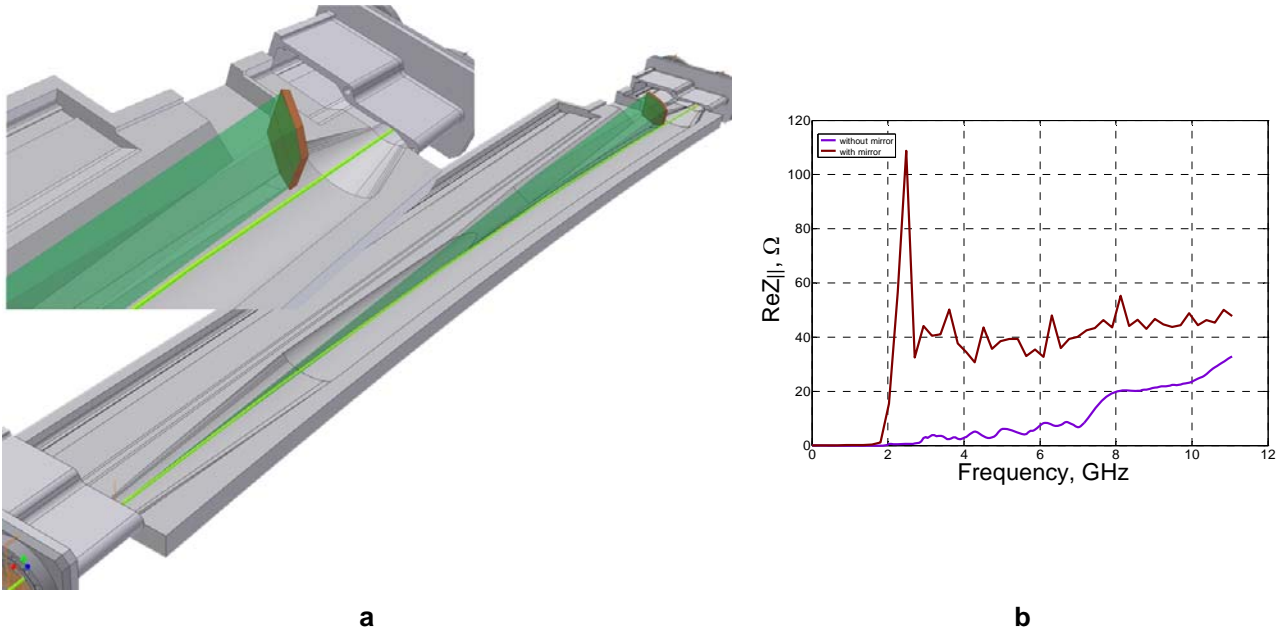


Figure 3.2.11 Infrared extraction chamber for the dipole magnet with a large gap. **a)** Design of the IR chamber with a mirror in front of the tapered transition. The green line represents the electron beam and the green shaded region represents the IR radiation. **b)** Real part of the longitudinal impedance. Wine line and the purple line are calculations with and without extraction mirror inside the chamber respectively.

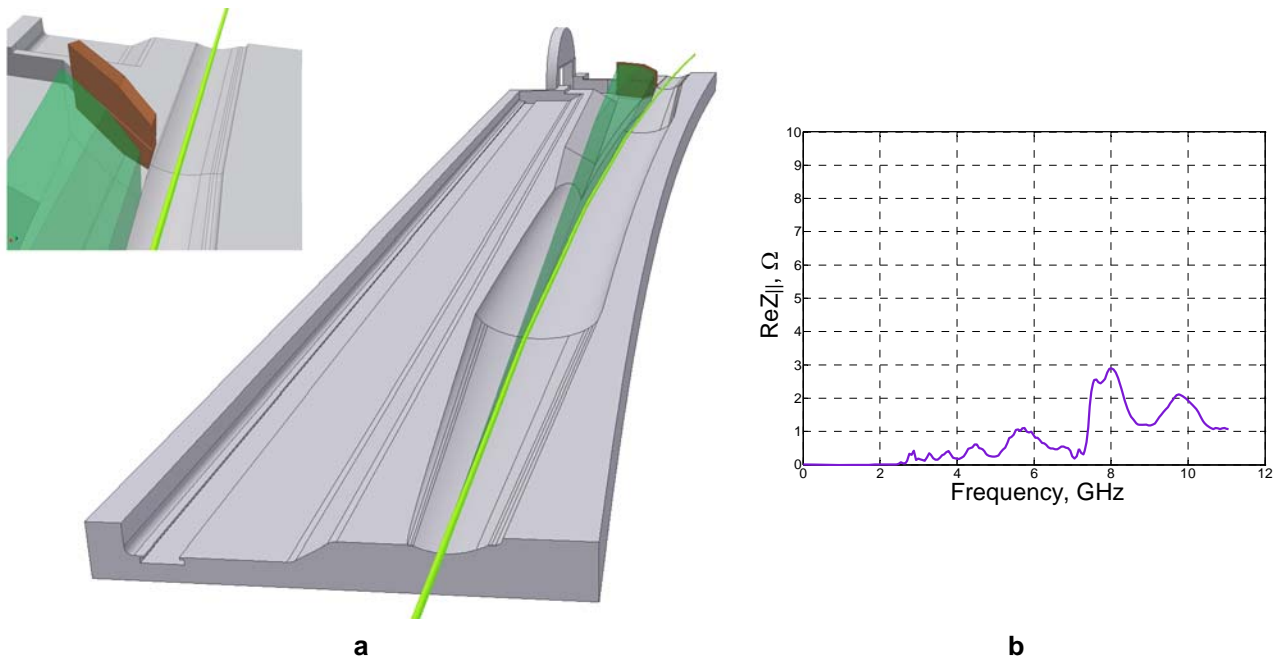


Figure 3.2.12 Design of the infrared extraction chamber with the mirror at a point right after the widened cross-section. **a)** Mirror is located inside the regular vacuum chamber behind the tapered transition. **b)** Real part of the longitudinal impedance for the current design of the IR chamber with the extraction mirror.

To estimate the short range wake (broad-band impedance) of the IR chamber, we consider a simplified model. The full height and the full width of the tapered chamber are taken the same as for the real structure, 67 mm and 134 mm, respectively. Smooth tapered transitions, each 180 mm long, are located at both ends of

the chamber. The shorter taper length here is taken for reducing computational time. We modeled narrow and trapezoid slots, where the extraction mirror will be located. The trapezoid slot extends vertically away from the structure as shown in Figure 3.2.13 (c).

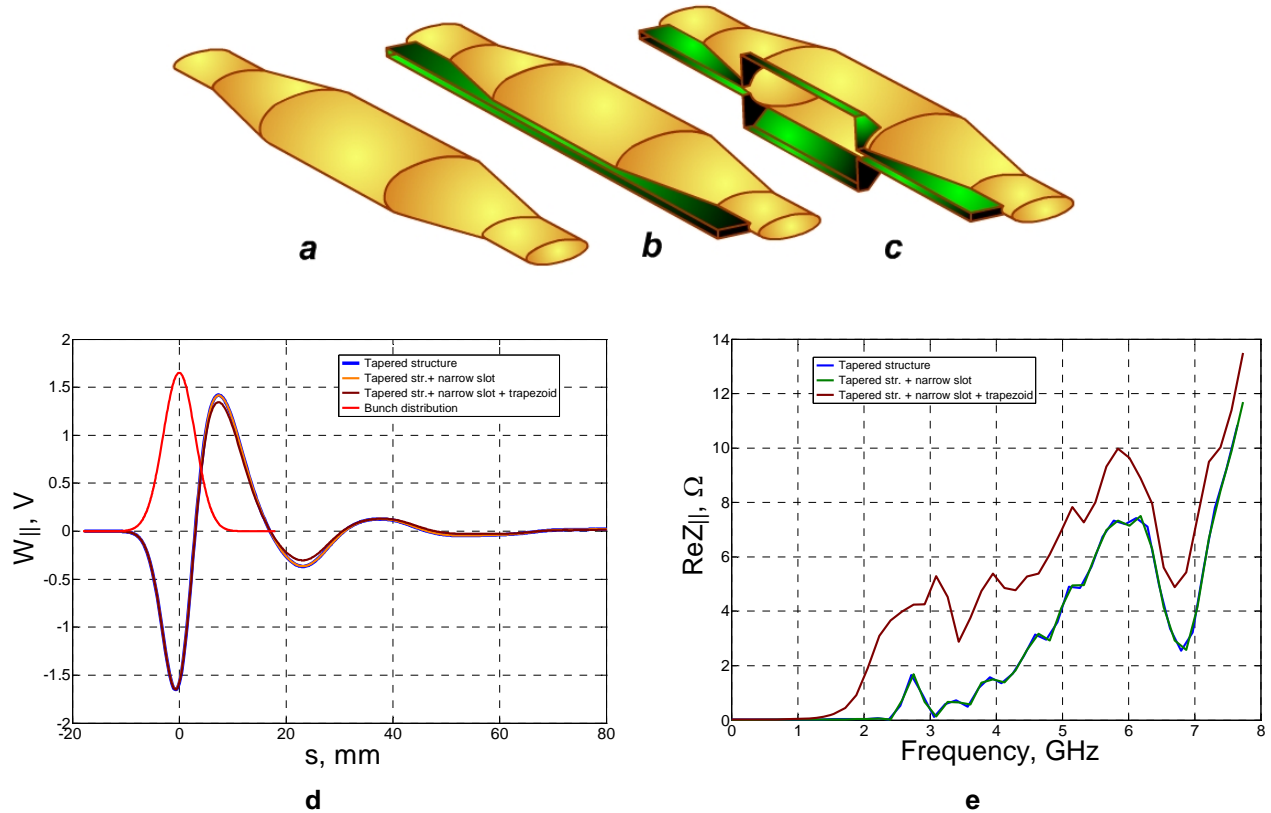


Figure 3.2.13 Simplified model of IR-extraction chamber. **a)** Tapered elliptic chamber. **b)** Tapered elliptic chamber with narrow slot. **c)** Tapered elliptic chamber with narrow slot and trapezoidal slot. **d)** The longitudinal short-range wakepotential. **e)** The real part of the longitudinal impedance.

Computations of the longitudinal wakepotential for a $\sigma_s=3$ mm rms bunch length show that narrow and trapezoid slots do not significantly affect the short-range wakepotential (Figure 3.2.13d) and hence the loss factor. The narrow-band impedance due to tapered transitions is similar to the impedance of the real geometry with the extraction mirror at the right location. The amplitude of the resonant peaks in the simplified geometry is slightly higher due to shorter taper length.

This analysis was concentrated on verifying of the results obtained for the real geometry, which is a more complex geometry and has a large value for numerical computations. As a first step we eliminated the resonant modes (narrow-band impedance) due to the extraction mirror. The next step needs to be done, to estimate the broad-band impedance for the actual design geometry. It requires a lot of computational time. In Table 3.2.6 we present the results computed for the simplified geometries shown in Figure 3.2.13. The loss factor for these geometries is $\kappa_{loss}=0.84V/pC$. Based on this preliminary study, the taper length for the actual design geometry will be increased to reduce the loss factor.

3.2.5 Intrabeam Scattering

Small-angle Coulomb scattering within a beam leads to the excitation of betatron and synchrotron oscillations of particles, which usually increases beam emittances in all phase planes. This effect, often called intra-beam scattering (IBS) or multiple Coulomb scattering, is proportional to the beam 3D phase-space density and depends strongly on beam energy, becoming more severe for high intensity, low energy machines.

When IBS is included, the steady-state beam properties with radiation damping are defined by

$$\varepsilon_x = \frac{\varepsilon_{x0}}{1 - \tau_x/T_x}, \quad \varepsilon_y = \frac{\varepsilon_{y0}}{1 - \tau_y/T_y}, \quad \sigma_p^2 = \frac{\sigma_{p0}^2}{1 - \tau_p/T_p}, \quad (3.2-28)$$

where subscript 0 indicates the beam properties in the absence of IBS, $\tau_{x,y,p}$ stand for synchrotron radiation damping times, and $T_{x,y,p}$ are the IBS growth times discussed below. These equations indicate that the IBS effect becomes important when IBS rates are significant in comparison with the radiation damping rates. Because the IBS growth times $T_{x,y,p}$ depend on beam current as well as beam emittances, energy spread, and bunch length, the above equations are coupled, and solving them requires some iterative procedure. Sometimes a fourth equation is added that expresses the current-dependent relation of the bunch length to the energy spread, to account for the potential well distortion. If the vertical emittance is dominated by weak coupling (which is our expectation for NSLS-II), the effect simplifies to 2D, and the second equation is replaced by $\varepsilon_y = \kappa \varepsilon_x$, where κ stands for the coupling coefficient.

The basic theoretical framework of IBS effect was established long ago by Piwinski [3.2.31] and Bjorken and Mtingwa (B–M) [3.2.32] using two different approaches. These theories express IBS rise times $T_{x,y,p}$ as complicated integrals of beam parameters, such as energy and phase space density, as well as lattice properties. The B–M theory has been extended to include arbitrary vertical-horizontal and vertical-longitudinal coupling [3.2.33]. The resulting growth rates are local quantities, and have to then be averaged around the lattice. Many accelerator physics codes include some variations of the B–M approach. In addition to these general procedures which are fairly computer intensive, there exist a number of more approximate formulations of IBS effect that simplify the treatment for certain parameter regimes. For example, Bane [3.2.34] has recently shown the equivalence of the Piwinski and B–M treatments in the regime applicable for high energy machines. In this regime, Bane has found that B–M results reduce to fairly compact expressions for IBS rise times, which we have found useful for NSLS-II.

The IBS approaches mentioned above result in growth times proportional to the so-called Coulomb log factor, equal to $\ln(b_{\max}/b_{\min})$, where $b_{\max, \min}$ are impact parameters, which are not well defined. Often, b_{\max} is taken equal to σ_y . To fix b_{\min} , a so-called “tail-cut” procedure was suggested by Raubenheimer [3.2.35]. He pointed out that, since IBS results in non-Gaussian beam distributions, tail particles could be overemphasized; therefore, one must chose b_{\min} to eliminate interactions having collision rates smaller than SR damping rates.

The NSLS-II emittance is strongly dominated by the IDs and damping wigglers. Rather than assuming some fixed ID makeup, we have calculated IBS effects as a function of radiation losses in the machine, having ε_{x0} vary from the ~ 2 nm bare lattice value down to about 0.4 nm. The zero-current vertical emittance ε_{y0} was fixed at the diffraction limit for 1 Å x-rays (8 pm-rad), corresponding to κ varying from $\sim 0.5\%$ for bare lattice to about 2% for $\varepsilon_{x0} = 0.4$ nm.

Most NSLS-II calculations have been performed with the code ZAP [3.2.20], which implements the 2D procedure of the B–M theory [3.2.32], i.e., the vertical emittance is assumed dominated by coupling. We used 500 mA for the total ring current, and assumed it uniformly distributed into 80% of the 500 MHz RF buckets. As we changed the amount of radiation losses, the RF voltage was adjusted to keep the RF energy acceptance constant at 3%. Electron beam parameters in the absence of IBS, used as input to ZAP (such as horizontal

emittance, energy spread, bunch length, and radiation damping times) were calculated analytically by scaling bare lattice values by the amount of radiation losses. The results given by ZAP are shown in Figure 3.2.14.

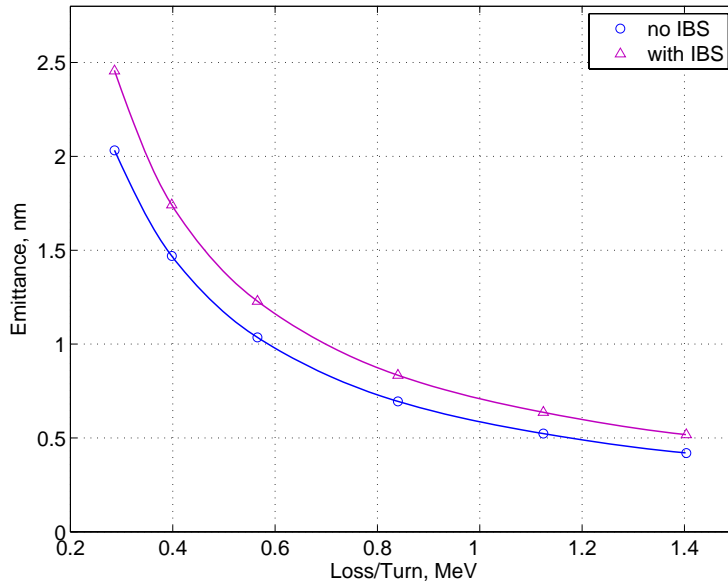


Figure 3.2.14 Horizontal emittance vs. total SR loss.

Note that the IBS-induced relative emittance blow-up does not exceed 20%, and remains fairly independent of the amount of radiation losses (and hence the emittance). This implies that for smaller emittances, increased IBS rates due to denser bunches are offset by the increase in radiation damping. This is quite contrary to a more typical situation in a storage ring light source not dominated by IDs, where decreasing the emittance by adjusting the lattice (and hence keeping the SR rates fixed) can result in an increase of IBS-induced emittance blow-up. We have also found that the IBS rise times calculated by ZAP are in reasonable agreement (better than 50 %) with the estimates we have done using Bane's formalism.

Note that the results presented in Figure 3.2.14 are based on several conservative assumptions. First, calculations are performed at zero-current bunch length, while in reality the bunch will be longer, due to potential well distortion and the harmonic RF system. At even higher single-bunch currents, used in special operating modes, the microwave instability will result in an even stronger increase in bunch length as well as energy spread, reducing the IBS effect further. In addition, the calculations of Coulomb log that are used in ZAP use $b_{\max} = \sigma_x$ and do not include the tail-cut procedure. As a result, the Coulomb log value ZAP assumes for NSLS-II parameters is about 17, while more recent estimates [3.2.33] that include the cut would reduce it to about 10.

We have also done some cross-checks of the bare lattice case using the SAD code from KEK [3.2.36]. SAD has been extensively benchmarked against the experimental results from the ultra-low emittance ATF storage ring. SAD does include the tail-cut, so it results in smaller IBS induced blow-up compared to ZAP. However, when scaled for the Coulomb log, the codes are in good agreement. SAD allows for full 3D treatment of IBS and will be used in the future to study the effects of vertical dispersion for NSLS-II.

To summarize, our calculations to date indicate that under pessimistic assumptions, IBS-induced relative emittance blow-up for NSLS-II should not exceed 20% at nominal bunch intensity and therefore it should not present a problem. Furthermore, we have found the magnitude of the blow-up to be fairly independent of the NSLS-II emittance, since the increased IBS rates for denser bunches are compensated by faster radiation damping. Future studies will include accounting for a more comprehensive ID makeup, considering the effects of vertical dispersion, and further developing some models of bunch lengthening.

3.2.6 Touschek Lifetime

The beam lifetime in most modern synchrotron radiation sources is limited by the Touschek effect, which describes the collision of two electrons inside a bunch, leading to momentum transfer from the transverse (usually horizontal) plane into the longitudinal direction. If the resulting longitudinal momentum exceeds the momentum acceptance of the accelerator, these particles are lost.

The Touschek lifetime is calculated as [3.2.37],

$$\frac{1}{\tau} = \frac{r_e^2 c q}{8\pi e \gamma^3 \sigma_s} \cdot \frac{1}{C} \cdot \oint_C \frac{F((\delta_{acc}(s) / \gamma \sigma_{x'}(s))^2)}{\sigma_x(s) \sigma_{x'}(s) \sigma_y(s) \delta_{acc}^2(s)} ds, \quad (3.2-29)$$

where r_e denotes the classical electron radius, q the bunch charge, σ_s the RMS bunch length, C the circumference of the storage ring, and $\sigma_x(s)$ and $\sigma_y(s)$ the RMS horizontal and vertical beam radii, including the dispersion term.

$$\sigma_{x'}(s) = \frac{\varepsilon_x}{\sigma_x(s)} \sqrt{1 + \frac{H(s) \sigma_\delta^2}{\varepsilon_x}} \quad (3.2-30)$$

is the RMS beam divergence for $\alpha_x = 0$, with

$$H(s) = \gamma_x \eta^2 + 2\alpha_x \eta \eta' + \beta_x \eta'^2 \quad (3.2-31)$$

the chromatic invariant. The function $F(x)$ is defined as

$$F(x) = \int_0^1 \left(\frac{2}{u} - \ln \frac{1}{u} - 2 \right) \cdot \exp(-x/u) du. \quad (3.2-32)$$

While the Touschek lifetime depends linearly on the bunch length as well as on the vertical beamsize, its dependence on the horizontal beamsize (or emittance) is more complicated. For large horizontal beamsize, the particle density of the bunch becomes very small, thus greatly decreasing the probability of two electrons colliding. On the other hand, a large horizontal emittance results in large horizontal momenta that can be transferred into the longitudinal plane due to a Touschek scattering event. The dependence of the resulting Touschek lifetime (for a bunch length of 4.5 mm) on horizontal emittance is illustrated in Figure 3.2.15. The result is that in the region of the design emittance for NSLS-II, the Touschek lifetime is not particularly sensitive to emittance. For a variety of reasons we will discuss, this estimate of Touschek lifetime is optimistic. Even so, for the design emittance, the lifetime is below the specified lifetime of 3 hours. Increasing the bunch length with a Landau cavity can provide the extra lifetime to meet the lifetime goal.

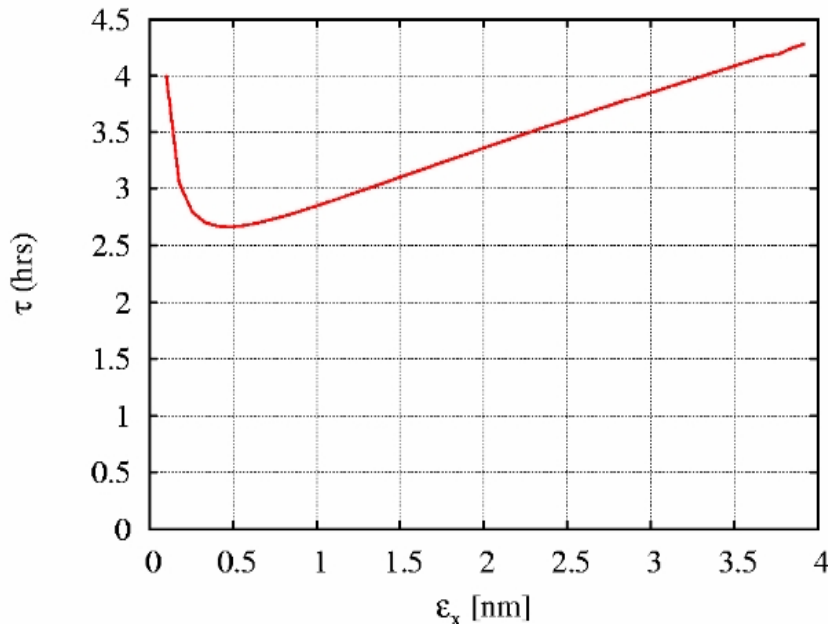


Figure 3.2.15 Tauschek lifetime vs. horizontal emittance for 3% momentum acceptance and a 4.5 mm bunch length.

Experience at facilities like ALS and SLS has shown that nonlinear betatron coupling plays a significant role in limiting the momentum acceptance of the storage ring, especially in the presence of small vertical apertures due to small-gap insertion devices. Therefore, tracking has been performed using the TRACY-2 code. Since Tauschek scattering occurs near the center of the bunch, the momentum acceptance δ_{acc} needs to be determined for particles starting at a longitudinal position s with coordinates $x = x' = y = y' = 0$. In general, this yields different momentum acceptances δ_{acc}^+ for positive and δ_{acc}^- for negative momenta, resulting in different Tauschek lifetimes τ^+ and τ^- . Based on these two results, the total Tauschek lifetime τ_{tot} is computed as

$$\frac{1}{\tau_{tot}} = \frac{1}{2} \cdot \left(\frac{1}{\tau^+} + \frac{1}{\tau^-} \right). \quad (3.2-33)$$

The RF acceptance has been set to $\pm 3\%$. To achieve this for the bare lattice, an RF voltage of 2.5 MV is required. For the baseline case of 3 damping wigglers, a voltage of 3.1 MV is required. The RF acceptance determines the maximum achievable momentum acceptance. In fact there are a number of factors that can reduce the true momentum acceptance. Off-momentum particles below the RF acceptance can hit apertures that an on-momentum particle would not hit. This is due to the fact that off-momentum particles have a different orbit (from dispersion), and different tunes (from chromaticity). Further, as a particle executes damped synchrotron oscillations, it will sample a large region of phase space and tune space which can lead to the loss of the particle. The calculations shown here use 512 turns, or several synchrotron oscillations. Tracking for a full damping time (~ 4500 turns for 3 damping wigglers) should be performed to spot-check results. We have found that in some cases, this extra tracking time can decrease the momentum acceptance, and hence lifetime. In one case (very similar to the nominal case we present here), we found that the lifetime dropped from 2.5 hours to 2.2 hours when the number of turns was increased from 512 to 5000.

To get a realistic estimate of the momentum acceptance, a realistic lattice model is created from the design lattice and relevant non-linearities plus appropriate physical apertures are included. The lattice is non-linear due to the sextupoles, insertion devices and random and systematic higher order multipole errors. These are discussed further in the section on dynamic aperture. Here, we have taken the bare lattice and added 3 damping wigglers and 3 CPMUs, plus random and systematic multipole errors. The damping wigglers, in

addition, have higher harmonic content determined by fitting computed field maps to a Halbach basis. The systematic multipole errors come from modeling and measurements of quadrupoles and sextupoles borrowed from the SLS which are similar to our design magnets. The random errors come from measured values for the SLS magnets produced by the Budker Institute in Novosibirsk. The ID parameters used were as follows: for the damping wiggler, the peak field is 1.8 T, and the period length 9 cm, with 77 periods. For the CPMUs, the peak field is 1.2 T, and the period length 19 mm, with 160 periods.

Random misalignment and roll errors are added, including the systematic effects from the girders. The girders are misaligned randomly by 100 μ , and quadrupoles and sextupoles misaligned by 30 μ relative to the girder. The orbit is corrected by computing the beam response matrix and adjusting the corrector strengths to minimize orbit offset at the BPMs. In addition, we must correct the linear optics due to the perturbation caused by the damping wigglers. For these studies, the three damping wigglers were assumed to occur consecutively. Periodic distribution should also be considered.

The vertical emittance is determined by a combination of linear coupling and vertical dispersion. The random roll errors of 0.2 mrad for the quadrupoles and sextupoles and 0.5 mrad girder to girder cause coupling, but the equilibrium vertical emittance is still below the diffraction limited value of 8 pm ($\epsilon_y = 1$ pm for the case used for the calculations of energy acceptance). An algorithm to increase vertical dispersion combined with coupling control/correction has been developed to control vertical emittance. The algorithm has been tested but is not included in these calculations. A vertical emittance of 8 pm is assumed here for the lifetime calculation.

After preparing the lattice by adding all the above errors, corrections and physical apertures (described below), the momentum acceptance around the ring is computed by tracking. The result for the nominal case is shown in Figure 3.2.16 (a). We see that the errors and apertures have not had a large impact and the lifetime has only dropped from 2.77 hours to 2.62 hours. Adding more insertion devices adds to the non-linearity and is expected to have an impact on momentum aperture.

As we have mentioned, beam loss can occur due to electrons hitting transverse physical apertures. Both vertical and horizontal apertures can decrease lifetime. First consider the horizontal case. A Touschek scatter in a dispersive region causes betatron oscillations throughout the ring. Considering uncoupled linear betatron dynamics, the amplitude of such oscillations is given by

$$x(s) = (\eta + \sqrt{H_0\beta_x})\delta \quad (3.2-34)$$

with H_0 the dispersion invariant (3.2-31) at the position of the scatter, and δ the resultant relative energy change of the particle. The maximum value is approximately twice the maximum dispersion times δ . For δ of 3% this can be as large as 27 mm. Figure 3.2.16 (b) shows the effect on lifetime of varying the horizontal aperture in the maximum dispersion region. We see that below 27 mm, the lifetime decreases. This shows the importance of maintaining the stay-clear aperture. Photon absorbers are one example of elements for which it would otherwise be desirable to be closer to the beam than the stay-clear specifications.

If we expect such large horizontal betatron oscillations to be stable, then clearly any coupling will cause vertical apertures to be a concern. The smallest vertical aperture is that of the CPMU gap of ± 2.5 mm. We have varied this gap size and computed the effect on the lifetime in Figure 3.2.16 (c). Below the nominal value of ± 2.5 mm, we see a decrease in lifetime.

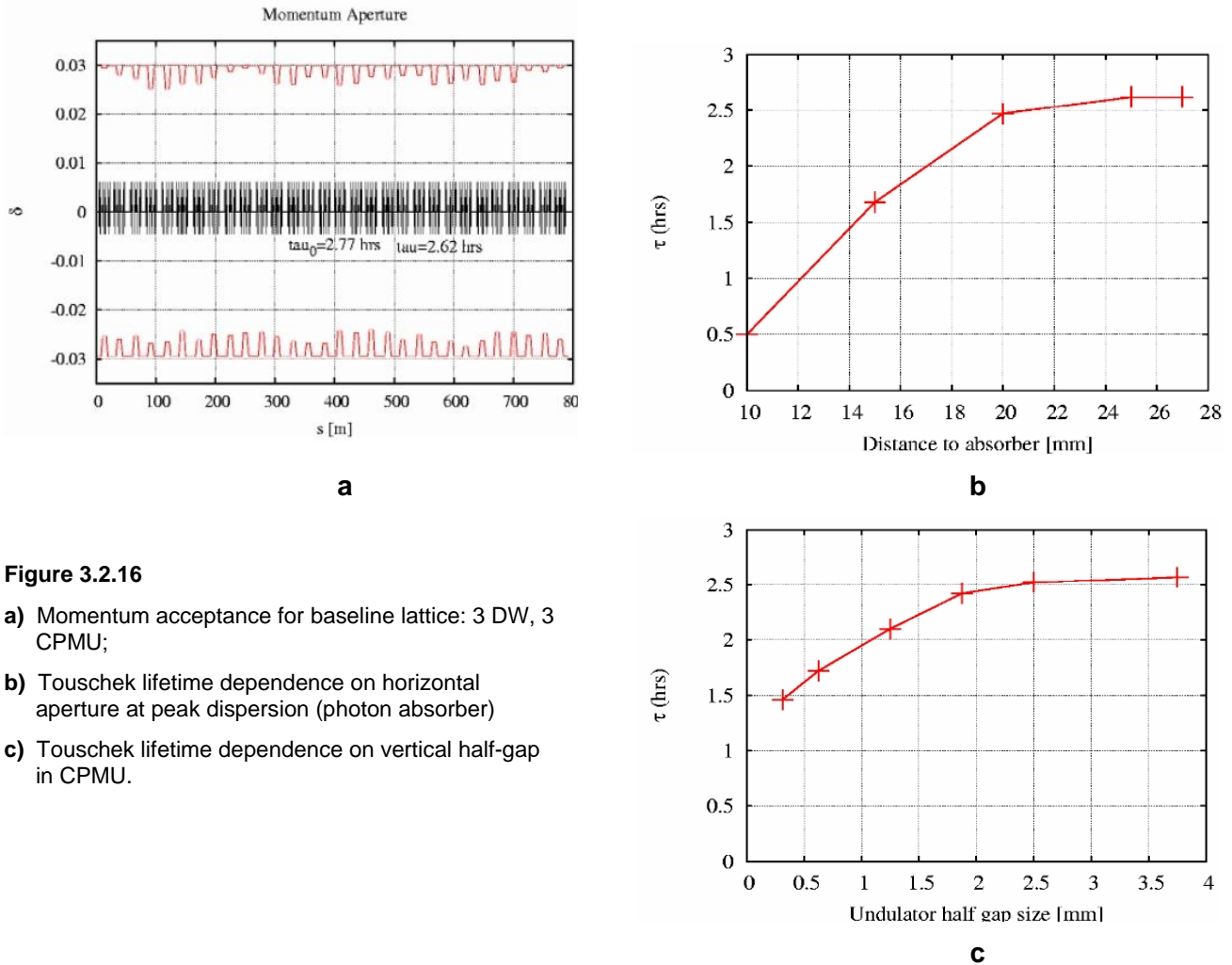


Figure 3.2.16

- a) Momentum acceptance for baseline lattice: 3 DW, 3 CPMU;
- b) Touschek lifetime dependence on horizontal aperture at peak dispersion (photon absorber)
- c) Touschek lifetime dependence on vertical half-gap in CPMU.

In conclusion, a realistic storage ring model is required to estimate the Touschek lifetime, particularly in order to compute the momentum acceptance. We are developing such a realistic model to be used together with dynamic aperture calculations to analyze limits on stay-clear apertures, magnetic and alignment imperfections, and other machine parameters such as chromaticity. Such studies are ongoing and must be continually updated as the sextupole settings and tunes continue to be optimized and the lattice design continues to mature. Further effects to be explored are the impact from additional insertion devices, especially from EPU's. Also, we will study more realistic ID modeling, inclusion of the dispersion wave to get a self-consistent model, and required stay-clear apertures. We also plan comprehensive studies including multiple seeds for the random errors. Finally, we emphasize that even if the momentum acceptance of 3% is achieved, we still require the bunch lengthening effect from the Landau cavity in order to achieve a Touschek lifetime of 3 hours.

3.2.7 Landau Cavity

Let us begin by reviewing the operation of a higher-harmonic, bunch-lengthening cavity (HHC) [3.2.38]. The fundamental cavity operates at an angular frequency, $\omega_{rf} = h\omega_0$, where h is an integer and $\omega_0 = 2\pi/T_0$ is the angular frequency of revolution. Assuming the Landau cavity is operating at the n^{th} harmonic of the frequency of the fundamental RF, the voltage seen by an electron with temporal deviation τ is

$$V(\tau) = V_0 \left[\sin(\omega_{rf}\tau + \phi_s) + \kappa \sin(n\omega_{rf}\tau + \phi_n) \right]. \quad (3.2-34)$$

In the ideal operation of such a cavity, one chooses to satisfy the conditions

$$\begin{aligned} U_0 &= V_0 [\sin \phi_s + \kappa \sin \phi_n] \\ 0 &= \cos \phi_s + n\kappa \cos \phi_n \\ 0 &= \sin \phi_s + n^2 \kappa \sin \phi_n, \end{aligned} \quad (3.2-35)$$

where energy loss (U_0) and gain are balanced, and the first and second derivatives of the waveform are set to zero, at zero phase. In this case, the voltage has the form

$$V(\tau) = \cos \phi_s \left(\sin \omega_{rf}\tau - \frac{1}{n} \sin n\omega_{rf}\tau \right) + \sin \phi_s \left(\cos \omega_{rf}\tau - \frac{1}{n^2} \cos n\omega_{rf}\tau \right). \quad (3.2-36)$$

Approximating this for small τ yields the cubic form

$$V(\tau) \cong \cos \phi_s \left(\frac{n^2 - 1}{6} \right) (\omega_{rf}\tau)^3 + \sin \phi_s \left(1 - \frac{1}{n^2} \right). \quad (3.2-37)$$

As we will operate the Landau cavity passively, i.e., powered only by the beam, we cannot satisfy all of the ideal conditions. A superconducting cavity, in particular, absorbs very little power, implying that ϕ_n is fixed at $-\pi/2$, a few degrees from the ideal phase. Fortunately, this phase shift has little impact on the bunch profile. Figure 3.2.17 shows an unstretched bunch (blue) plotted with a stretched bunch (red) in a uniform fill with HHC detuning at +82 kHz.

A third-harmonic Landau cavity can be used to increase the electron bunch length without increasing the energy spread. This increases the Touschek lifetime and reduces the effect of intrabeam scattering on emittance. The nonlinear voltage resulting from the use of a Landau cavity results in a large increase in the dependence of the synchrotron tune on the amplitude of synchrotron oscillations. Energy transfer from potentially unstable resonant particles within a bunch to the surrounding non-resonant particles often provides a powerful mechanism for the suppression (Landau damping) of longitudinal coupled-bunch dipole modes. Also, the increase of bunch length can increase the stabilizing effect of positive chromaticity on the transverse dipole oscillations. The increased synchrotron tune spread can also help stabilize the higher-order head-tail modes.

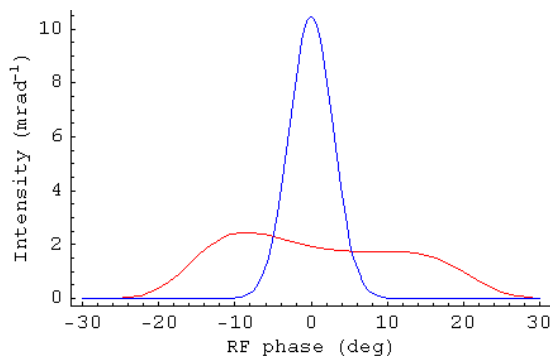


Figure 3.2.17 An unstretched bunch (blue) plotted with a stretched bunch (red) in a uniform fill with HHC detuning at +80 kHz. The bunch lengths are 14.1 and 56.1 ps, respectively.

If, as expected, there is a gap in the fill for ion clearing, then there will be a periodic transient induced in the cavity fields, causing non-uniform bunch profiles across the bunch train [3.2.39, 3.2.40, 3.2.41]. This effect is proportional to the R/Q s of the cavities, which favors superconducting cavities due both to their lower R/Q and their higher sustainable fields (requiring fewer cavities). Away from the center of the bunch train, bunches are much shorter and are peaked near the local synchronous phase, which can be a distance from the center of the nominal bucket. These peripheral bunches have shorter Touschek lifetime. This effect was found at ALS [3.2.40] to significantly reduce the overall lifetime of the beam. Figure 3.2.18 shows the bunch profiles for a 90% fill pattern, harmonic-cavity detuning of +80 kHz, and a single gap, and with the gap split into four symmetrically spaced gaps.

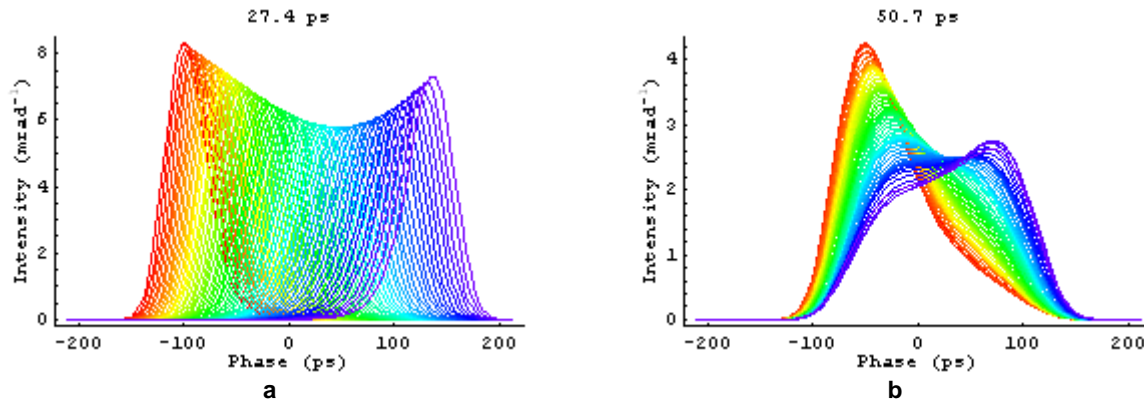


Figure 3.2.18 Bunch profiles along the bunch train for a 90% fill fraction, harmonic-cavity detuning of +80 kHz, and a) a single gap in the train, and b) four gaps in the train. Each plot is labeled with the average RMS bunch length of the bunches. For reference, the unstretched bunch length is 14.1 ps and the stretched bunch length in a uniform fill is 56.1 ps.

With a single ion-clearing gap, the transient is severe, even with SC cavities (Figure 3.2.18a). The bunches are dispersed in phase with only modest stretching, reducing the field the beam is able to drive in the HHCs. The increase in bunch length is less than a factor of two. In this large ring, reducing the HHC detuning to bring up the field tends to increase the dispersion before increasing the field and stretching individual bunches. But breaking up the gap into several smaller gaps makes the ring appear to the cavities to be a smaller and is effective at increasing the average bunch length. In the case of four gaps, the increase in bunch length is by a factor of 3.6. The profiles of Figure 3.2.18b with four gaps appear similar to the bunch profiles measured at ELETTRA [3.2.42], which is one-third the size of NSLS-II. With an 80% fill fraction, the bunches are even shorter (Figure 3.2.19). Bunch lengths vary smoothly with increasing fill fraction to the 56.1-ns length at a 100% fill. Smaller fill fractions aggravate the variation of bunch shapes along the train.

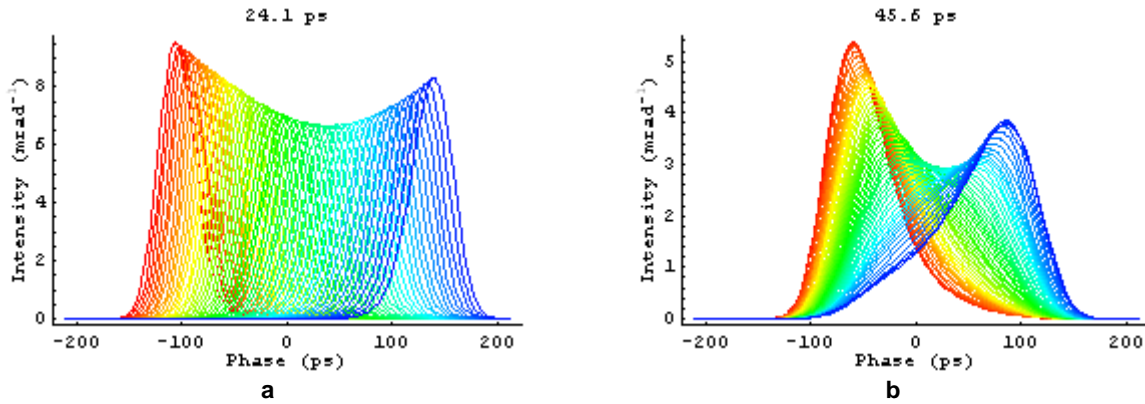


Figure 3.2.19 Bunch profiles along the bunch train for a 80% fill fraction, harmonic-cavity detuning of +80 kHz, and a) a single gap in the train, and b) four gaps in the train. Each plot is labeled with the average RMS bunch length of the bunches. For reference, the unstretched bunch length in a uniform fill is 14.1 ps and the stretched bunch length in a uniform fill is 56.1 ps.

Bunch lengths vary with position along the train, and tend to be greatest near the center. In Figure 3.2.20a, each trace corresponds to a particular cavity field set by the detuning, which is from +110 (violet) to 70 (red) kHz. As HHC fields increase, bunch lengths and lifetimes tend to increase; but bunches that become double peaked, however, can show large RMS bunch length but reduced lifetime. Bunch centroid phases (arrival times) also vary with position along the train. In Figure 3.2.20b, the phase along the train is plotted for a 90% fill and the same fields as in Figure 3.2.20a. The synchronous phase is a sensitive function of local shifts in the RF wave due to the $(\omega_{rf})^3$ inflection; that sensitivity increases with increasing HHC field, even beyond the optimal HHC field.

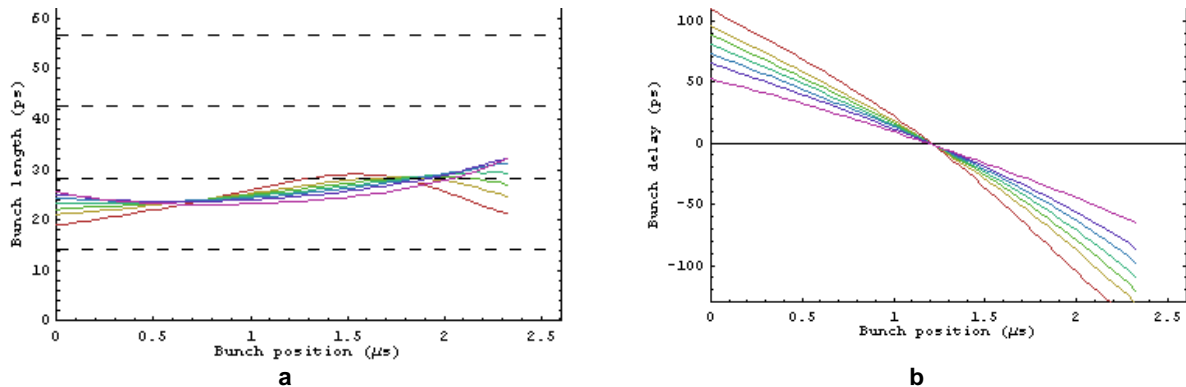


Figure 3.2.20 Bunch lengths a) and delays b) along the bunch train for a 90% fill and a single gap. Each trace corresponds to a particular cavity detuning: +110 (violet), 100, 95, 90, 85, 80, and 70 kHz (red). In a), the dashed lines are drawn at multiples of the unstretched bunch length.

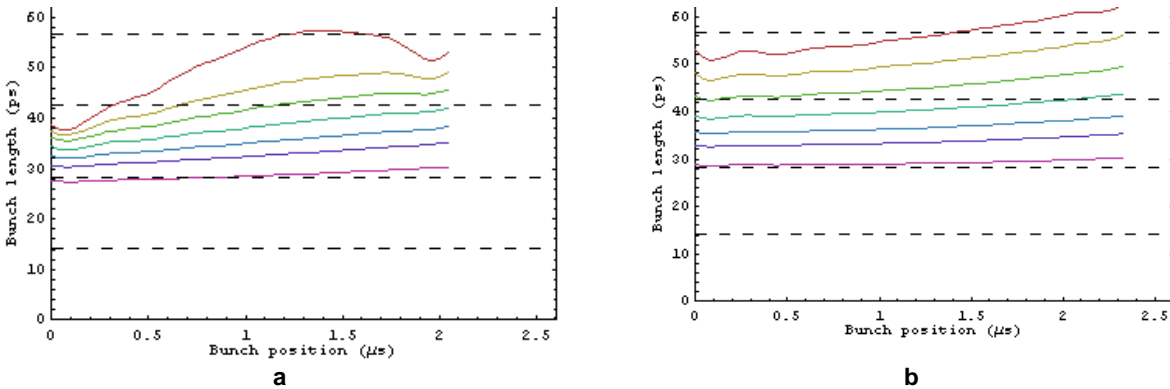


Figure 3.2.21 Bunch lengths along the bunch train with four gaps in an **a)** 80% fill, and **b)** 90% fill. Each trace corresponds to a particular cavity detuning: in **a)**, +110 (violet), 100, 95, 90, 85, 80, and 70 kHz (red), and in **b)**, +110 (violet), 100, 95, 90, 85, 80, and 75 kHz (red). The dashed lines are drawn at multiples of the unstretched bunch length.

The HHC field required for nominal bunch stretching is 1.5 MV. Since the maximum sustained fields reached in HHCs developed to date are 0.5 MV per cell in 1500 MHz cavities, three cells are required, either in three single-cell cavities, or two double-cell cavities. The performance plots above were computed assuming four cells, perhaps in two cryostats. In practice, significantly longer lifetimes are achievable by operating the HHCs at fields slightly higher than the ideal described above, as the NSLS VUV ring is operated now. The useful fields are limited by the onset of higher-order longitudinal instabilities.

The Day-1 configuration employs a reduced number of damping wigglers and consequently requires less main- and harmonic-cavity fields. Since two harmonic-cavity cells are capable of providing 1.0 MV of the 1.1 MV nominally required during this phase, most of the benefit of the HHC is obtained from this one cavity. Since the impedance is only that of two main and two HHC cells, the impact of the bunch train on bunch profiles is reduced in proportion.

Compressed bunch operation for timing experiments is possible by detuning the HHC below the RF harmonic, instead of above. The bunch length at small single-bunch currents is reduced to less than half the bunch length without a harmonic cavity. But at finite currents, potential-well distortion by the ring's broadband impedance, and microwave instability, if present, inevitably increases the bunch lengths. The short bunch lengths may also permit higher-frequency, higher-order modes in the HHC and elsewhere to drive coupled-bunch instabilities. Short-bunch operation may drive the need for longitudinal feedback.

The potential for unstable coupled-bunch modes driven by the CESR-B SC cavity in unstretched bunches was investigated in Section 3.2.3.4. In stretched bunches, Landau damping is expected to provide additional damping. This was confirmed in Vlasov simulations of stretched bunches assuming an RF potential well giving the stretched bunch of Figure 3.2.17. In each run, bunches was simulated with a single HOM present, up to 6.3 GHz, and its threshold for instability in terms of impedance determined. At all frequencies, thresholds at least a few times higher than that given in Eq. 3.2-27 were determined. Results are shown in Figure 3.2.22.

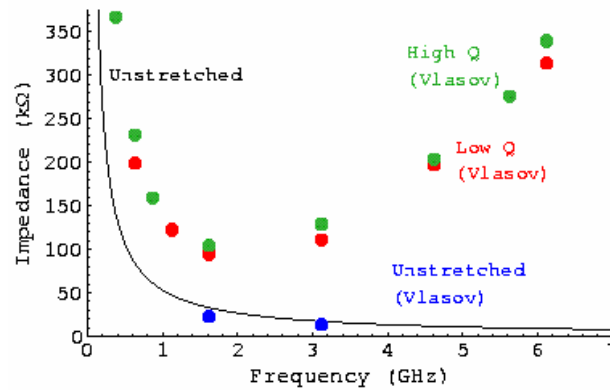


Figure 3.2.22 Instability thresholds (at 500 ma) for coupled-bunch modes in a stretched bunch expressed in terms of impedance, for a high-Q-model HOM impedance (green points) and lower-Q-model HOM impedance (red points), in the phase-four commissioning phase of the machine. The solid line is from Eq. 3.2-27, and blue points are test Vlasov runs with unstretched bunches. Thresholds were determined by Vlasov simulations.

It is useful to construct linear time-independent models of the RF system and beam, which are then plugged into comprehensive models of the RF system and used to search for unanticipated behaviors [3.2.43]. Linear models are also useful for determining RF-system specifications, such as amplifier noise specifications, from beam-based noise specifications. But the stretched bunches of NSLS-II have a multiplicity of active degrees of freedom that shape their small-signal behavior as they interact with the rf system, and the Pedersen model [3.4.44] is not adequate to model them. As an alternative, computer simulations may be used to determine beam behavior, which is realistic to the degree to which the computer model captures the physics of the beams.

In this spirit, Vlasov simulations were used to determine impulse response functions, which were then Fourier transformed to their frequency-domain representations. The beam phase response to amplitude and phase modulation of the rf, which is the motion of the bunch centroid phase in response to excitation of the RF intensity and phase, is shown in Figure 3.2.23. Although only the beam phase response is shown, beam energy, main-cavity amplitude and phase, and HHC amplitude and phase responses are also determined by a single set of simulations. Very precise rational-function fits have been obtained using MATLAB's signal processing toolbox.

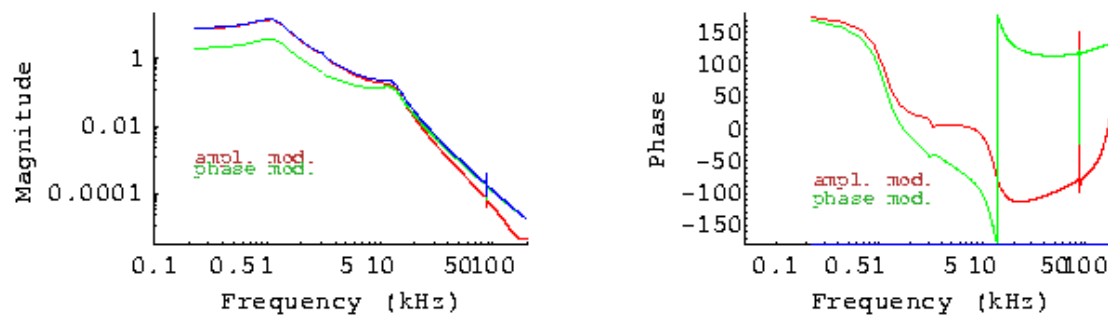


Figure 3.2.23 Beam-phase response functions to amplitude and phase modulation. Red traces are for amplitude modulation, green traces for phase modulation, and blue traces for the root square sum of the two. The left plot shows the amplitudes of the response functions, and right plots show the phases. There are four main cavities, four HHCs, HHC detuning is -4 kHz, and the loaded Q of the main cavities is set to 90 k.

There is considerable structure in these response functions starting at about 1 kHz that suggests that the problem of designing an RF controller capable of suppressing noise at significant bandwidth will be difficult. It is hoped that detailed rational-function and RF system models will provide some guidance in this area.

NSLS-II can opt to use an active HHC, i.e., HHCs that are powered by conventional amplifiers, such as was done in the NSLS VUV ring. In this configuration, resistive and reactive power are applied to control the phase of the cavity relative to the beam, almost arbitrarily. But the numerical results presented above, and the example of the VUV ring, which uses an active system to set the cavity (a NC cavity) phase to -90 degrees, show that the impact of the difference between -90 degrees and the nominal phase for stretching, even in the uniform-fill case, is insignificant. And in a fill with a significant gap, the improvement in the profiles is swamped by the effect of the periodic transient. Furthermore, an active system would require development of a cavity with an input coupler, could introduce multipacting, and could complicate HOM suppression. For these reasons, a passive cavity has been selected for NSLS-II.

3.2.8 Conclusions

Using a simplified model of the storage ring impedance, we have estimated the instability thresholds for NSLS-II. The longitudinal motion is found to be stable. At zero chromaticity, the transverse resistive wall impedance will make the beam unstable at 15 mA average current. According to simulations, increasing the chromaticity above 4 should provide stability. However, there is concern about the effect on DA at higher chromaticity; therefore, we will also use a transverse feedback system.

We have made significant progress in calculating the impedance of the storage ring using GdfidL. The results obtained thus far are within the envelope of the model we have used to estimate thresholds. Thus, we believe our model is conservative. We plan to complete the calculation of the storage ring impedance and then use the numerically determined wakefields in a tracking code to determine the instability thresholds.

Calculations indicate that the increase of emittance due to intrabeam scattering should be less than 20%. For the present state of the lattice design, the 5 mm full vertical aperture of the in-vacuum undulators reduces the energy acceptance from 3% down to 1.5% at large-dispersion locations. This results in a Touschek lifetime of 2 hrs. We plan to investigate whether further optimization of the working point can reduce the nonlinear coupling and thus increase the Touschek lifetime. Use of a Landau third-harmonic bunch lengthening cavity is planned. This will reduce the effect of intrabeam scattering on the emittance, lengthen the Touschek lifetime to more than 3 hrs, and provide enhanced longitudinal and transverse stability.

References

- [3.2.1] A.W. Chao, *Physics of Collective Beam Instabilities in High Energy Accelerators* (Wiley, NY, 1993).
- [3.2.2] See, e.g., K. Harkay, R. Nagaoka, J.L. Revol, and T. Nakamura, "A Preliminary Comparison of Beam Instabilities among ESRF, APS, and SPrinG-8 X-Ray Storage Ring Light Sources, Proc. EPAC2002, 1505 (2002).
- [3.2.3] W. Bruns, <http://www.gdfidl.de>.
- [3.2.4] G.V. Stupakov, "Wake and Impedance," SLAC-PUB-8683 (2000).
- [3.2.5] B. Zotter and S.A. Kheifets, *Impedances and Wakes in High-Energy Particle Accelerators* (World Scientific Publishing Co., Singapore, 1998).
- [3.2.6] A. Chao, S. Heifets, and B. Zotter, "Tune Shifts of Bunch Trains due to Vacuum Chambers Without Circular Symmetry," *Phys. Rev. ST-AB* **5**, 111001 (2002).
- [3.2.7] K. Bane, and M. Sands, "Short-Range Resistive Wall Wakefields," AIP Conf. Proc. **367**, 131 (1995).
- [3.2.8] B. Podobedov, "Extreme Anomalous Skin Effect Wakefields," unpublished.

- [3.2.9] Y.C. Chae, “The Impedance Database and its Applications to the APS Storage Ring,” Proc. PAC2005, 3017.
- [3.2.10] See, e.g., S. Krinsky, “Simulation of Transverse Instabilities in the NSLS-II Storage Ring,” BNL-75019-2005-IR.
- [3.2.11] J. Haissinski, *Il Nuovo Cimento* **18**, 72 (1973).
- [3.2.12] K. Oide and K. Yokoya, “Longitudinal Single-Bunch Instability in Electron Storage Ring,” KEK Preprint 90-10 (1990).
- [3.2.13] M. Borland, ELEGANT,
http://www.aps.anl.gov/Accelerator_Systems_Division/Operations_Analysis/software.shtml
- [3.2.14] D. Boussard, CERN LABII/RF/INT/75-2 (1975).
- [3.2.15] M. Blaskiewicz, “The TRANFT User’s Manual,” unpublished.
- [3.2.16] J. Kirchgessner, *Part. Accel.* **46**, 151 (1995).
- [3.2.17] M. de Jong et al., *J. Microwave Power Electromagnetic Energy* **27**, 136 (1992).
- [3.2.18] K. Halbach and R.F. Holsinger, “SUPERFISH-A Computer Program for Evaluation of RF Cavities with Cylindrical Symmetry,” *Part. Accel.* **7**, 213 (1976).
- [3.2.19] Mark deJong, private communication.
- [3.2.20] M.S. Zisman, S. Chattopadhyay, and J.J. Bisognano, “ZAP User’s Manual,” LBL-21270, UC-28 (1986), 168.
- [3.2.21] R. Nagaoka, “Numerical Evaluation of Geometric Impedance for SOLEIL,” Proc. EPAC2004, 2038.
- [3.2.22] K. Yokoya, “Resistive Wall Impedance of Beam Pipes of General Cross Section,” *Part. Accel.* **41**, 221 (1993).
- [3.2.23] G. Stupakov, “Coupling Impedance of a Long Slot and an Array of Slots in a Circular Vacuum Chamber,” *Phys. Rev. E* **51**, 3515 (1995).
- [3.2.24] E. Karantzoulis, V. Smaluk and L. Tosi, “Broad Band Impedance Measurements on the Electron Storage Ring ELETTRA,” *Phys. Rev. ST-AB* **6**, 030703 (2003).
- [3.2.25] B. Podobedov and S. Krinsky, “Transverse Impedance of Elliptical Cross-Section Tapers,” Proc. EPAC2006, 2973 (2006).
- [3.2.26] A. Blednykh, S. Krinsky, B. Podobedov, and J.M. Wang, “Transverse Impedance for Small-Gap Undulators for NSLS-II,” Proc. EPAC2006, 2973 (2006).
- [3.2.27] P. Stefan et al., “Small-Gap Undulator Research at the NSLS: Concepts and Results.” *Nucl. Instr. Meth. A* **412**, 161 (1998).
- [3.2.28] A. Blednykh, “Trapped Modes in an Elliptic Vacuum Chamber,” *Nucl. Instrum. Meth. A*.
- [3.2.29] P.J. Chou, “Numerical Analysis of Higher-Order Modes for Superconducting RF Cavity at SRRC,” Proc. Pac2003, 1368.
- [3.2.30] P.J. Chou, J. Chen, K.-T. Hsu, C.-C. Kuo, C. Wang, and M.-H. Wang, “Collective Effects in the TLS Storage Ring after the Installation of Superconducting Cavity,” Proc. PAC2005, 2360.
- [3.2.31] A. Piwinski Tech. Rep. HEAC 74, Stanford, 1974; See Also A. Piwinski in A. Chao and M. Tigner, *Handbook of Accelerator Physics*, World Scientific (1999) 125.
- [3.2.32] J. Bjorken and S. Mtingwa, “Intrabeam Scattering,” *Part. Accel.* **13**, 115 (1983).
- [3.2.33] K. Kubo and K. Oide, “Intrabeam Scattering Formulas for High Energy Beams,” *Phys. Rev. ST-AB* **4**, 124401 (2001).
- [3.2.34] K.L.F. Bane, “A Simplified Model of Intrabeam Scattering,” SLAC-PUB-9226 (2002).
- [3.2.35] T. Raubenheimer, *Part. Accel.* **45**, 111 (1994).
- [3.2.36] K. Oide, *SAD User’s Guide*.
- [3.2.37] A. Streun, “Momentum Acceptance and Touschek lifetime,” SLS Note 18/97.
- [3.2.38] A. Hofmann and S. Meyers, “Beam Dynamics in a Double RF System,” Proc. 11th International Conference on High Energy Accelerators, Geneva (Birkhauser Verlag, Basel, (1980), p 160.
- [3.2.39] N. Towne, “Stretched Bunch Shapes in the NSLS VUV Ring,” Proc. PAC1999 (1999) 2828.

[3.2.40]J.M. Byrd, S. De Santis, J. Jacob, and V. Serriere, “Transient Beam Loading Effects in Harmonic RF Systems for Light Sources,” *Phys. Rev. ST-AB* **5**, 092001 (2002).

3.3 Orbit Feedback System

3.3.1 Requirements for Beam Stability

To realize the benefits of the high brightness and small beam sizes of NSLS-II, it is essential that the photon beams are exceedingly stable, assuring constant intensity after apertures, constant photon energy after monochromators, and minimal photon source size and highly precise steering accuracy for focusing on small samples. For example, in the common case of 1:1 focusing optics, positional stability of the photon beam on the sample is directly related to that of the electron beam. The position of the photon beam should be stable to a level of $\Delta_y/\sigma_y \sim 10\%$. We require beam motion of no more than 10% of beam size, particularly in the frequency range from ~ 10 mHz to 100 Hz. This tolerance has been adopted by many synchrotron radiation laboratories. Since the minimum vertical beta function is about 1 m, when we take the vertical emittance as $10^{-10}/4\pi$ m, the vertical beamsize is $2.7 \mu\text{m}$ RMS. Therefore, the beam position stability should be $\sim 0.3 \mu\text{m}$ in the short straight section.

3.3.2 Fast Orbit Motion with Feedback Loop On and Off

For the NSLS-II ring with a DBA30 lattice as shown in Figure 3.1.1 (only half a super-period is shown), the performance of a fast, closed-orbit feedback system with 120 BPMs and 120 correction trims was calculated. The BPM and fast corrector positions used in this simulation are shown in Figure 3.3.1. The vacuum chamber at the fast correctors is made of stainless steel.

We averaged over 400 different sets of random numbers for positional deviation of all the quads, assuming they vibrate randomly with uncorrelated RMS displacement of $0.2 \mu\text{m}$. The resulting beam RMS motion $\sigma_{\Delta y}$ is shown in blue in Figure 3.3.2. We used 60 out of 120 eigenvectors in this case.

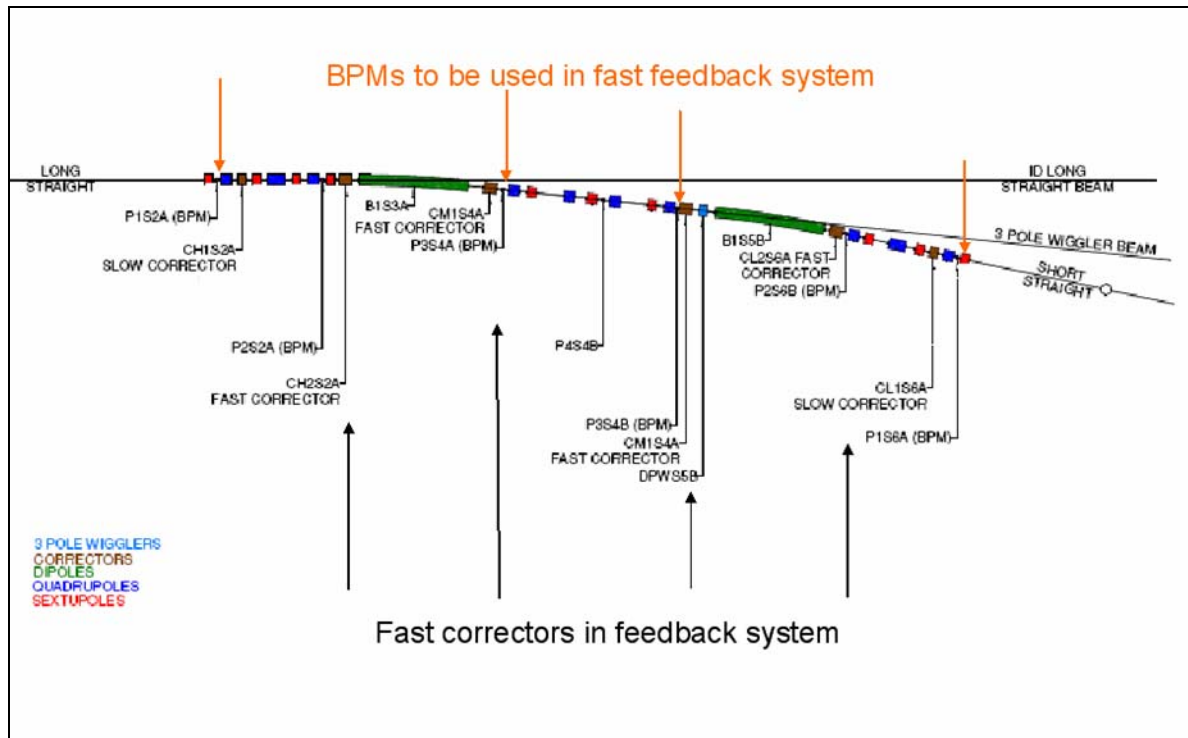


Figure 3.3.1 Positions of BPMs and fast correctors in one cell.

For each set of Gaussian random errors for the quad and BPM vibrations, all with RMS displacement of $0.2 \mu\text{m}$, the open-loop BPM signal was calculated assuming BPM electronic noise is $0.2 \mu\text{m}$. Then the SVD matrix was used to calculate the corrector strengths, and finally the orbit with the feedback loop closed with a gain of 100. After averaging over 400 random samples, the residual RMS beam motion shown in Figure 3.3.2 was obtained, represented by the red curve. The open-loop BPM signal and the corrector strength used in the feedback loop are marked by dark green and purple dots, respectively.

The height of the purple dots represents the RMS strength of the correctors, in units of μrad . The figure shows that the feedback loop reduces the beam motion at the center of the long straight section ($z = 0$) from $3 \mu\text{m}$ to $0.2 \mu\text{m}$. The maximum RMS corrector strength is on the order of $0.14 \mu\text{rad}$.

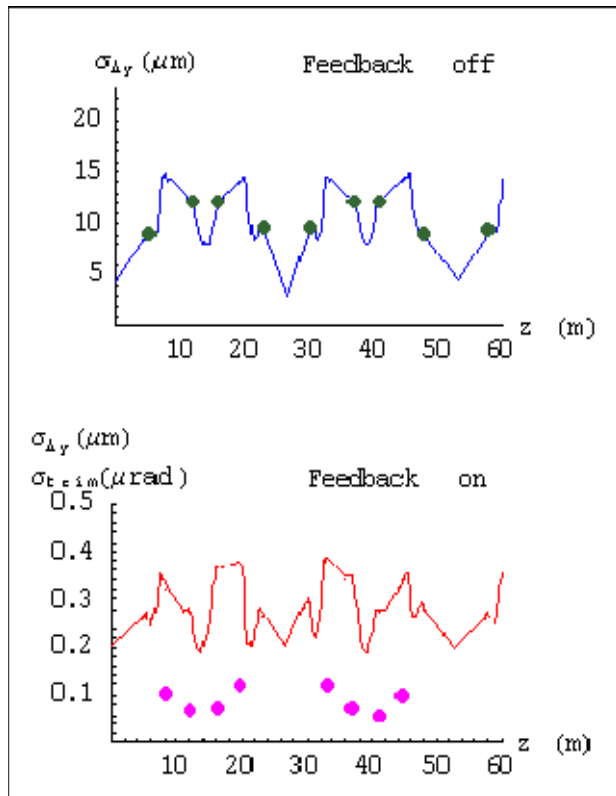
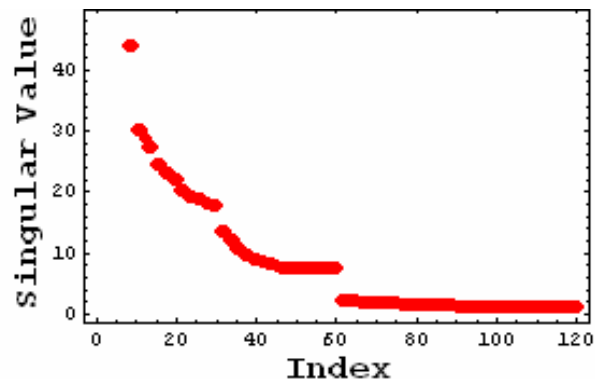


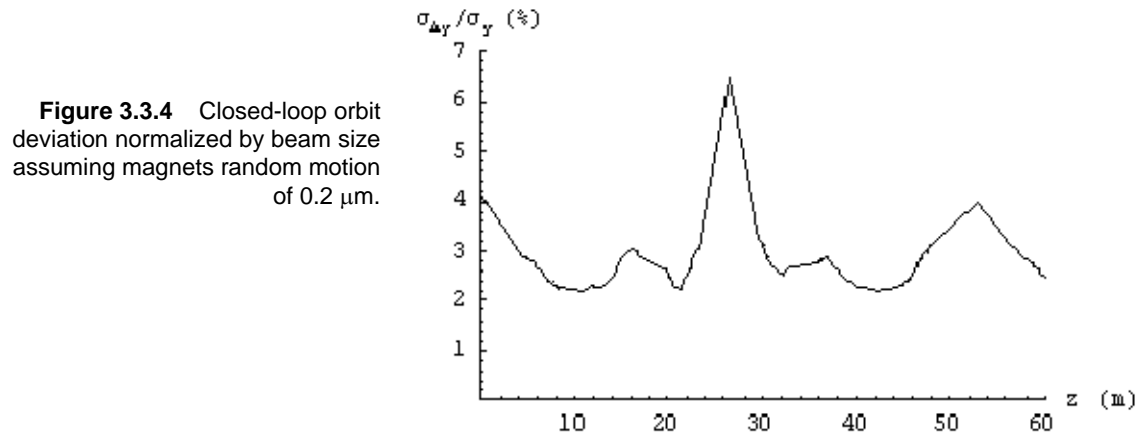
Figure 3.3.2 Open (blue) and closed-loop (red) RMS orbit motion and RMS corrector strengths (purple dots) in the feedback loop. The z -axis is the distance along the ring circumference, in meters. The green dots are the RMS motion at the location of the BPMs in the feedback loop. 60 eigenvalues out of 120 are used in this simulation.

Figure 3.3.3 gives the singular value spectrum for the 4BPM, 4 trims feedback system, indicating the possibility of using 60 eigenvectors, or using 2 trims per cell in vertical plane. Simulations confirmed that both give similar performance.

Figure 3.3.3 Singular values for the feedback system with four BPMs and four trims shows that using 60 eigenvectors should have similar performance to using all 120, and this is confirmed by simulation. It also indicates that good performance could be obtained using only two trims per cell (60 eigenvectors).



The tolerance on the floor motion required to keep beam motion within 10% of beamsize was determined using the following assumptions: 1) $\epsilon_y = 0.1 \text{ nm}/4\pi$, 2) all the quads and BPMs mounted on the girders have uncorrelated random vibration of $0.2 \text{ }\mu\text{m}$, and 3) the BPM electronic noise is $0.2 \text{ }\mu\text{m}$. Averaging over 400 samples gave the ratio of the vertical beam motion divided by the RMS beamsize as a function of z in the ring, shown in Figure 3.3.4. At the short straight section, the ratio of beam motion over beamsize is 6.4%. This implies that the tolerance for the quad vibration is more than $0.3 \text{ }\mu\text{m}$ RMS. This calculation ignored the fact that for low-frequency ground motion, the movement of different components mounted on the girders can be correlated, since the sound wavelength at low frequency can be larger than the girder dimension. Actually, simulation for correlated movement of quads mounted on the same girder shows a reduced amplification factor, since the quads moving together tend to cancel each other [3.3.1]. The noise caused by ripples in the power supply corrector magnet current was also ignored. Compared with this effect, the orbit motion due to the vibration of BPMs is much more difficult to suppress. Actually, it is very difficult to reduce the beam motion to much less than the amplitude of the BPM vibration. Similar calculations for horizontal orbit show that if quads and BPMs have random vibration of RMS value $0.2 \text{ }\mu\text{m}$ and BPM noise is $0.2 \text{ }\mu\text{m}$, the residual RMS value of beam motion is $0.14 \text{ }\mu\text{m}$ at the straight sections. Since the horizontal beam size is much larger than the vertical beam size, the horizontal requirement is much easier to satisfy than the vertical.



The beam motion due to power supply noise in a digital feedback system is determined by the voltage corresponding to the last bit of the power supply and the power supply current noise itself [3.3.1, 3.3.2]. Similar to the vibration simulation, we find that if we require beam motion (due to trim noise at the beam waist where $\beta_y = 1.26 \text{ m}$) to be less than $0.1 \text{ }\mu\text{m}$, the RMS trim noise should be less than 4 nrad. Hence the power supply should be accurate to $4 \text{ nrad}/0.29 = 12 \text{ nrad}$. If the maximum trim strength is 1 mrad, we need the last digit to be less than 12 ppm and the RMS noise should be less than 4 ppm.

3.3.3 Ground Movement at the NSLS-II Site

Figure 3.3.5 shows floor vibration measurement in January 2007 at three locations: CFN, field near CFN future NSLS-II site, and NSLS beamline. This data show that due to cultural activity the noise level is higher at the current NSLS site than CFN center and the field where the future NSLS-II is located. It shows that with improved floor design and construction, the vibration noise is much lower. In Figure 3.3.6, the inverse integrated PSD of floor vibration measurement at UV ring floor near entrance using seismic sensor shows RMS vibration amplitude within bandwidth from 0.5 Hz-100 Hz is less than $0.1 \text{ }\mu\text{m}$. Since the sound speed in concrete is 3 km/s, below 0.5 Hz, the ratio of sound wavelength over the storage ring diameter is sufficiently large that the effect of the vibration below 0.5 Hz is not critical.

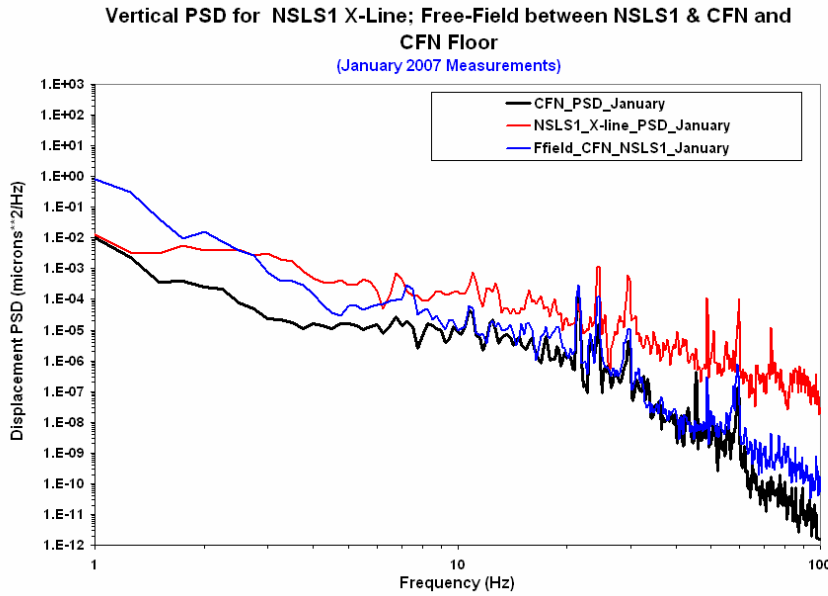


Figure 3.3.5 Floor vibration measurement at three locations: CFN, field near CFN future NSLS-II site, and NSLS beamline X1.

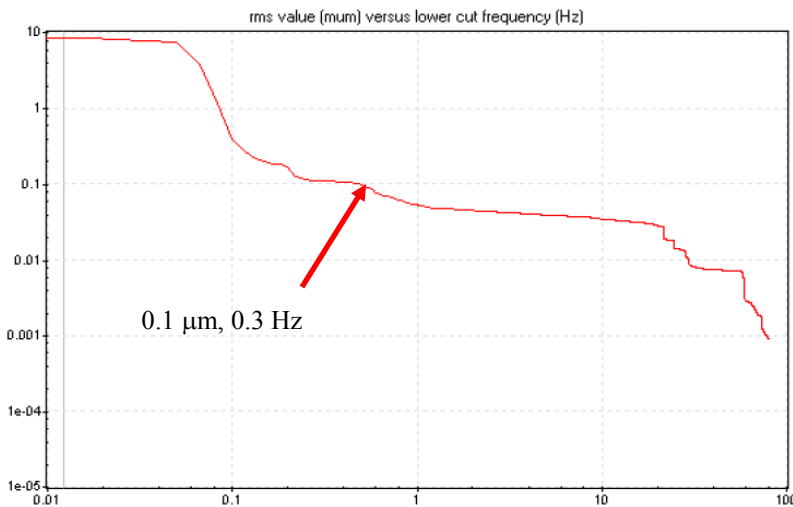


Figure 3.3.6 Inverse integrated PSD of floor vibration measurement at UV ring floor near entrance using seismic sensor showing RMS vibration amplitude within bandwidth from 0.5 Hz-100 Hz is less than 0.1 μm.

3.3.3.1 Long-Term Ground Movement

As for long-term ground movement at the BNL site, measurements carried out at RHIC between 1997 and 2002 show the coefficient A in the ATL law is $A \approx 3 \times 10^{-18} \text{ m}^2/\text{m/s}$ [3.3.4, 3.3.5]. Based on this, we estimate that the RMS movement within the 252 m diameter of NSLS-II over a half-year is about 110 μm.

We simulated the performance of the slow feedback system on long-term ground motion using the ATL law [3.3.6] at the NSLS-II site over a half year, with the same set of BPMs and correctors as mentioned in Section 3.3.2. The results are shown in Figure 3.3.7. In this specific example, the maximum ground movement was 107 μm, with an RMS value of 36 μm. The maximum relative movement between the beam and the ground was about 700 μm without feedback; with feedback, it was 48 μm with an RMS value of about 10 μm.

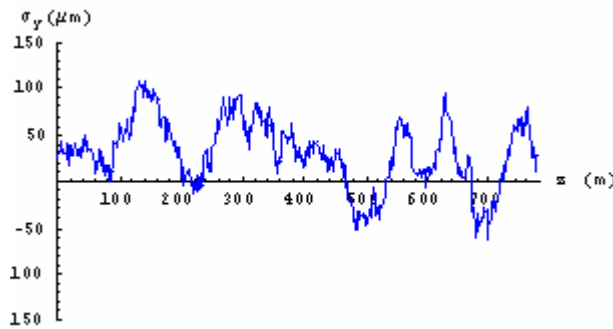
We averaged over 400 samples. The RMS residual movement has a mean value of $9.3 \mu\text{m}$. This is over half a year. When we scaled according to the ATL law, the residual RMS movement within a day should be reduced to about $0.7 \mu\text{m}$.

If the orbit is realigned every six months, then within that half year the required corrector strength for the global orbit correction is about 0.1 mrad . To leave a margin for error, the maximum strength of the corrector is specified to be 0.5 to 1 mrad . As shown in Section 3.3.2, this requires the last bit of the power supply to be 30 ppm .

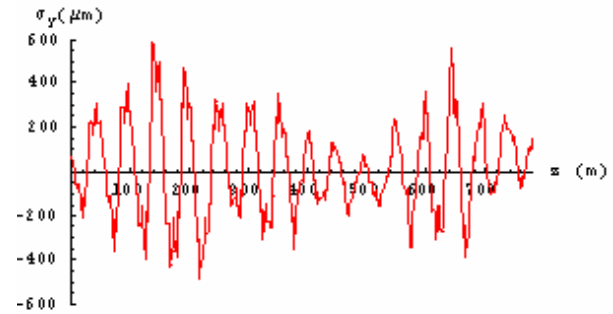
3.3.3.2 Temperature Stability

As we discussed in Section 3.3.2, the most stringent requirement on orbit stability is in the 6.6 m straight sections, where the BPM motion is required to be less than $0.2 \mu\text{m}$ (see Figure 3.3.4). Due to thermal expansion of the girder and vacuum chamber support system, the air temperature stability in the storage ring tunnel is specified to be $\pm 0.1^\circ\text{C}$. We specify that the BPMs will move less than $\pm 0.2 \mu\text{m}$. To insure that in the short straight sections the orbit motion satisfy the stability requirement, we specify the BPMs at the ends of insertion devices in 6.6 m straight sections move less than $\pm 0.1 \mu\text{m}$ with specially designed BPM supports. Our simulation shows that when those BPMs in the short straight sections move less than others, the feedback system also insure the orbit motion in those sections less than other sections correspondingly.

Feedback Loop Off

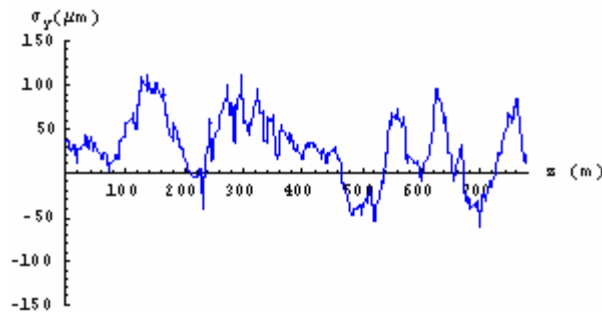


Floor motion around the ring. While the RMS of the relative displacement across the ring diameter for a large number of examples is $110 \mu\text{m}$, in this specific example the maximum movement is $107 \mu\text{m}$, and the RMS around the ring is $36 \mu\text{m}$.

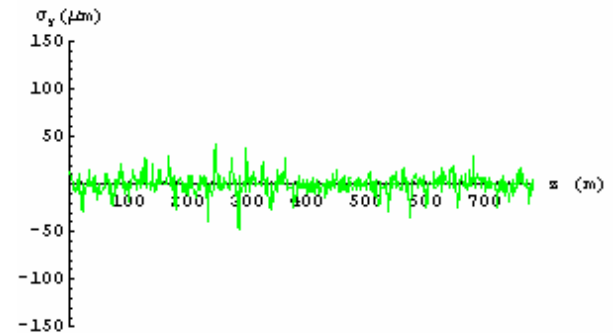


Electron beam motion (vertical) without feedback loop; maximum is $600 \mu\text{m}$.

Feedback Loop On



Electron beam motion with the feedback loop on follows the floor motion approximately.



Electron beam motion relative to floor (the difference between the two plots on the left) with the feedback loop on; maximum is $48 \mu\text{m}$, RMS $10 \mu\text{m}$.

Figure 3.3.7 Simulated long-term ground motion and electron beam motion within half a year, with feedback system on and off. The horizontal axis is the distance along the circumference.

3.3.4 BPM Resolution and Noise Floor

A power density spectrum plot of measurement of orbit motion at NSLS using an RF BPM is reported in Figure 3.3.8, with beam motion shown in blue and the noise floor of the BPM in red. The plot shows that above 200 Hz, the beam motion is dominated by the noise floor. Hence, a feedback system with frequency higher than 200 Hz will not improve the orbit stability. The feedback system based on our BPM should have a cut-off point set below 200 Hz. Measurements at NSLS show that the vibration amplitude between 50 Hz and 200 Hz is less than 10 nm, which is negligibly small. Therefore, to relax the requirement on the feedback system bandwidth, the cut-off point is set at 60 Hz. A long-term drift test of the BPM offset is still needed, to show it is sufficiently small (lower than 0.2 μm). BPMs with better performance are available, and work in developing better BPMs is needed.

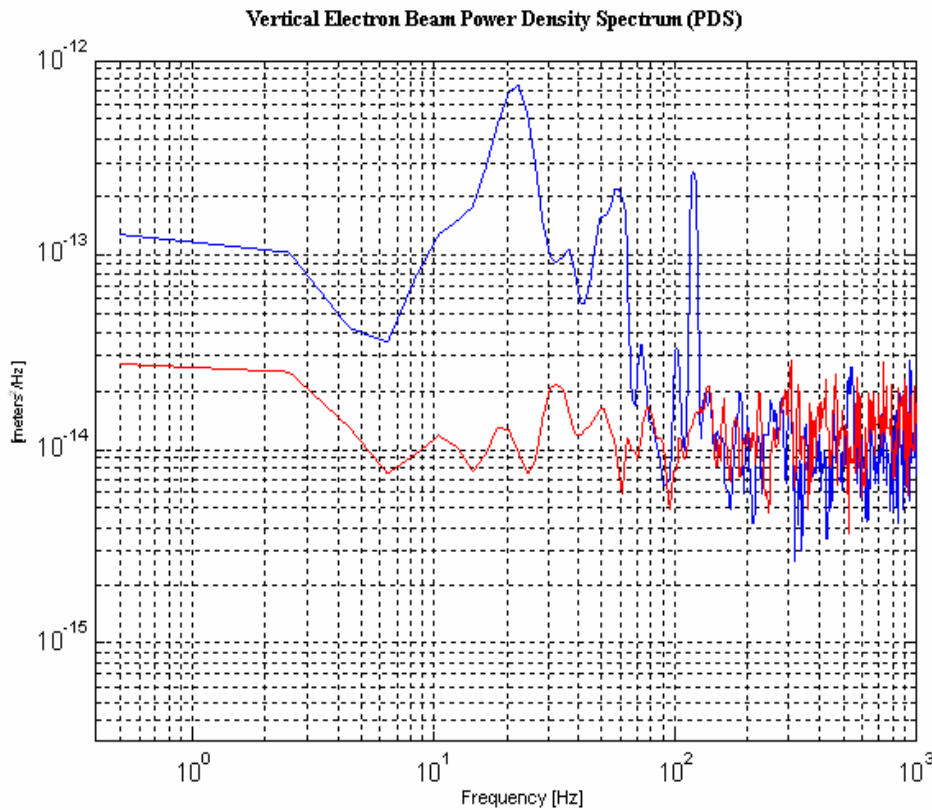


Figure 3.3.8 Power density spectrum of beam motion.

3.3.5 Requirements for the Feedback System

Based on these considerations, the ground vibration of 0.2 μm above 0.5 Hz satisfies the 0.3 μm requirement determined by the feedback system performance calculation presented in Section 3.3.2. However, the BPM motion caused by thermal expansion poses the most stringent requirement on the temperature stability, we require the ring tunnel temperature stability to be within $\pm 0.1^\circ\text{C}$, and the BPM supports are designed such that they move less than $\pm 0.2 \mu\text{m}$ within $\pm 0.1^\circ\text{C}$. In particular the BPM supports at the ends of the insertion devices in the 6.6 m sections are designed to move less than $\pm 0.1 \mu\text{m}$ within $\pm 0.1^\circ\text{C}$.

As mentioned in Section 3.3.4, the measured beam motion coincides with the BPM noise floor for frequencies higher than 200 Hz (see Figure 3.3.8). In addition, since most of the motion comes below 60 Hz, it is desirable to design the feedback system PID circuit to reach a 60 Hz bandwidth.

Because eddy currents are proportional to the thickness and electrical conductivity of materials, only thin laminations (1 mm thickness) or air coils should be used for correctors and the low-conductive materials preferred for vacuum chambers. Eddy currents in vacuum chambers usually impose the most critical bandwidth limitation on the feedback loop [3.3.1].

When designing the feedback system bandwidth, it is crucially important to design the vacuum chamber and power supplies for all the correctors to be used in the fast global feedback system such that they have the same frequency response. Without excellent equalization, we may be forced to narrow the bandwidth of the feedback system or lower the gain of the system.

To maintain the dynamical aperture regardless of long-term ground movement requires the beam to stay within 50 μm of the center of the sextupoles. According to the simulation based on the ATL law, described in Section 3.3.2, if the ring is regularly realigned, this can be achieved. RF frequency will also be used as an additional corrector to compensate for energy drifts.

References

- [3.3.1] M. Borg, PAC '01, talk on IWBS'02, and EPAC 04 paper.
- [3.3.2] J. A. Carwardine and F. R. Lenkszus, "Real-Time Orbit Feedback at the APS," p.12, 1997 beam instrumentation workshop at SSRL.
- [3.3.3] Heiko Ehrlichmann, private communication (2/2006).
- [3.3.4] Vladimir Shiltsev, "Space-Time Ground Diffusion: The ATL Law for Accelerators," DESY-MPY, Notkestrasse 85, 22603 Hamburg, Germany.
- [3.3.5] Vadim Ptitsyn, private communication (7/2004).
- [3.3.6] A. Walski, and N.J. Walker, Proceedings of 2003 PAC.

3.4 Canting and Decker Distortion for the NSLS-II

Canting and Decker distortion are similar in that they both require additional trim dipoles placed in the ID straight. In both cases the dispersion must be constrained in the cell. Furthermore, the sum of the additional bend angles must be zero to ensure the beam orbit stays on the center of the multipole magnets. Therefore there are three constraints at the end of the bump:

$$\begin{cases} \eta = 0 \\ \eta' = 0 \\ \sum \theta = 0 \end{cases} \quad (3.4.1)$$

It requires three independent knobs to satisfy these constraints. In addition, we require that the perturbation to the linear lattice must be small.

Decker distortion has proven effective in reducing the stray background radiation for the photon BPMs at the Advanced Light Source [3.4.1]. Even though the stability of the photon beam is directly related to that of the electron beam circulating in the storage ring, it is also affected by other factors, such as the electron trajectory in the insertion devices. Moreover, the long beamline amplifies small jitter of the electron beam. Hence including photon BPMs to the feedback loops helps keep the photon beam stable.

The characteristic radiation angle from the NSLS-II storage ring dipole is $1/\gamma \sim 0.17$ mr; the dipole kick from the strongest quadrupole is about one milliradian if the beam is offset by 2 mm; therefore the distortion angle is determined to be 1~2 mr.

At APS, Decker distortion was implemented after the storage ring and the beam lines were built. In their case, moving the magnet girders was easier than moving the straights and the beam lines. Their approach was to add two trims to the front and the end of a cell and then move the entire cell except the straight section. For NSLS-II, we looked at other possible options, since we can design from the beginning. Instead of moving a cell, we found it is convenient to offset the ID straight with two trims and vary the cell magnets to fulfill the constraints. The diagram is shown in Figure 3.4.1. One can vary B1, B2, the main bending magnets, M1, the trim in the straight, and all the quadrupoles to form a dispersion bump. The downstream cell is reflection symmetric to the upstream one. We examined two solutions: in the first solution we vary only the dipoles and the trims; and in the second solution we also adjust the quadrupoles, but the field in only one main dipole is changed.

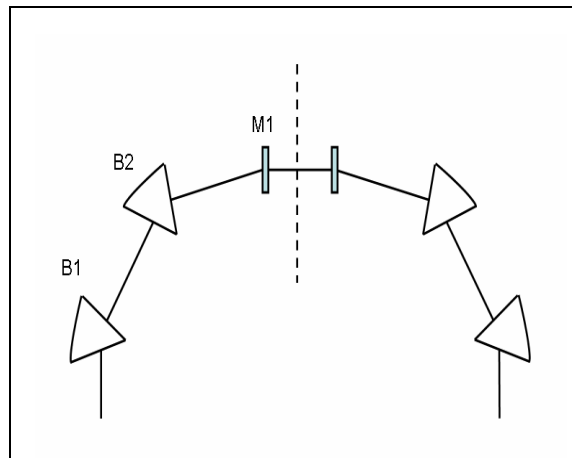


Figure 3.4.1 Diagram of Decker distortion proposed for NSLS-II.

Figure 3.4.2 shows the first solution of Decker distortion for the NSLS II lattice. In this solution only the dipoles are varied. The bend angle adjustment in the dipoles and the trim is: $\Delta\beta_1 = -1.727$ mr, $\Delta\beta_2 = 0.727$ mr and $M_I = 1$ mr. The quadrupole settings are not changed therefore the beta functions, the emittance and the tunes are kept the same. The dispersion in the long straight is constrained to zero. The dispersion departs from zero in the short ID straight and has the value 5 mm. Because of the symmetry and emittance constraints, the effect on the beam size and the emittance growth is negligible.

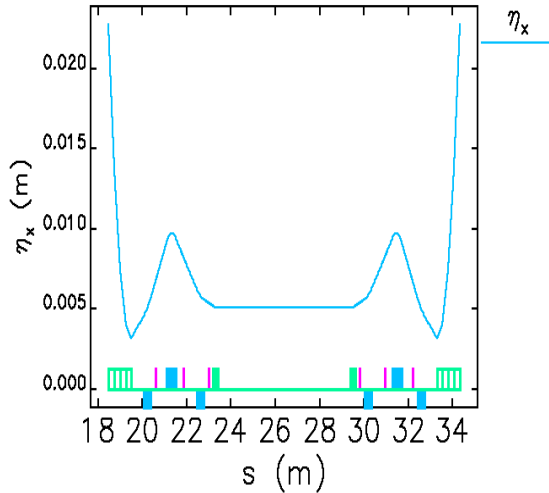


Figure 3.4.2 Dispersion function in the dipole-only solution.

The second solution with variation of quadrupoles is shown in Figure 3.4.3. In this solution there is no need to change B_1 . The parameters are: $\Delta\beta_1 = 0$ mr, $\Delta\beta_2 = -1$ mr, and $M_I = 1$ mr. The relative quadrupole strength changes are small, $|\Delta K_1 / K_1| \leq 0.015$. The dispersion in the long straight is zero and it is about 0.3 mm in the short straight. This scheme has an advantage in that the girder between the two main dipoles does not have to be moved.

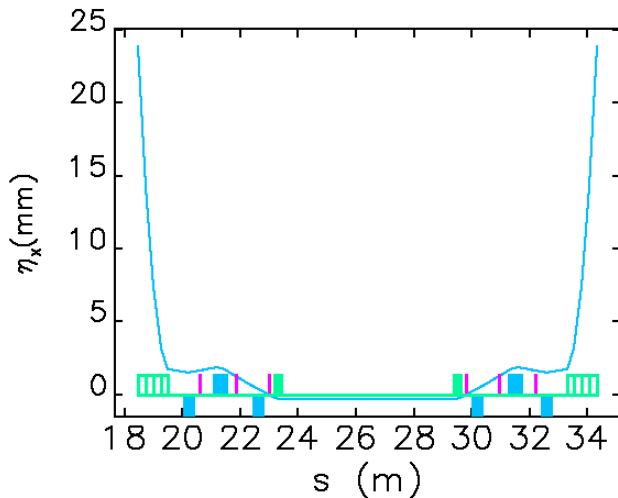


Figure 3.4.3 The second solution: varying $\Delta\beta_2$ and the quadrupoles.

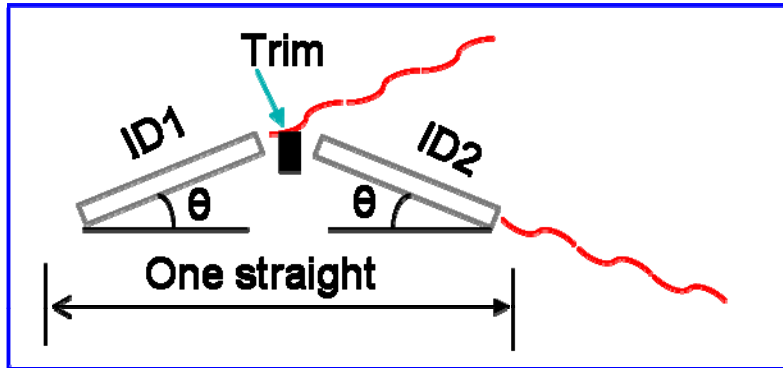


Figure 3.4.4 Diagram of canting.

The idea of canting is to split the radiation from one straight into two beam lines as is diagrammed in Figure 3.4.4. However, this also introduces external dispersion and the damping wigglers excite quantum fluctuations. The emittance growth is proportional to the dispersion invariant $H = \gamma\eta^2 + 2\alpha\eta\eta' + \beta\eta'^2$. It can be shown that if the dispersion function at the center of the straight is much less than $\beta_c\theta$, where θ is half of the canting angle; i.e., if

$$\eta_c \ll \beta_c\theta, \quad (3.4.2)$$

then the dispersion invariant is minimized, and

$$H_{\min} \approx \beta_c\theta^2. \quad (3.4.3)$$

Therefore the emittance growth is proportional to the center beta function and square of the canting angle.

At commissioning, NSLS-II will have three 7 meter-long damping wigglers. The relevant parameters are $\beta_w=1.8$ T, $\lambda_w=9$ cmT, cm. One calculates the opening angle to be $2\theta=2.6$ mr. It has been decided the maximum canting angle is 3.5 mr. With the minimized H_{\min} , the emittance growth is calculated as a function of the number of canted damping wigglers. The results are listed.4.1.

Table 3.4.1 Emittance Growth Due To 3.5 mr Canting.

	None canted	All canted	Growth factor
Emittance(nm)(21m)	0.9	0.96	1.068
Emittance(nm)(35m)	0.67	0.74	1.11
Emittance(nm)(56m)	0.51	0.59	1.16

The emittance growth for the baseline is only about 7% even if all three damping wigglers are canted. The emittance is less than 1 nm, which meets our design goal. Note the momentum spread is not affected by canting.

There are several choices to bend the electron orbit. A straightforward solution would be putting three trims in the straight. Such a solution is shown in Figure 3.4.5. The disadvantage of this solution is that 0.3~0.4 meters is needed for each trim; therefore the usable space for the insertion device is shortened.

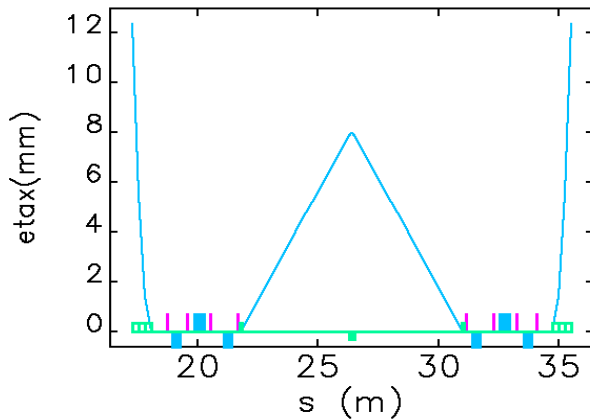


Figure 3.4.5 A straightforward solution for canting. Three trims are put in the straight as -2, 4, and -2 mr. The maximum dispersion is 8 mm.

The second option is to put only one trim in the center of the straight and vary the main dipoles and quadrupoles to satisfy the three constraints. A solution is shown in Figure 3.4.6. Note the negative dispersion in the center. This is because the dispersion invariant is minimized.

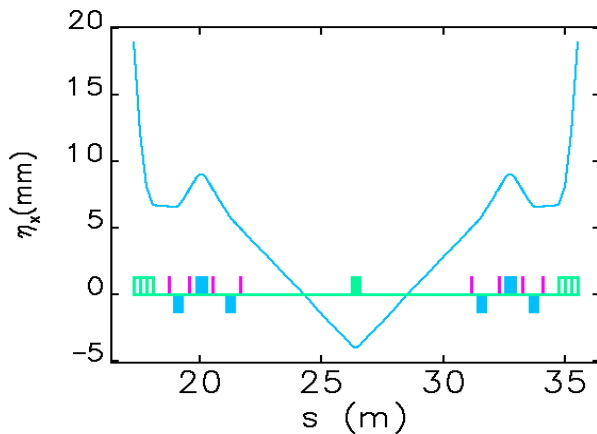


Figure 3.4.6 A solution of canting the damping wigglers. The angles or the changes are: $\Delta\beta_2 = -M_1 = -1.926$ mr. The quadrupole setting changes are $|\Delta K_1 / K_1| < 0.01$.

A third option would be to make special poles for the damping wigglers. One pole of the damping wiggler gives about 4 mr bending to the beam. If the end poles can be made longer, then the damping wiggler itself can bend the beam. This approach looks feasible and can save both space and cost on the magnets and power supplies.

References

- [3.4.1] G. Decker and O. Singh, Phys. Rev. ST Accel. Beams 2, 112801 (1999).

3.5 Extra-Long Straights

The lengths of the normal short and long straight sections at the NSLS-II are 6.6 m and 9.3 m, respectively. Some experiments, e.g., inelastic scattering experiments, would benefit from long insertion devices with length as great as 10~12 m. Such long insertion devices require extra-long straights of 12~15 meters.

A straightforward way to create such long straights is to make a few special cells; however, this approach reduces the symmetry of the lattice to the number of the longer straights and affects the dynamic aperture of the beam. In order to restore the symmetry, Hara et al. proposed a 2π transformer scheme[1]. The idea is to make the betatron phase advance a multiple of 2π for the two matching cells and the extra-long straight; therefore the symmetry is restored. Note the periodicity number is two units less because of the excluding of the two matching cells. This idea was successfully implemented at SPring-8 in the year 2000. Four 27 m long straights were created this way.

Another issue for extra-long straights is that the vertical gap of the insertion device imposes a limiting physical aperture on the storage ring. Note the beta function in the straight is given by

$$\beta(s) = \beta_c \left[1 + \left(\frac{s}{\beta_c} \right)^2 \right], \quad (3.5.1)$$

where β_c is the beta function at the center of the straight.

The present physical aperture of NSLS-II is limited by the ± 2.5 mm gap of the in-vacuum undulator. In order not to diminish the physical aperture, the gap of the long undulator has to satisfy

$$h \geq 2.5 \sqrt{\frac{\beta_s(L/2)}{\beta_L(L/2)}}, \quad (3.5.2)$$

where β_s and β_L are the beta functions at the ends of the IDs in the short straight and the extra-long straight. Varying β_c to maximize the aperture, one gets

$$h \geq 2.5 \sqrt{\frac{L_U}{L_L}}, \quad (3.5.3)$$

where L_U and L_L are the lengths of in-vacuum undulator and the long undulator. Therefore, if the gap remains the same, an ID that is four times longer would reduce the physical aperture by two-fold. And it will be even worse if β_c is minimized for the purpose of higher brightness.

To focus the beta functions to small values while maintaining the physical aperture, quadrupole magnets can be added to the long straight to create segments. The quadrupoles are also helpful for matching the phase advance inside the long straight. Suppose the betatron phase advance of a normal straight is $\Delta\Psi$; if the phase advance of the segmented extra-long straight is $2\pi + \Delta\Psi$, then the extra-long straight is the same as a normal straight, from the symmetry point of view.

One can show that the betatron phase advance in a magnet-free section is less than π . Hence, to obtain 2π phase advance, a minimum of three sections are needed. To get a better understanding of the problem, we designed a solution for NSLS-II; the beta functions are plotted in Figure 3.5.1.

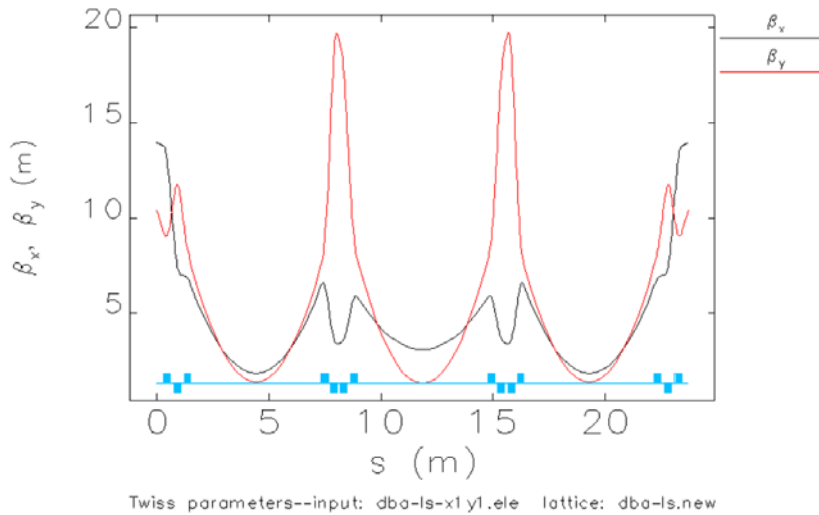


Figure 3.5.1 A segmented extra-long straight solution for NSLS-II. It starts from the last magnet in the long straight of a normal cell. The total length is 23.7 m with three equal-length straights of 5.83 m each. The generated chromaticity is $\Delta\zeta_x = -1.04$ and $\Delta\zeta_y = -3.01$. The beta functions at the center of the sections are $\beta_x / \beta_y = 1.8/1.4, 3.0/1.3,$ and $1.8/1.4$ m.

Because dispersion is zero everywhere in the extra-long straights, the generated chromaticity has to be corrected by the sextupoles in the other cells. Therefore the chromaticity in every cell cannot be corrected to zero. Because of this, the extra-long straight is not transparent to the off-momentum particles. One can show that if n extra-long straights are inserted into an m -period storage ring, then the ring is $n < m$ fold symmetric for the off-momentum particles.

Proper selection of the working point and careful elimination of the higher-order terms might restore the dynamic aperture. However, the impact of extra-long straights on the stability of the dynamic aperture of off-momentum particles could not be studied in sufficient detail before the decision on the NSLS-II footprint could be made. Furthermore, there are issues, such as the deposition of high synchrotron radiation power on the extra-long undulator beam pipes. For this reason, an alternative approach to extra-long straights is envisioned, which could be implemented into the footprint of NSLS-II.

This idea is illustrated in Figure 3.5.2. Two cells are moved aside, converting the middle straight into an extra-long straight, the maximum length of which is about 18 m for the present lattice.

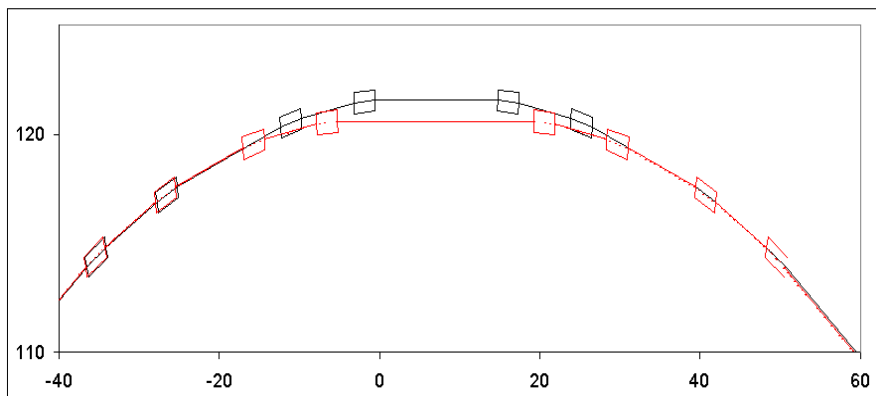


Figure 3.5.2 Moving the cells to create an extra long straight.

This scheme would allow compensation of the chromaticity and nonlinear terms in the moved cells, and they can be transparent to the off-momentum particles if all the relevant higher-order terms are eliminated. The impact of such an insert on dynamic aperture is under study.

[3.5-1] M. Hara, T. Nakamura, T. Takada, and H. Tanaka, "Use of long straight sections of SPring-8," Rev. Sci. Instrum. 63 (1), p.355, 1992.